Analysis of a dual stacked rectangular microstrip antenna

Zwemstra, T.

Award date:
1989

EINDHOVEN UNIVERSITY OF TECHNOLOGY
DEPARTMENT OF ELECTRICAL ENGINEERING
GROUP ELECTROMAGNETISM AND CIRCUIT THEORY

ANALYSIS OF A DUAL STACKED RECTANGULAR MICROSTRIP ANTENNA

by T. Zwemstra

ET - 14 - 89

Report on the graduation project performed in fulfilment of the requirements for the degree of Master of Science (Ir.) at the Eindhoven University of Technology, Department of Electrical Engineering, in the period november 1988 - september 1989 under supervision of dr. M.E.J. Jeuken.

Eindhoven, 29 september 1989

ABSTRACT

In this report a rigorous analysis is presented of dual stacked rectangular microstrip antennas, in order to investigate their characteristics and possible improvement in bandwidth compared to the conventional single-patch microstrip antenna. The stacked antenna consists of two rectangular microstrip patches stacked on top of each other and one dielectric layer separating the patches and another dielectric layer separating the lower patch from the ground plane. These two substrate layers in general have different dielectric properties. The two patches can have different sizes and also an offset can be introduced between the upper and lower patch, The stacked microstrip antenna is fed by a coaxial feed connected to the lower patch.

The stacked microstrip antenna is modeled as a plane stratified medium with zero-thickness surface current layers replacing the actual patch currents flowing on the microstrip patches. The electromagnetic fields radiated by these current layers are derived everywhere inside this stratified medium and they are expressed as superposition integrals in terms of surface-current and associated surface-charge distributions on the interfaces of the dielectric layers and magnetic-vector- and scalar-potential associated spatial Green's functions, which incorporate the geometry and properties of the stratified medium. Next the field due to the coaxial feed is derived and a type of electric-field integral equation is set up which is solved in the space-domain for the unknown patch surface currents using a method of moments. Once these currents are known, the antenna characteristics which are of interest here, namely their resonant behaviour, input-impedance and impedance-matching are easily found. For accurately predicting the antenna characteristics, efficient numerical techniques for the numerical evaluation of this particular treatment of the microstrip radiation problem are reviewed. Some stacked microstrip antenna geometries have been analyzed and are presented, and these preliminary results show that only a moderate increase in bandwidth and improvement of the impedance-matching is obtained, but that possibly a more extensive investigation of the effect of the various microstrip parameters would reveal a further enhancement of the bandwidth and matching to the feed line. Some results also show that the stacked microstrip antenna could be used as a dual frequency antenna through a proper choice of the microstrip parameters.

Errata:

p.19 Eqn.(2.45) : $H_1^{(2)}(k_\rho \rho)$ i.p.v. $H_0^{(2)}(k_\rho \rho)$

p.39 Eqn.(2.101) : $Z_s \int_{S_i} \bar{f}_{ki}(r_i) \cdot \bar{f}_{lj}(r_i)\, ds_i$

p.52 : β_{TM0} i.p.v. β_{TE0}

p.54 regel 7 na Eqn.(2.128): that the integrands

p.58 Eqn.(2.131) : $H_n^{(1)}(z)$ i.p.v. $H_n^{(2)}$ in bovenste betrekking

CONTENTS

1 INTRODUCTION

The analysis and design of a circularly polarized microstrip phased array antenna for mobile satellite communications in the 1.5-1.6 GHz. band has been the subject of recent investigations within the Group Electromagnetism and Circuit Theory of the Department of Electrical Engineering at the Eindhoven University of Technology. This research has shown that the well-known major drawback of microstrip patch antennas, namely their narrow impedance bandwidth, has proved to be a particular disadvantage in a microstrip phased array [1]. Without some means of overcoming this difficulty it is even impossible for such a phased array antenna to be realized in practice. One possible way of enhancing the frequency band over which the microstrip antenna is matched to the feeding network is to increase the impedance matching of the microstrip patch by incorporating some sort of matching network into the antenna design [2]. Another way, and the subject of the research presented in this report, is to search for microstrip patch antennas which have an inherently broader bandwidth and, if possible, provide a good impedance match over a desired frequency range.

As an example of this last approach, when using a conventional single-patch microstrip antenna, removal of parts of the upper conductor, for instance a slot or a cross, seems to broaden the bandwidth of the overall microstrip patch antenna. Research into this type of microstrip antenna is currently underway and will be reported elsewhere [4].

The introduction of several stacked dielectric layers together with multiple stacked microstrip patches has also proved to be a very promising way for the enhancement of the bandwidth of microstrip antennas [3]. The idea behind the use of multiple stacked patches is that you can try to create several close resonances which, together, provide a much broader bandwidth compared to just one single resonance for a single patch microstrip antenna. An additional advantage of these types of microstrip antennas is that, instead of creating a single broader resonance, you can also obtain several close, but still separate, resonances, thus providing multiple frequency operation; see for instance [5].

Obviously, a wide variety of stacked microstrip patch antennas can be

investigated, differing in size, form and number of stacked patches, the type of dielectric substrates used and the configuration of the microstrip feed. We shall however focus on a stacked microstrip antenna consisting of two dielectric layers and two stacked, and possibly offset, rectangular patches, the whole antenna being fed by a coaxial probe connected to the lower patch (figure 1.1).

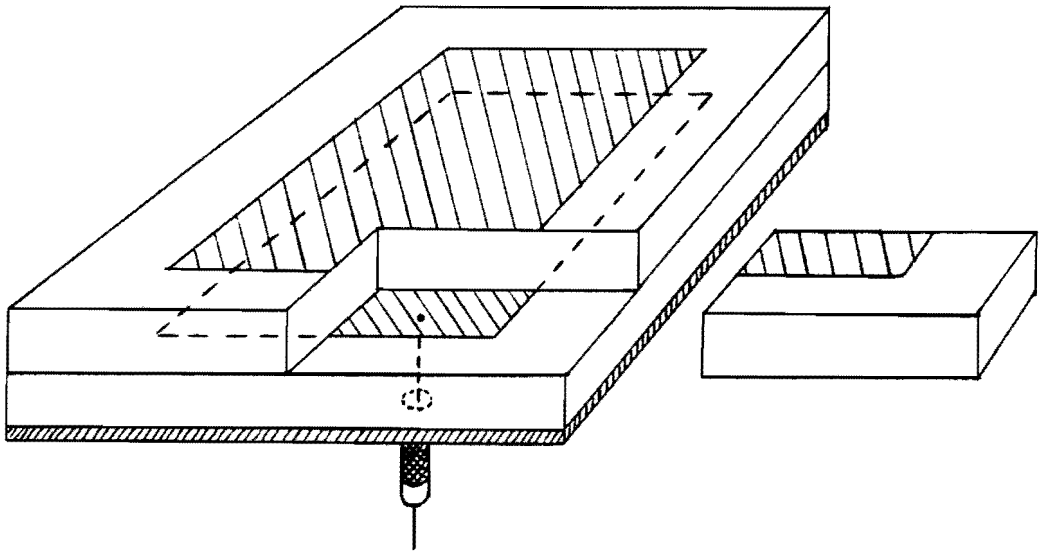

Fig 1.1 A dual stacked rectangular microstrip antenna

In this report a rigorous analysis of a dual stacked rectangular microstrip antenna, as depicted in the above figure, is carried out, introducing only a minimum of simplifying assumptions. In the next chapter the details of this analysis are presented after a short introduction into the particular method of analysis used and a description of model used to describe the microstrip antenna. Chapter 3 gives the details concerning the numerical evaluation of the antenna parameters of interest, based on the preceding analysis. And finally in chapter 4 some results are presented, primarily aimed at emphasizing some characteristics of stacked microstrip antennas, related to their frequency behaviour, input-impedance characteristics and matching ability, and also to provide a comparison with single-patch microstrip antennas.

2 ANALYSIS OF THE MICROSTRIP ANTENNA USING POTENTIAL ASSOCIATED SPATIAL GREEN'S FUNCTIONS

In this chapter the theoretical analysis is given for a dual stacked rectangular microstrip antenna in order to arrive at expressions for calculating the resonant frequency and input impedance, which are used to study the frequency behaviour and bandwidth characteristics of such antennas. The analysis is performed using dyadic and scalar Green's functions for expressing the electromagnetic fields in terms of the surface currents and surface charges induced on the microstrip patches and the excitation currents and charges on the coaxial probe, and a type of electric field integral equation is solved in the space domain for the unknown surface currents on the patches. Once these currents are known, the input impedance can be obtained and the frequency behaviour of the antenna investigated. After an introduction into the method which will be used for analyzing microstrip antennas, so that one will get a general idea along which lines the analysis will proceed, the particulars of the present analysis will be presented in a step-by-step approach, which will eventually lead to the accurate evaluation of the input impedance of the antenna.

2.1 General outline

Microstrip antennas have been the subject of numerous research efforts over the last few decades and a large number of mathematical models have been employed to analyze them. These models ranging from very simple ones with a lot of simplifying assumptions to very advanced ones. Because our aim is to accurately predict the characteristics of the stacked microstrip antenna, the more simple models, such as the cavity model, will not do; even if it were possible to extend these simple models to the study of stacked microstrip antennas. One therefore has to look for analysis methods which provide a theoretically exact description of the microstrip antenna in terms of fields, currents and charges, and based on fundamental electromagnetic theory. Above all it must correctly take into account the properties which are basic to microstrip antennas such as the presence of the conducting ground plane and the two dielectric substrate layers, possible losses in the dielectrics and

on the conducting patches, and the radiation in the dielectric layers and in free space.

One commonly encountered method of analysis is one which considers the currents flowing on the patches as the source of radiation into the microstrip structure and into free space. These surface currents are induced on the patches in the presence of an excitation field, in our case the field created by the coaxial feed probe, and the main problem is to find these unknown currents, after which quantities like the far field radiation pattern and the input impedance can be obtained.

The radiated or diffracted electric field due to an arbitrary surface current distribution $\bar{J}_s$ can, in general, be written as the following superposition integral:

$$\bar{E}^r(\bar{r}) = \int_S \bar{\bar{G}}_e(\bar{r}/\bar{r}') \cdot \bar{J}_s(\bar{r}')\, ds' \qquad (2.1)$$

in which the surface integration is performed over the surface S on which the surface current $\bar{J}_s$ flows. This formulation also holds for two separate, non-overlapping, surface current distributions, for instance $\bar{J}_s = \bar{J}_{s1} + \bar{J}_{s2}$ and $S = S_1 \cup S_2$, which is the case for two microstrip patches. Surfaces S_1 and S_2 then correspond to the microstrip patches and $\bar{J}_{s1}$ and $\bar{J}_{s2}$ are the surface currents flowing on them. The function $\bar{\bar{G}}_e(r/r')$ is an electric-type dyadic Green's function which gives a linear relation between the currents at source point $\bar{r}'$ and the electric field at observation point $\bar{r}$. This Green's function depends on the particular medium in which the currents are present and it incorporates the properties of this medium. In the most simple case, the medium is an infinitely extending region, homogeneously filled with for instance air, and in this case the Green's function has a particularly simple form. But the medium can also be inhomogeneously filled, including for instance various regions of different properties, and the Green's function then has a more complicated form, which depends on the size, form and number of different regions and their electromagnetic properties. The latter is the case for a microstrip antenna, in which two dielectric layers, backed by a conducting groundplane, are present in an infinite half-space filled with air.

The expression (2.1) for the radiated field can also be written in terms of a magnetic vector potential $\bar{A}$ and a scalar potential V as

$$\bar{E}^r(\bar{r}) = -j\omega\,\bar{A}(\bar{r}) - \nabla V(\bar{r}) \tag{2.2}$$

with

$$\bar{A}(\bar{r}) = \int_S \bar{\bar{G}}_A(\bar{r}/\bar{r}')\cdot\bar{J}_s(\bar{r}')\,ds' \tag{2.3}$$

and

$$V(\bar{r}) = \int_S G_V^H(\bar{r}/\bar{r}')\rho_s(\bar{r}')\,ds' \tag{2.4}$$

introducing the magnetic vector potential associated dyadic Green's function $\bar{\bar{G}}_A$ and the scalar potential associated Green's function G_V^H, which offer some numerical advantages as will be outlined in one of the forthcoming sections. In the formulation according to (2.2)-(2.4), which will be used in this report for analyzing the radiation from the two stacked microstrip patches in the presence of different dielectric layers and the groundplane, the surface charge density ρ_s, associated with the surface current density $\bar{J}_s$, is explicitly accounted for, in contrast to the formulation (2.1).

As mentioned before the unknown currents, and associated charge, flowing on the patches, as they appear in (2.3) and (2.4), have to be found in order to determine the characteristics of the antenna, e.g., the input impedance. This is done by applying the boundary condition for the tangential electric fields on the conducting patches

$$\hat{e}_z \times (\bar{E}^r(\bar{r}) + \bar{E}^e(\bar{r})) = Z_s (\hat{e}_z \times \bar{J}_s(\bar{r})) \quad \bar{r} \in S_1 \cup S_2 \tag{2.5}$$

in which $\bar{E}^e$ is the excitation field due to the coaxial feed and Z_s is the surface impedance of the conducting patches, which is introduced to account for ohmic losses on these patches. The condition (2.5) states that the total tangential electric field on the surface of the patches is proportional to the surface currents. Inserting (2.2)-(2.4) into (2.5) gives the so-called mixed potential electric field integral-equation which has to be solved to

determine the surface currents and charges.

In the formulation stated above, all quantities are given as functions of spatial coordinates. However, this particular method of analysis can be performed along two different lines. In the first one, all field quantities and currents are handled in the so-called spectral domain. After performing a Fourier-transformation with respect to the transverse coordinates, which are those coordinates in the direction parallel to the boundaries between the layers in a microstrip structure, spectral variables are introduced instead of the spatial transverse coordinates. This approach has the apparent advantage that the double spatial integration present in the integrals (2.1), (2.3) or (2.4), which can be interpreted as a sort of convolution integrals, is eliminated. Examples of this method are given in [6] for a single patch antenna and in [7][8] for a stacked patch antenna.

The other approach deals directly with the expressions (2.2)-(2.5). Although the Green's functions in this case take the form of integrals of some functions which are given in the spectral domain (Hankel-transforms), as will be shown in the forthcoming sections, once these are calculated the determination of the unknown patch currents from the integral-equation (2.5) is done in the space domain. Hence the classification of this method as a space-domain approach.

For the analysis of the dual stacked rectangular microstrip antenna we have chosen the latter approach. This method of analysis for dealing with microstrip antennas has been developed by Mosig et.al. at the Laboratoire d'Electromagnetism et d'Acoustique of the Swiss Federal Institute of Technology in Lausanne. A detailed account of the foundations of this theory, and a number of numerical techniques especially suited to this type of analysis, are extensively reviewed in several articles, applied to a single layer microstrip structure [9][10]; which are recommended reading. The first also gives a general survey on the various methods used for analyzing microstrip antennas. A short outline of this theory, applied to double-layer microstrip structures and two stacked patches, is given in [3].

Although not explicitly referenced everywhere throughout this report, the theoretical analysis presented in [9] will provide a basis for the following

extension of this theory to the case of a double-layered microstrip structure with two stacked patches, following the line of analysis presented in [3]. Also the notation used in these articles is adopted here.

Roughly the analysis of the microstrip antenna according to (2.2)-(2.5) can be divided into three main parts. First the Green's functions appearing in (2.3) and (2.4) must be determined. These can be considered as the potentials created by unit point sources, i.e., the magnetic vector potential created by a unit surface current element defines the vector potential associated Green's function $\overline{\overline{G}}_A$ and the scalar potential due to a unit point charge defines the scalar potential associated Green's function G_v^H. They will be found by using the theory of wave propagation in a plane stratified medium backed by a conducting ground plane. The second part of the analysis is the determination of the excitation field in (2.5), created in our case by a coaxial feed probe. A suitable feed model must be found and the excitation field expressed in a similar type of mixed potential form as (2.2), as a function of the currents and charges of the feed probe. Finally the integral equation (2.5) must be solved for the surface currents and charges on the patches, after which the antenna input impedance is easily obtained. Before proceeding with this, the model which will be used to describe the microstrip antenna and all its properties will be outlined in the next paragraph.

2.2 Microstrip model

In practice, a dual stacked microstrip antenna will consist of two substrate layers of finite transverse dimensions, placed on a conducting ground plane and with one patch between the two layers and the other placed on top of the structure (fig. 1.1). Especially the finite size of the structure in the transverse direction will present a great problem when one wants to calculate the electromagnetic fields within the structure. It is customary, however, to extend the substrate layers and the ground plane to infinity, creating a plane layered medium with infinite transverse dimensions (fig. 2.1).

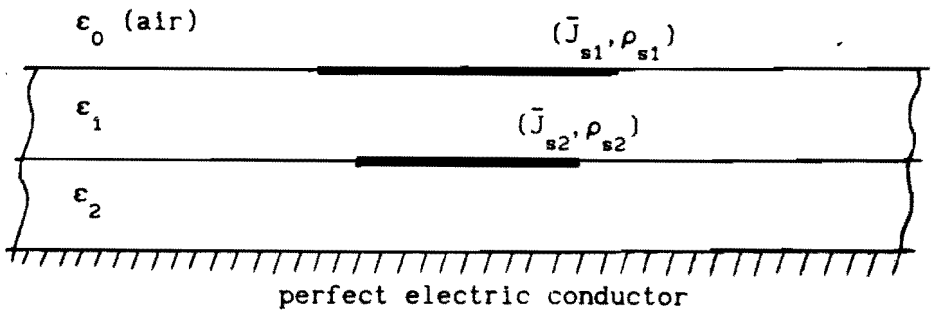

Fig. 2.1 Microstrip model

The advantage of this assumption is that the properties of the medium only vary in the direction perpendicular to the plane layers, thus making any electromagnetic boundary value problem easier to solve compared to the actual case with side boundaries between the dielectrics and air present. This assumption is validated by the fact that we are primarily interested in the so-called near-field quantities, such as resonant frequency and input impedance, which are independent of the actual transverse dimensions of the real microstrip antenna [12].

Although the entire medium is inhomogeneous, it is assumed that each dielectric layer separately is homogeneous, linear and isotropic, and that their dielectric properties are described by the complex permittivity

$$\varepsilon_i = \varepsilon_0 \varepsilon_{ri} = \varepsilon_0 \varepsilon_{ri}' (1 - j \tan \delta_i) \qquad (2.6)$$

with ε_0 the free space permittivity, ε_{ri}' the relative dielectric constant and $\tan \delta_i$ the loss-tangent for layer i; the latter being introduced for taking into account possible dielectric losses. The permeability of all dielectric layers is assumed to be that of vacuum: μ_0.

The conducting microstrip patches lie on the interfaces between air and the top dielectric layer and on the interface between the two dielectrics. In reality, surface currents are induced on both sides of the patches. However,

since the thickness of the patches is always much smaller than that of the dielectric layers, one can replace both patches by zero-thickness surface current layers $\bar{J}_{s1}$ and $\bar{J}_{s2}$ with the same dimensions as the patches; these current layers thus representing the *total* surface current flowing on the conducting microstrip patches [9]. Any ohmic losses due to the finite conductivity of the patches can be incorporated by introducing the plane-wave surface impedance [12]

$$Z_s = (1 + j)\sqrt{\frac{\mu_0 f \pi}{\sigma}} \qquad (2.7)$$

which is used in the boundary condition (2.5) on the conducting patches for formulating an integral equation for the unknown surface currents. This surface impedance is the ratio of the tangential electric field at the surface of a plane conductor with conductivity σ, and the currents flowing in this conductor, when a uniform plane wave of frequency f is incident upon the conductor [11]. The ground plane, however, is assumed, for simplicity, to be a perfect conductor ($\sigma \rightarrow \infty$).

So, the stacked microstrip antenna is modeled as a plane stratified medium, made up of three layers and backed by a perfectly conducting ground plane, with surface currents , which replace the actual conducting patches, flowing on the air-dielectric interface and on the dielectric-dielectric interface. This allows us to use the theory of wave propagation in layered media for determining the fields and potentials everywhere within this medium, due to an arbitrary distribution of currents and charges.

2.3 A horizontal electrical dipole in a layered medium

According to the formulation of the microstrip radiation problem presented in the first paragraph, the first step is to find the vector potential associated Green's function $\bar{\bar{G}}_A$ and the scalar potential associated Green's function G_v^H. These potential associated Green's functions correspond to the vector potential of an elementary electrical current and the scalar potential of a unit point charge, respectively, located on the two interfaces where

induced surface currents and charges are assumed. To determine these, we shall solve the boundary value problem of an x-directed horizontal electrical dipole (HED), arbitrarily located within the upper substrate layer (figure 2.2).

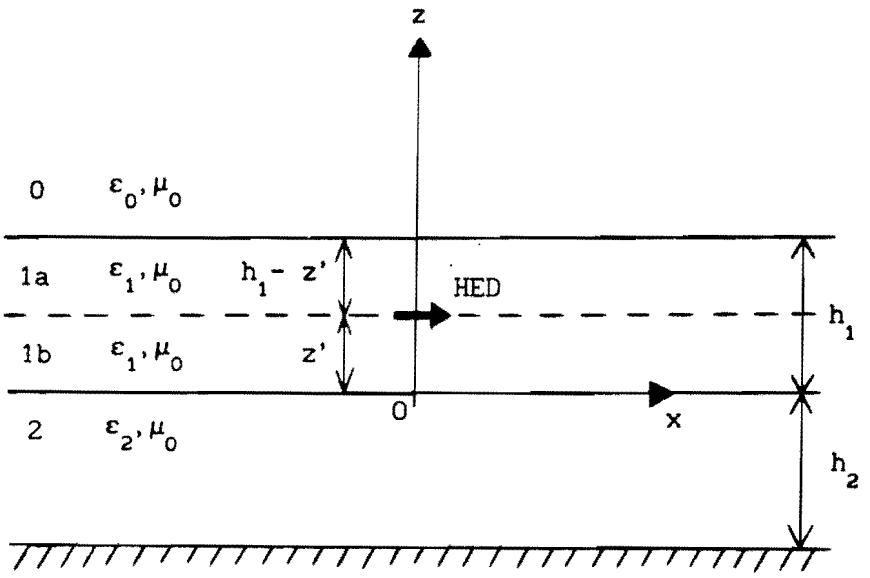

Fig. 2.2 Horizontal electrical dipole

As will be shown, the magnetic vector potential and the scalar potential of this x-directed source will be sufficient for completely determining the Green's functions appearing in (2.3) and (2.4) and thus specifying the fields in the mixed potential form (2.2) due to any arbitrary surface current distribution $\bar{J}_s$ in a plane parallel to the boundaries and located in the top dielectric layer. In two limiting cases ($z' \rightarrow h_1$ and $z' \rightarrow 0$), the fields due to any surface current flowing on the two interfaces can subsequently be obtained, which is the situation we need for our particular microstrip model. This approach can also be used for analyzing a single-patch microstrip covered with a dielectric layer or just a simple single-layer/single-patch microstrip antenna, depending on where the patch surface current distribution will be located within the layered medium.

For the coming analysis a coordinate system has been introduced (fig. 2.2) fixed to the interface of the two dielectrics, in which an arbitrary point

can be described by either rectangular (x,y,z) or circular cylindrical (ρ,ϕ,z) coordinates. The location of the HED is given $(x'=0,y'=0,z')$ with $0 \le z' \le h_1$ (primed coordinates will from here on denote source coordinates), and it is assumed to lie on the interface of two sublayers (1a and 1b) with the same dielectric properties. If the dipole moment is taken as unity, Idx = 1 [Am], the surface current density associated with the electrical dipole can be written as [9]

$$\bar{J}_s = \hat{e}_x \frac{\delta(\rho)}{2\pi\rho} \tag{2.8}$$

in circular cylindrical coordinates. Using Hankeltransforms, (2.8) can be expressed in the following integral form [13]:

$$\bar{J}_s = \hat{e}_x J_{sx} = \hat{e}_x \frac{1}{4\pi} \int_C H_0^{(2)}(k_\rho \rho)\, k_\rho\, dk_\rho \tag{2.9}$$

This particular form will prove to be very convenient because, as we will see, the vector and scalar potentials due to the HED, which will be introduced later, can be written in a similar form.

We begin our discussion, however, by first formulating the boundary value problem in terms of the electromagnetic fields $(\bar{E},\bar{H})$. If a time-harmonic dependence $\exp(j\omega t)$ of the actual time varying field quantities is assumed, then the complex fields in each separate region must satisfy the Maxwell-equations without any primary source terms:

$$\nabla \times \bar{E}_i = -j\omega\mu_0 \bar{H}_i \tag{2.10a}$$
$$\nabla \times \bar{H}_i = j\omega\varepsilon_i \bar{E}_i \tag{2.10b}$$
$$\nabla \cdot \bar{E}_i = 0 \qquad : i = 0, 1a, 1b, 2 \tag{2.10c}$$
$$\nabla \cdot \bar{H}_i = 0 \tag{2.10d}$$

At the boundaries, the tangential components of the fields are subject to the following boundary conditions:

$$z=h_1 \quad : \hat{e}_z \times (\bar{E}_0 - \bar{E}_{1a}) = \bar{0} \tag{2.11a}$$
$$\hat{e}_z \times (\bar{H}_0 - \bar{H}_{1a}) = \bar{0} \tag{2.11b}$$

$$z=z' \quad : \hat{e}_z \times (\bar{E}_{1a} - \bar{E}_{1b}) = \bar{0} \tag{2.12a}$$

$$\hat{e}_z \times (\bar{H}_{1a} - \bar{H}_{1b}) = \bar{J}_s \tag{2.12b}$$

$$z=0 \quad : \hat{e}_z \times (\bar{E}_{1b} - \bar{E}_2) = \bar{0} \tag{2.13a}$$

$$\hat{e}_z \times (\bar{H}_{1b} - \bar{H}_2) = \bar{0} \tag{2.13b}$$

$$z=-h_2 \quad : \hat{e}_z \times \bar{E}_2 = \bar{0} \tag{2.14}$$

An additional boundary condition must be imposed at infinity. This so-called radiation condition states that the field solutions must represent waves, propagating away from the sources and decaying with distance from the sources. This can be denoted as follows (Sommerfeld radiation condition) [9]:

$$\lim_{r\to\infty} r\,(\partial_r \psi + jk\psi) = 0 \tag{2.15}$$

with r being the radial coordinate in a spherical coordinate system and k the wavenumber in a particular medium. The scalar function ψ is any solution of the homogeneous Helmholtz-equation and in this case it represents the vector components of the fields $(\bar{E}_i, \bar{H}_i)$, because it follows from the Maxwell-equations (2.10) that in each region these components must satisfy the Helmholtz-equation. Together with the two-dimensional continuity equation

$$\nabla_t \cdot \bar{J}_s + j\omega\rho_s = 0 \tag{2.16}$$

in which $\nabla_t = (\partial_x, \partial_y, 0)$, relations (2.10)-(2.15) completely specify the boundary value problem for the dipole within the stratified medium, and in the presence of the perfectly conducting ground plane and an infinite half space.

The above boundary value problem can now be reduced to one in terms of potentials. Relation (2.10d) shows that we can write the magnetic field in each region as

$$\bar{H}_i = \frac{1}{\mu_0} \nabla \times \bar{A}_i \tag{2.17}$$

introducing the magnetic vector potential $\bar{A}_i$. Substituting (2.17) into (2.10a) shows that the electric field can be written as

$$\bar{E}_i = -j\omega \bar{A}_i - \nabla V_i \tag{2.18}$$

with V_i being a scalar potential which, at this point, is still arbitrary.

Introducing both (2.17) and (2.18) in (2.10b) yields

$$\nabla(\nabla\cdot\bar{A}_i) - \nabla^2 \bar{A}_i = \omega^2\mu_0\varepsilon_i\bar{A}_i - j\omega\mu_0\varepsilon_i \nabla V_i \tag{2.19}$$

If the scalar potential V_i is now specified using the well-known Lorentz-gauge

$$\nabla\cdot\bar{A}_i + j\omega\mu_0\varepsilon_i V_i = 0 \tag{2.20}$$

in each medium separately, where ε_i is independent of the spatial coordinates, the expression (2.19) shows that the magnetic vector potential is made to satisfy the homogeneous Helmholtz equation in each region. So:

$$\nabla^2\bar{A}_i + k_i^2 \bar{A}_i = 0 \tag{2.21}$$

with

$$k_i = \omega\sqrt{\mu_0\varepsilon_i} \tag{2.22}$$

being the wavenumber of medium i, i=1 for regions 1a and 1b.

Substituting (2.18) into (2.10c) and using the Lorentz-gauge (2.20) shows that the scalar potential too has to satisfy a homogeneous Helmholtz-equation in each medium according to:

$$\nabla^2 V_i + k_i^2 V_i = 0 \tag{2.23}$$

One now has to formulate the boundary conditions for both $\bar{A}$ and V. It has been shown for a single-layer microstrip structure [9], that the magnetic vector potential can be completely determined from Eqn. (2.21) and a set of boundary conditions involving only the potential $\bar{A}$ and the surface current density $\bar{J}_s$, whereas the boundary conditions for V include not only V and the surface charge distribution ρ_s, but also components of the vector $\bar{A}$. We shall therefore only formulate the boundary conditions for the magnetic vector

potential $\bar{A}$, and after $\bar{A}$ has been found use the Lorentz-gauge to determine the scalar potential V.

The boundary conditions at each boundary for $\bar{A}$ read as follows:

$z=h_1$:

$$\bar{A}_0 = \bar{A}_{1a} \tag{2.24a}$$

$$1/\varepsilon_0 \, \nabla\cdot\bar{A}_0 = 1/\varepsilon_1 \, \nabla\cdot\bar{A}_{1a} \tag{2.24b}$$

$$\hat{e}_z \times \partial_z\bar{A}_0 = \hat{e}_z \times \partial_z\bar{A}_{1a} \tag{2.24c}$$

$z=z'$:

$$\bar{A}_{1a} = \bar{A}_{1b} \tag{2.25a}$$

$$\nabla\cdot\bar{A}_{1a} = \nabla\cdot\bar{A}_{1b} \tag{2.25b}$$

$$\hat{e}_z \times [\partial_z\bar{A}_{1a} - \partial_z\bar{A}_{1b}] = -\mu_0\hat{e}_z \times \bar{J}_s \tag{2.25c}$$

$z=0$:

$$\bar{A}_{1b} = \bar{A}_2 \tag{2.26a}$$

$$1/\varepsilon_1 \, \nabla\cdot\bar{A}_{1b} = 1/\varepsilon_2 \, \nabla\cdot\bar{A}_2 \tag{2.26b}$$

$$\hat{e}_z \times \partial_z\bar{A}_{1b} = \hat{e}_z \times \partial_z\bar{A}_2 \tag{2.26c}$$

$z=-h_2$:

$$\hat{e}_z \times \bar{A}_2 = \bar{0} \tag{2.27a}$$

$$\partial_z(\hat{e}_z\cdot\bar{A}_2) = 0 \tag{2.27b}$$

For the perfectly conducting groundplane, Eqn. (2.27a) follows from (2.14) with (2.18) and using the fact that we can arbitrarily choose $V_2=0$ on the ground plane. This choice, together with the Lorentz-gauge and (2.27a) then leads to (2.27b). For the other boundaries, the conditions (2.24b), (2.25b) and (2.26b) follow from the continuity of the scalar potential across these boundaries and the Lorentz-gauge. The boundary conditions for the tangential magnetic fields, (2.11b), (2.12b) and (2.13b), together with the continuity of $\bar{A}$ finally leads to (2.24c), (2.25c) and (2.26c), respectively.

The radiation condition (2.15) must also be satisfied by the vector potential for a unique solution to exist, so:

$$\lim_{r\to\infty} r(\partial_r\bar{A}_i + jk\,\bar{A}_i) = 0 \tag{2.28}$$

since $\bar{A}_i$ is also a solution of the homogeneous Helmholtz-equation, (2.21).

The next step is to find a solution for the formulated mixed-potential boundary value problem. We therefore seek a solution for $\bar{A}$ satisfying the

wave-equation (2.21), subject to the boundary conditions (2.24)-(2.28). It can be shown that for an x-directed source we only need an x- and z-component of the magnetic vector potential to satisfy all boundary conditions [9][14]. Thus, the solution, given in both a rectangular and cylindrical coordinate system, reads:

$$\bar{A}_i = A_{xi}\hat{e}_x + A_{zi}\hat{e}_z = A_{xi}\cos\phi\ \hat{e}_\rho - A_{xi}\sin\phi\ \hat{e}_\phi + A_{zi}\hat{e}_z \qquad (2.29)$$

Substituting (2.29) and source term (2.9) into the boundary conditions (2.24)-(2.27) then gives:

$z=h_1$:

$$A_{x0} = A_{x1a} \qquad (2.30a)$$

$$A_{z0} = A_{z1a} \qquad (2.30b)$$

$$1/\varepsilon_0\ \partial_z A_{z0} - 1/\varepsilon_1\ \partial_z A_{z1a} = \cos\phi\ (1/\varepsilon_1 - 1/\varepsilon_0)\ \partial_\rho A_{x0} - 1/\rho\ \sin\phi\ (1/\varepsilon_1 - 1/\varepsilon_0)\ \partial_\phi A_{x0} \qquad (2.30c)$$

$$\partial_z A_{x0} = \partial_z A_{x1a} \qquad (2.30d)$$

$z=z'$:

$$A_{x1a} = A_{x1b} \qquad (2.31a)$$

$$A_{z1a} = A_{z1b} \qquad (2.31b)$$

$$\partial_z A_{z1a} = \partial_z A_{z1b} \qquad (2.31c)$$

$$\partial_z A_{x1a} - \partial_z A_{x1b} = -\mu_0 J_{sx} \qquad (2.31d)$$

$z=0$:

$$A_{x1b} = A_{x2} \qquad (2.32a)$$

$$A_{z1b} = A_{z2} \qquad (2.32b)$$

$$1/\varepsilon_1\ \partial_z A_{z1b} - 1/\varepsilon_2\ \partial_z A_{z2} = \cos\phi\ (1/\varepsilon_2 - 1/\varepsilon_1)\ \partial_\rho A_{x2} - 1/\rho\ \sin\phi\ (1/\varepsilon_2 - 1/\varepsilon_1)\ \partial_\phi A_{x2} \qquad (2.32c)$$

$$\partial_z A_{x1b} = \partial_z A_{x2} \qquad (2.32d)$$

$z=-h_2$:

$$A_{x2} = 0 \qquad (2.33a)$$

$$\partial_z A_{z2} = 0 \qquad (2.33b)$$

In the development of (2.24b), (2.25b) and (2.26b) into (2.30c), (2.31c) and (2.32c) in circular cylindrical coordinates, the fact has been used that because the magnetic vector potential is continuous across the boundaries, so are the partial derivatives of the vector components with respect to the transverse coordinates ρ and ϕ.

Both A_x and A_z in each medium are solutions of the homogeneous

Helmholtz-equation (2.21), which can be found by separation of variables, leading to the following solution in cylindrical coordinates:

$$H_n^{(2)}(k_\rho \rho)\left(A\, e^{jn\phi} + B\, e^{-jn\phi} \right)\left(C\, e^{-jk_{zi}z} + D\, e^{jk_{zi}z} \right) \qquad (2.34)$$

with k_ρ and k_z being the radial and axial component of the wavevector, which are related by the following expression:

$$k_\rho^2 + k_{zi}^2 = k_i^2 \qquad (2.35)$$

and parameter n being an integer due to the periodicity of the solution. Within the solution (2.34) the Hankelfunction of the second kind is chosen because together with the harmonic time dependence exp(jωt) this yields a solution which represents outward propagating waves in the radial direction.

Expression (2.34) is actually an elementary solution of the wave equation. The general solution is found by summation over all possible solutions (k_ρ, k_{zi}), and in this case the choice for an integration over the spectral variable k_ρ is made, for instance from $-\infty$ to $+\infty$ along the real axis of the complex k_ρ-plane, leading to a Hankel-transform representation of the solutions of the wave-equation. Since the spectral variable k_ρ and k_z can take on any value at this point, provided (2.35) is satisfied, the infinite integration path in the Hankel-transforms need not lie along the real axis in the k_ρ-plane. Through deformation of this path in the k_ρ-plane, the general solution for the components of the vector potentials can thus be written as:

$$\left.\begin{matrix} A_{xi} \\ A_{zi} \end{matrix}\right\} = \int_C H_n^{(2)}(k_\rho \rho)\left(A\, e^{jn\phi} + B\, e^{-jn\phi} \right)\left(C\, e^{-jk_{zi}z} + D\, e^{jk_{zi}z} \right) dk_\rho \qquad (2.36)$$

with C being an arbitrary infinite integration path in the complex k_ρ-plane. Expression (2.36) gives the solution of the wave-equation as a superposition of cylindrical waves with wavenumbers k_ρ and k_{zi} and is a form well suited to the treatment of the microstrip radiation problem. The actual choice of the integration path C and possible restrictions on the values for k_ρ and k_z for a proper evaluation of the integrals of the form (2.36) shall be dealt with later on.

Substitution of the general solution into the boundary conditions (2.30)-(2.33) and applying the radiation condition (2.28) will yield a solution for A_x and A_z. It is more convenient, however, to first solve for A_x and use this solution to obtain A_z. This can be done because A_x can be uniquely determined from the conditions (2.30a), (2.30d), (2.31a), (2.31d), (2.32a), (2.32d), (2.33a), the radiation condition (2.28) and the source term (2.9). The solution for A_z can then be found from the other boundary conditions and the radiation condition, in which the coupling between the two vector components occur in (2.30c) and (2.32c).

Substitution of (2.36) and (2.9) into (2.31d) immediately shows that within region 1 the vector component A_x is ϕ-independent, and since A_x must be continuous across the boundaries A_x, is everywhere independent of ϕ. Thus with n=0 this yields

$$A_{xi} = \int_C H_0^{(2)}(k_\rho \rho) \; [\; C_i e^{-u_i z} + D_i e^{u_i z} \;] dk_\rho \qquad (2.37)$$

in which, for notational convenience, the complex variable

$$u_i = jk_{zi} = (k_\rho^2 - k_i^2)^{1/2} \qquad (2.38)$$

is introduced for each medium.

Next we apply the radiation condition to A_x in free space. Since the Hankelfunction approaches zero for $\rho \to \infty$ we only have to look in the positive z-direction within medium 0 and it is then easy to show that the solutions represent outward propagating waves, decaying with distance from the source, if D_0=0 and if the following conditions are met:

$$Im(k_{z0}) < 0 \quad , \quad Re(k_{z0}) > 0 \qquad (2.39)$$

Substituting (2.37) and (2.9) into the boundary conditions concerning A_x, mentioned above, and considering only the z-variation then leads to the following system of equations:

$$
\begin{aligned}
C_0 e^{-u_0 h_1} &= C_{1a} e^{-u_1 h_1} + D_{1a} e^{u_1 h_1} \\
-u_0 C_0 e^{-u_0 h_1} &= -u_1 C_{1a} e^{-u_1 h_1} + u_1 D_{1a} e^{u_1 h_1} \\
C_{1a} e^{-u_1 z'} + D_{1a} e^{u_1 z'} &= C_{1b} e^{-u_1 z'} + D_{1b} e^{u_1 z'} \\
-u_1 C_{1a} e^{-u_1 z'} + u_1 D_{1a} e^{u_1 z'} + u_1 C_{1b} e^{-u_1 z'} - u_1 D_{1b} e^{u_1 z'} &= -\frac{\mu_0}{4\pi} k_\rho \qquad (2.40) \\
C_{1b} + D_{1b} &= C_2 + D_2 \\
-u_1 C_{1b} + u_1 D_{1b} &= -u_2 C_2 + u_2 D_2 \\
C_2 e^{u_2 h_2} + D_2 e^{-u_2 h_2} &= 0
\end{aligned}
$$

Solving this set of linear equations and substituting the coefficients (C_i, D_i) in (2.37) gives the solution for the x-component of the magnetic vector potential

$$
A_{x1} = \frac{\mu_0}{4\pi} \int_C H_0^{(2)}(k_\rho \rho)\, k_\rho\, f_{x1}(k_\rho, z, z')\, dk_\rho \qquad (2.41)
$$

with

$$
\begin{aligned}
f_{x0} &= \frac{T_1}{D_{TE}} e^{-u_0 (z-h_1)} && : h_1 \le z \\
f_{x1a} &= \frac{T_1}{D_{TE}} \left[\cosh u_1 (z-h_1) - \frac{u_0}{u_1} \sinh u_1 (z-h_1) \right] && : z' \le z \le h_1 \\
f_{x1b} &= \frac{T_2}{D_{TE}} \left[\cosh u_1 z + \frac{u_2}{u_1} \coth u_2 h_2 \sinh u_1 z \right] && : 0 \le z \le z' \\
f_{x2} &= \frac{T_2}{D_{TE}} \frac{\sinh u_2 (z+h_2)}{\sinh u_2 h_2} && : -h_2 \le z \le 0
\end{aligned} \qquad (2.42)
$$

$$
\begin{aligned}
T_1 &= \cosh u_1 z' + \frac{u_2}{u_1} \coth u_2 h_2 \sinh u_1 z' \\
T_2 &= \cosh u_1 (z'-h_1) - \frac{u_0}{u_1} \sinh u_1 (z'-h_1)
\end{aligned} \qquad : 0 \le z' \le h_1 \qquad (2.43)
$$

$$
D_{TE} = \cosh u_1 h_1 \, [u_0 + u_2 \coth u_2 h_2] + \sinh u_1 h_1 \, [u_1 + \frac{u_0 u_2}{u_1} \coth u_2 h_2] \qquad (2.44)
$$

The determination of A_z proceeds in a similar way. First we note that boundary conditions (2.30c) and (2.32c) and the form of A_x, (2.41), show that A_z has got a ϕ-dependence of the form: $\cos\phi$. Subsequently, the general

solution (2.36) with n=1 gives

$$A_{zi} = \cos\phi \int_C H_0^{(2)}(k_\rho \rho)\ [\ C_i e^{-u_i z} + D_i e^{u_i z}\ ] dk_\rho \qquad (2.45)$$

Due to the asymptotic behaviour of the Hankelfunction, the radiation condition in this case also yields D_0 and (2.39). Substitution of (2.45) in the appropriate boundary conditions, together with the solution for A_x (2.41)-(2.44), gives:

$$\begin{aligned}
C_0 e^{-u_0 h_1} &= C_{1a} e^{-u_1 h_1} + D_{1a} e^{u_1 h_1} \\
\frac{1}{\varepsilon_0}[-u_0 C_0 e^{-u_0 h_1}] - \frac{1}{\varepsilon_1}[-u_1 C_{1a} e^{-u_1 h_1} + u_1 D_{1a} e^{u_1 h_1}] &= \\
& \left(\frac{1}{\varepsilon_0} - \frac{1}{\varepsilon_1}\right) \frac{\mu_0}{4\pi} k_\rho^2 \frac{T_1}{D_{TE}} \\
C_{1a} e^{-u_1 z'} + D_{1a} e^{u_1 z'} &= C_{1b} e^{-u_1 z'} + D_{1b} e^{-u_1 z'} \\
-u_1 C_{1a} e^{-u_1 z'} + u_1 D_{1a} e^{u_1 z'} &= -u_1 C_{1b} e^{-u_1 z'} + u_1 D_{1b} e^{-u_1 z'} \qquad (2.46) \\
C_{1b} + D_{1b} &= C_2 + D_2 \\
\frac{1}{\varepsilon_1}[-u_1 C_{1b} + u_1 D_{1b}] - \frac{1}{\varepsilon_2}[-u_2 C_2 + u_2 D_2] &= \left(\frac{1}{\varepsilon_1} - \frac{1}{\varepsilon_2}\right) \frac{\mu_0}{4\pi} k_\rho^2 \frac{T_2}{D_{TE}} \\
-u_2 C_2 e^{u_2 h_2} + u_2 D_2 e^{-u_2 h_2} &= 0
\end{aligned}$$

The solution for the z-component of the vector potential can now be found by solving (2.46) and is given by

$$A_{zi} = -\frac{\mu_0}{4\pi} \cos\phi \int_C H_1^{(2)}(k_\rho \rho)\ k_\rho^2\ f_{zi}(k_\rho, z, z')\ dk_\rho \qquad (2.47)$$

with :

$$\begin{aligned}
f_{z0} = \frac{1}{D_{TE} D_{TM}} \Bigg[& \left(\frac{\varepsilon_2}{\varepsilon_0} - \frac{\varepsilon_2}{\varepsilon_1}\right) T_1 (\cosh u_1 h_1 + \frac{\varepsilon_1 u_2}{\varepsilon_2 u_1} \tanh u_2 h_2 \sinh u_1 h_1) \\
& + \left(\frac{\varepsilon_2}{\varepsilon_1} - 1\right) T_2 \Bigg] e^{-u_0 (z - h_1)}
\end{aligned}$$

$$f_{z1a} = \frac{1}{D_{TE} D_{TM}} \left[\left(\frac{\varepsilon_2}{\varepsilon_1} - 1 \right) T_2 \left(\cosh u_1(z-h_1) - \frac{\varepsilon_1 u_0}{\varepsilon_0 u_1} \sinh u_1(z-h_1) \right) \right.$$

$$\left. + \left(\frac{\varepsilon_2}{\varepsilon_0} - \frac{\varepsilon_2}{\varepsilon_1} \right) T_1 \left(\cosh u_1 z + \frac{\varepsilon_1 u_2}{\varepsilon_2 u_1} \tanh u_2 h_2 \sinh u_1 z \right) \right]$$

$$f_{z1b} = f_{z1a} \tag{2.48}$$

$$f_{z2} = \frac{1}{D_{TE} D_{TM}} \left[\left(\frac{\varepsilon_2}{\varepsilon_1} - 1 \right) T_2 \left(\cosh u_1 h_1 + \frac{\varepsilon_1 u_0}{\varepsilon_0 u_1} \sin u_1 h_1 \right) \right.$$

$$\left. + \left(\frac{\varepsilon_2}{\varepsilon_0} - \frac{\varepsilon_2}{\varepsilon_1} \right) T_1 \right] \frac{\cosh u_2(z+h_2)}{\cosh u_2 h_2}$$

$$D_{TM} = \cosh u_1 h_1 \left[\frac{\varepsilon_2}{\varepsilon_0} u_0 + u_2 \tanh u_2 h_2 \right] + \tag{2.49}$$

$$\sinh u_1 h_1 \left[\frac{\varepsilon_2}{\varepsilon_1} u_1 + \frac{\varepsilon_1 u_0}{\varepsilon_0 u_1} u_2 \tanh u_2 h_2 \right]$$

It is interesting to note that taking the limit $z' \to h_1$ in the boundary conditions (2.40) and (2.46), and subsequently eliminating the coefficients for sublayer 1a, yields the boundary conditions for a HED located on the interface of the upper dielectric and air. The boundary conditions for a HED located on the interface of the two dielectrics can be found in a similar way by taking the limit $z' \to 0$. This shows that the potentials for electrical dipoles in these two limiting cases can be obtained from the general solutions (2.41)-(2.44), (2.47)-(2.49) for a HED, arbitrarily located within the upper dielectric, without having to formulate and solve the boundary value problem for these two cases separately, thus saving a considerable amount of work. These two cases are of importance, because they lead to the Green's functions for surface current/charge distributions located on the interfaces mentioned, as they appear in our stacked microstrip model. Taking the limits $z' \to 0$ and $h_1 \to 0$ and eliminating the coefficients for medium 1 yields the boundary conditions for a HED located on the air-dielectric interface for a single-layer microstrip structure. And it can also be shown that with these limits the potentials found for a two-layer structure, Eqns. (2.41)-(2.44),(2.47)-(2.49), agree with those found directly for a single-layer microstrip structure, as presented in [9].

The scalar potential V in each medium can now easily be obtained using the Lorentz-gauge (2.20), which in cylindrical coordinates reads:

$$V_i = - \frac{1}{j\omega \mu_0 \varepsilon_i} \left[\cos\phi \, \partial_\rho A_{xi} + \partial_z A_{zi} \right] \tag{2.50}$$

Substitution of (2.41)-(2.44), (2.47)-(2.49) then yields

$$V_i = \frac{\cos\phi}{4\pi j\omega\varepsilon_i} \int_C H_1^{(2)}(k_\rho \rho) \, k_\rho^2 \, f_{vi}(k_\rho, z, z') \, dk_\rho \tag{2.51}$$

with

$$f_{vi} = f_{xi} + \partial_z f_{zi} \tag{2.52}$$

Because the functions appearing in (2.51) are needed elsewhere, they will be listed here for reference purposes:

$$\begin{aligned}
f_{v0} &= \frac{1}{D_{TE} D_{TM}} \left[-u_0 \left(\frac{\varepsilon_2}{\varepsilon_0} - \frac{\varepsilon_2}{\varepsilon_1} \right) T_1 \left(\cosh u_1 h_1 + \frac{\varepsilon_1 u_2}{\varepsilon_2 u_1} \tanh u_2 h_2 \sinh u_1 h_1 \right) \right. \\
&\qquad \left. -u_0 \left(\frac{\varepsilon_2}{\varepsilon_1} - 1 \right) T_2 + D_{TM} T_1 \right] e^{-u_0 (z-h_1)} \\
f_{v1a} &= \frac{1}{D_{TE} D_{TM}} \left[D_{TM} T_1 \left(\cosh u_1 (z-h_1) - \frac{u_0}{u_1} \sinh u_1 (z-h_1) \right) \right. \\
&\qquad + u_1 \left(\frac{\varepsilon_2}{\varepsilon_1} - 1 \right) T_2 \left(\sinh u_1 (z-h_1) - \frac{\varepsilon_1 u_0}{\varepsilon_0 u_1} \cosh u_1 (z-h_1) \right) \\
&\qquad \left. + u_1 \left(\frac{\varepsilon_2}{\varepsilon_0} - \frac{\varepsilon_2}{\varepsilon_1} \right) T_1 \left(\sinh u_1 z + \frac{\varepsilon_1 u_2}{\varepsilon_2 u_1} \tanh u_2 h_2 \cosh u_1 z \right) \right] \\
f_{v1b} &= \frac{1}{D_{TE} D_{TM}} \left[D_{TM} T_2 \left(\cosh u_1 z + \frac{u_2}{u_1} \coth u_2 h_2 \sinh u_1 z \right) \right. \\
&\qquad + u_1 \left(\frac{\varepsilon_2}{\varepsilon_1} - 1 \right) T_2 \left(\sinh u_1 (z-h_1) - \frac{\varepsilon_1 u_0}{\varepsilon_0 u_1} \cosh u_1 (z-h_1) \right) \\
&\qquad \left. + u_1 \left(\frac{\varepsilon_2}{\varepsilon_0} - \frac{\varepsilon_2}{\varepsilon_1} \right) T_1 \left(\sinh u_1 z + \frac{\varepsilon_1 u_2}{\varepsilon_2 u_1} \tanh u_2 h_2 \cosh u_1 z \right) \right] \\
f_{v2} &= \frac{1}{D_{TE} D_{TM}} \left[u_2 \tanh u_2 h_2 \left[\left(\frac{\varepsilon_2}{\varepsilon_1} - 1 \right) T_2 \left(\cosh u_1 h_1 + \frac{\varepsilon_1 u_0}{\varepsilon_0 u_1} \sin u_1 h_1 \right) \right. \right. \\
&\qquad \left. \left. + \left(\frac{\varepsilon_2}{\varepsilon_0} - \frac{\varepsilon_2}{\varepsilon_1} \right) T_1 \right] + D_{TM} T_2 \right] \frac{\sinh u_2 (z+h_2)}{\sinh u_2 h_2}
\end{aligned} \tag{2.53}$$

The derivation given above for an x-directed horizontal electrical dipole can also be given for an y-directed dipole, because the latter is also needed for formulating the Green's functions since any surface current has both x- and y-components. Due to the rotational symmetry, however, the potentials for an y-directed source can be directly obtained from those for an x-directed source. An y-directed HED gives rise to an y- and z-component of the magnetic vector potential. These components and also the associated scalar potential can be found from (2.41), (2.47) and (2.51) by substituting $\phi - \pi/2$ for ϕ, see figure 2.3.

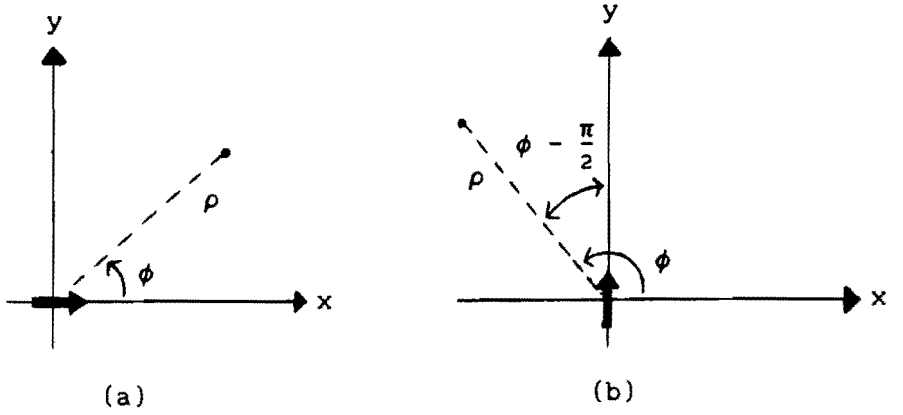

Fig. 2.3 Top view x- and y-directed dipoles, located in the transverse x-y-plane

For making a distinction between the potentials due to an x- and y-directed HED, the superscripts x and y will be added. The potentials for both types of dipoles then read as follows:

$$A^x_{xi} = A^y_{yi} = \frac{\mu_0}{4\pi} \int_C H_0^{(2)}(k_\rho \rho)\, k_\rho\, f_{xi}(k_\rho, z, z')\, dk_\rho \qquad (2.54)$$

$$\frac{A^x_{zi}}{\cos\phi} = \frac{A^y_{zi}}{\sin\phi} = -\frac{\mu_0}{4\pi} \int_C H_1^{(2)}(k_\rho \rho)\, k_\rho^2\, f_{zi}(k_\rho, z, z')\, dk_\rho \qquad (2.55)$$

$$\frac{V^x_i}{\cos\phi} = \frac{V^y_i}{\sin\phi} = \frac{1}{4\pi j\omega\varepsilon_i} \int_C H_1^{(2)}(k_\rho \rho)\, k_\rho^2\, f_{vi}(k_\rho, z, z')\, dk_\rho \qquad (2.56)$$

According to the Green's function formulation of the fields radiated by an arbitrary surface current distribution in a layered medium, (2.2)-(2.4), the magnetic vector potential is found by a superposition integral of the surface currents, weighted by a dyadic Green's function $\overline{\overline{G}}_A$. This Green's function is made up of the magnetic vector potentials of x- and y-directed current elements, i.e., unit moment electrical dipoles. The scalar potential, on the other hand, is found in terms of a superposition integral of the surface charge distribution, weighted by the Green's function G_v^H, in which G_v^H can be seen as the scalar potential created by a unit point charge. This potential can be found from the scalar potential of a HED. The charge associated with a HED are, through the continuity equation (2.16), two point charges of strength $\pm$ I/jω located on either end of the dipole. If we now define the scalar potential of a time harmonic unit point charge V_{qi}^H, associated with a time harmonic *horizontal* electrical dipole, according to

$$V_i^x = - \frac{1}{j\omega} \partial_x V_{qi}^H = - \frac{1}{j\omega} \cos\phi \, \partial_\rho V_{qi}^H \qquad (2.57a)$$

or

$$V_i^y = - \frac{1}{j\omega} \partial_y V_{qi}^H = - \frac{1}{j\omega} \sin\phi \, \partial_\rho V_{qi}^H \qquad (2.57b)$$

then this choice leads to the desired mixed potential form (2.2)-(2.4), as will be shown in the next section. Substitution of (2.56) into (2.57) gives:

$$V_{qi}^H = \frac{1}{4\pi\varepsilon_i} \int_C H_0^{(2)}(k_\rho \rho) \, k_\rho \, f_{vi}(k_\rho, z, z') \, dk_\rho \qquad (2.58)$$

This scalar potential and the potentials of the two horizontal electrical dipoles, (2.54)-(2.56), provide all the necessary expressions with which one can find the fields due to an arbitrary surface current distribution, flowing on a transverse plane $z = z'$, located anywhere within the top dielectric layer of a two-layer microstrip structure, in terms of the so-called potential associated Green's functions $\overline{\overline{G}}_A$ and G_v^H, which will be the subject of the next section.

2.4 Radiated fields due to an arbitrary surface current distribution

If, instead of a single elementary current source, an arbitrary surface current layer is present in the z = z'-plane, then it is straightforward to think of this current layer as being build up from an infinite amount of those elementary sources. Simple summation or superposition of the contributions to the various potentials of all elements then gives the total potentials and hence the radiated fields. To this end we first need to obtain the potentials of the elementary sources, described in the last section where they were fixed to the z-axis, arbitrarily located within the z'-plane. Because the properties of the layered medium only vary in the z-direction, the potentials are invariant to a translation in the transverse direction. For a HED located on the z-axis (figure 2.4a), the potentials depend, in the transverse direction, on the radial distance ρ between source and observation point and the angle ϕ between the observation vector $\bar{\rho}$ and the x-axis.

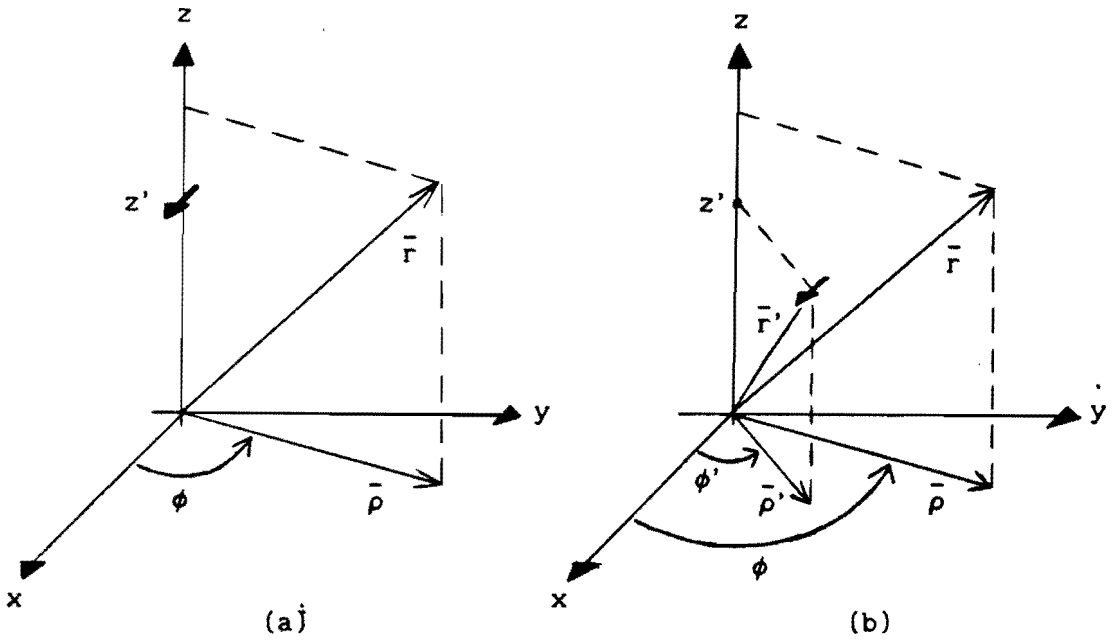

Fig. 2.4 Dipole position: a) fixed to z-axis and b) arbitrarily located in the z=z'-plane

After performing a translation of the HED's toward source point $\bar{r}' = (x', y', z') = (\rho', \phi', z')$, it is obvious (Fig. 2.4b) that in the

expressions for the potentials we merely have to replace ρ and ϕ by

$$\xi = | \bar{\rho} - \bar{\rho}' | \tag{2.59a}$$

and

$$\zeta = \sin^{-1}[(\rho\sin\phi - \rho'\sin\phi')/\xi] \tag{2.59b}$$

to obtain the potentials at any observation point $\bar{r} = (x,y,z) = (\rho,\phi,z)$ for a source located at source point $\bar{r}' = (x',y',z') = (\rho',\phi',z')$ with $0 \leq z' \leq h_1$.

The scalar potential of both an x- and y-directed dipole are then given by:

$$\frac{V_i^x(\bar{r}/\bar{r}')}{\cos\zeta} = \frac{V_i^y(\bar{r}/\bar{r}')}{\sin\zeta} = \frac{1}{4\pi j\omega\varepsilon_i} \int_C H_1^{(2)}(k_\rho\xi)\, k_\rho^2\, f_{vi}(k_\rho,z,z')\, dk_\rho \tag{2.60}$$

In view of the Green's function formulation the components of the magnetic vector potential shall, from here on, be denoted as

$$G_{Ai}^{xx}(\bar{r}/\bar{r}') = G_{Ai}^{yy}(\bar{r}/\bar{r}') = \frac{\mu_0}{4\pi} \int_C H_0^{(2)}(k_\rho\xi)\, k_\rho\, f_{xi}(k_\rho,z,z')\, dk_\rho \tag{2.61}$$

for the x- and y-components, and

$$\frac{G_{Ai}^{zx}(\bar{r}/\bar{r}')}{\cos\zeta} = \frac{G_{Ai}^{zy}(\bar{r}/\bar{r}')}{\sin\zeta} = -\frac{\mu_0}{4\pi} \int_C H_1^{(2)}(k_\rho\xi)\, k_\rho^2\, f_{zi}(k_\rho,z,z')\, dk_\rho \tag{2.62}$$

for the z-components. The scalar potential of a time harmonic point charge shall be written as

$$G_{vi}^{H}(\bar{r}/\bar{r}') = \frac{1}{4\pi\varepsilon_i} \int_C H_0^{(2)}(k_\rho\xi)\, k_\rho\, f_{vi}(k_\rho,z,z')\, dk_\rho \tag{2.63}$$

with the superscript H indicating that the single point charge is associated with a *horizontal* electrical dipole.

Suppose now that a surface current $\bar{J}_s$ exists, lying in the z=z'-plane in the

upper dielectric layer, non-zero over an arbitrary plane surface S' and zero everywhere outside S'. Dividing S' into an infinite amount of differential surface elements ds'=dx'dy', we can think of $\bar{J}_s$ as a collection of horizontal electrical dipoles, i.e., an x-directed dipole with electric current $J_{sx}dy'$ and length dx' and an y-directed dipole with current $J_{sy}dx'$ and of length dy' on each differential element ds' (dipole moments $J_{sx}ds'$ and $J_{sy}ds'$, respectively). Superposition then gives for the total scalar potential of this collection of elementary dipoles:

$$V_i(\bar{r}) = \int_{S'} \{ J_{sx}(\bar{r}')\, V_i^x(\bar{r}/\bar{r}') + J_{sy}(\bar{r}')\, V_i^y(\bar{r}/\bar{r}') \}\, ds' \qquad (2.64)$$

Substituting Eqns. (2.57) for an arbitrarily located dipole in (2.64) yields:

$$V_i(\bar{r}) = -\frac{1}{j\omega} \int_{S'} \nabla_t G^H_{vi}(\bar{r}/\bar{r}')\cdot\bar{J}_s(\bar{r}')\, ds' \qquad (2.65)$$

Using the identity from vector calculus: $\nabla\cdot(A\bar{B}) = \bar{B}\cdot\nabla A + A\nabla\cdot\bar{B}$, the fact that $\nabla_t G^H_v = -\nabla_{t'} G^H_v$ (see Eqn. (2.63) with (2.59a)), and the continuity equation (2.16), equation (2.65) can be written as:

$$V_i(\bar{r}) = \frac{1}{j\omega}\int_{S'} \nabla_{t'}\cdot[G^H_{vi}(\bar{r}/\bar{r}')\bar{J}_s(\bar{r}')]ds' + \int_{S'} G^H_{vi}(\bar{r}/\bar{r}')\rho_s(\bar{r}')ds' \qquad (2.66)$$

Application of the two-dimensional Gauss-theorem to the first term on the right-hand-side of (2.66) gives

$$\int_{S'} \nabla_{t'}\cdot[G^H_{vi}(\bar{r}/\bar{r}')\bar{J}_s(\bar{r}')]ds' = \oint_{L'} [G^H_{vi}(\bar{r}/\bar{r}')\bar{J}_s(\bar{r}')]\cdot\hat{n}\, dl' \qquad (2.67)$$

with L' being the contour of S', and $\hat{n}$ the unit vector, normal to L', and lying in the plane S'. Since the normal component of the current will be zero on the boundary of surface S', $\bar{J}_s\cdot\hat{n} = 0$ on L', this line integral will become zero. We thus find for the scalar potential for a given surface current /charge distribution $(\bar{J}_s, \rho_s)$:

$$V_i(\bar{r}) = \int_{S'} G^H_{vi}(\bar{r}/\bar{r}')\rho_s(\bar{r}')ds' \qquad (2.68)$$

This shows that the definition of the scalar potential of a single time harmonic unit point charge associated with a horizontal current element,

according to Eqn. (2.57), indeed leads to the scalar potential associated Green's function G_v^H, linking the charges, associated with a surface current distribution, to the total scalar potential V. All the properties of the medium, such as the different layers, their dielectric properties and the perfectly conducting ground plane, are incorporated in the Green's function G_v^H.

The total magnetic vector potential can also be found by summation of all the contributions from all differential surface current elements, leading to:

$$\bar{A}_i(\bar{r}) = \int_{S'} \{\hat{e}_x\, G_{Ai}^{xx}(\bar{r}/\bar{r}')J_{sx}(\bar{r}') + \hat{e}_y\, G_{Ai}^{yy}(\bar{r}/\bar{r}')J_{sy}(\bar{r}') + \hat{e}_z\, [G_{Ai}^{zx}(\bar{r}/\bar{r}')J_{sx}(\bar{r}') + G_{Ai}^{zy}(\bar{r}/\bar{r}')J_{sy}(\bar{r}')]\ \}\, ds' \qquad (2.69)$$

This can be written in a more compact form as:

$$\bar{A}_i(\bar{r}) = \int_{S'} \bar{\bar{G}}_{Ai}(\bar{r}/\bar{r}')\cdot\bar{J}_s(\bar{r}')ds' \qquad (2.70)$$

in which the dyadic Green's function $\bar{\bar{G}}_A$ is introduced according to

$$\bar{\bar{G}}_{Ai} = \hat{e}_x\hat{e}_x\, G_{Ai}^{xx} + \hat{e}_y\hat{e}_y\, G_{Ai}^{yy} + \hat{e}_z\hat{e}_x\, G_{Ai}^{zx} + \hat{e}_z\hat{e}_y\, G_{Ai}^{zy} \qquad (2.71)$$

or in matrix form as

$$\begin{pmatrix} G_{Ai}^{xx} & 0 & 0 \\ 0 & G_{Ai}^{yy} & 0 \\ G_{Ai}^{zx} & G_{Ai}^{zy} & 0 \end{pmatrix} \qquad (2.72)$$

The electromagnetic fields, radiated by the surface current layer $\bar{J}_s$, can now easily be found from Eqns. (2.17) and (2.18)

$$\bar{H}_i^r(\bar{r}) = \frac{1}{\mu_0}\,\nabla \times \int_{S'} \bar{\bar{G}}_{Ai}(\bar{r}/\bar{r}')\cdot\bar{J}_s(\bar{r}')ds' \qquad (2.73)$$

$$\bar{E}_i^r(\bar{r}) = -j\omega\int_{S'} \bar{\bar{G}}_{Ai}(\bar{r}/\bar{r}')\cdot\bar{J}_s(\bar{r}')ds' - \nabla \int_{S'} G_{vi}^H(\bar{r}/\bar{r}')\rho_s(\bar{r}')ds' \qquad (2.74)$$

in which index i depends on the particular layer in which the fields are evaluated at observation point $\bar{r}$.

For a surface current flowing on either the interface of the top dielectric layer and air or on the interface of both dielectric layers, or on both interfaces, appropriate limits must be taken in the Green's functions appearing in (2.73)-(2.74) with regards to the source vector $\bar{r}'$, $z' \rightarrow h_1$ and $z' \rightarrow 0$. In the case of surface currents present on both interfaces, the surface of integration S' must obviously be the union of the surfaces occupied by both current distributions.

A point worth mentioning here is why the potentials $\bar{A}$ and V are used to describe the fields, instead of calculating them directly, the latter resulting in the fields given by superposition integrals in terms of only the electric currents, weighted by electric- and magnetic-field associated Green's functions, as in Eqn. (2.1). This is because the potential associated Green's functions exhibit spatial singularities of type r^{-1}, see [11,p.160] for the homogeneous case, whereas the electromagnetic field associated Green's functions exhibit higher order spatial singularities [9]. The integrals appearing in (2.73)-(2.74) thus exist and the numerical evaluation of them will present no major difficulties.

2.5 Excitation field due to a coaxial feed

In the previous two sections the field radiated by a surface current layer or multiple surface current layers in a plane stratified medium were derived. These surface currents correspond to those induced on the microstrip patches under the influence of some sort of excitation field. It is the purpose of the theory presented this section to obtain the excitation fields as they occur when the microstrip antenna is excited by a coaxial feed probe, after which the unknown surface currents can be found by imposing boundary condition (2.5) on the conducting patches.

Real coaxial feeds consist of an inner conductor of finite diameter, carrying the source current to one of the patches, and an outer conductor connected to the conducting groundplane (Fig. 1.1). The electromagnetic modeling of these feeds is rather involved [9], so we shall resort to a simpler model for the coaxial feed which nevertheless must still provide sufficient accuracy. One of the possibilities of modeling the coaxial feed is to think of the microstrip antenna as being excited by the entire vertical inner conductor of the coaxial probe and make assumptions with regard to the currents flowing on this wire, from which the excitation fields then must be calculated [9]. We shall use here the thin wire-thin substrate approximation, in which the azimuthal currents on the probe can be neglected because its radius is much smaller than the wavelength and in which the longitudinal currents are assumed to be uniform, because in most cases the thickness of the substrate is small compared to the wavelength.

The coaxial feed shall thus be represented by a vertical current filament of zero-thickness (delta-excitation), extending from the groundplane to the interface of the two dielectric layers and of uniform current I, which is a first order approximation of real coaxial probes [15]. The excitation field $\bar{E}^e$ is defined as being the field due to this source, which exists within the microstrip structure without the presence of the conducting patches.

The derivation of the excitation field is performed by invoking Lorentz-reciprocity theorem to the situation depicted in figure 2.5., and is based on the theory presented in [16].

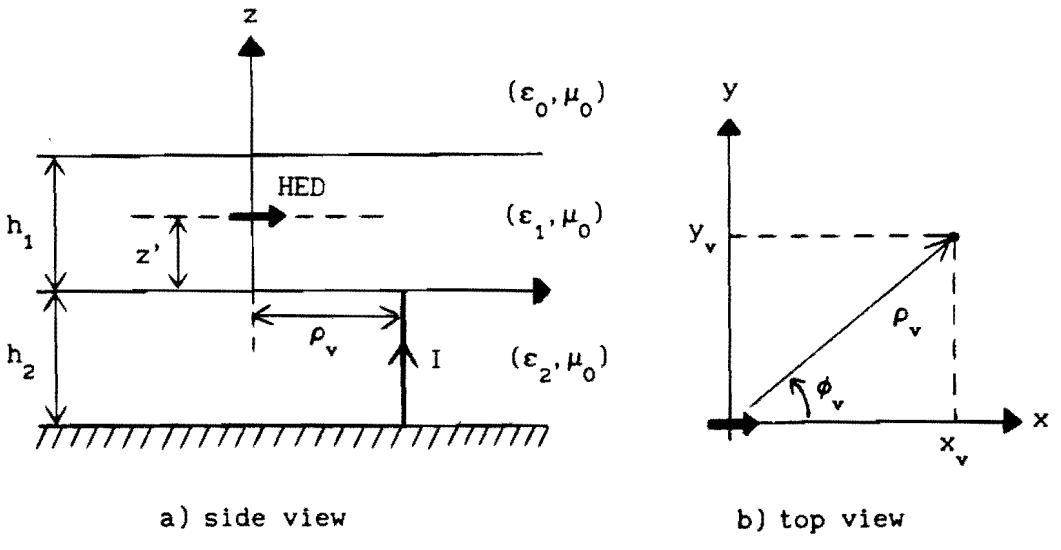

a) side view b) top view

Fig. 2.5 Horizontal dipole and vertical current in a layered medium; a) side view, b) top view

Within the layered microstrip structure there are two source distributions present. First there is a source H, which is an x-directed horizontal electrical dipole with dipole moment Idx = 1 [Am]. The volume current density associated with this source can thus be given by

$$\bar{J}^H = \hat{e}_x \, Idx \, \delta(\bar{r} - \bar{r}_H) = \hat{e}_x \, \delta(\bar{r} - \bar{r}_H) \tag{2.75}$$

with $\bar{r}_H = (0,0,z')$, $0 \leq z' \leq h_1$. The second source is one termed source V, and is a vertical filament of current I extending from $z=-h_2$ to $z=0$. The volume current density of this source reads

$$\bar{J}^V = \hat{e}_z \, I \, \delta(x - x_v) \, \delta(y - y_v) \tag{2.76}$$

and its transverse location with respect to the local coordinate system is $\bar{\rho}_v = (x_v, y_v) = (\rho_v, \phi_v)$.

The Lorentz-reciprocity theorem links the fields produced by source V and evaluated at the volume V_H occupied by source H to the fields due to

source H, evaluated at the volume V_v occupied by source V [25], according to

$$\int_{V_H} \bar{E}^V \cdot \bar{J}^H \, dV = \int_{V_v} \bar{E}^H \cdot \bar{J}^V \, dV \tag{2.77}$$

if only electric current sources are present within the volumes. The electric field due to source H is known everywhere throughout the layered medium, Eqns. (2.18), (2.29), (2.41)-(2.44), (2.47)-(2.49), (2.51) and (2.53), and is given by:

$$\bar{E}^H = -j\omega \, \bar{A}^H - \nabla \, V^H = -j\omega \begin{pmatrix} A_x^H \\ 0 \\ A_z^H \end{pmatrix} - \begin{pmatrix} \partial_x V^H \\ \partial_y V^H \\ \partial_z V^H \end{pmatrix} \tag{2.78}$$

Substitution of (2.78) into (2.77) then yields the unknown electric field $\bar{E}^V$, evaluated at $\bar{r}_H$. We want, however, the excitation field also in terms of a magnetic vector potential $\bar{A}^V$ and a scalar potential V^V. Therefore we can write

$$\bar{E}^V = -j\omega \, \bar{A}^V - \nabla \, V^V = -j\omega \begin{pmatrix} 0 \\ 0 \\ A_z^V \end{pmatrix} - \begin{pmatrix} \partial_x V^V \\ \partial_y V^V \\ \partial_z V^V \end{pmatrix} \tag{2.79}$$

since vertical currents only gives rise to a z-component of the magnetic vector potential [14][16].

Applying the Lorentz-theorem to the fields (2.78), (2.79) and the current distributions (2.75) and (2.76) then gives

$$E_x^V(\bar{r}_H) = \int_{-h_2}^{0} I \, E_z^H(\bar{\rho}_V, z) \, dz \tag{2.80}$$

and with the potentials inserted

$$-\partial_x V^V(\bar{r}_H) = -j\omega I \int_{-h_2}^{0} A_z^H(\bar{\rho}_V, z) \, dz - I \int_{-h_2}^{0} \partial_z V^H(\bar{\rho}_V, z) \, dz \tag{2.81}$$

Assuming a unit current (I = 1A), (2.81) can be developed as follows:

$$-\partial_x V^V(\bar{r}_H) = -j\omega I \int_{-h_2}^{0} A_z^H(\bar{\rho}_V, z)\, dz - V^H(\bar{\rho}_V, Z=0) + V^H(\bar{\rho}_V, z=-h_2)$$

$$= -j\omega I \int_{-h_2}^{0} A_z^H(\bar{\rho}_V, z)\, dz - V^H(\bar{\rho}_V, Z=0) \qquad (2.82)$$

since the scalar potential V^H is assumed to vanish on the groundplane. The expressions for A_z^H and V^H are known for observation points in medium 2, Eqns. (2.41) and (2.51), with which (2.82) gives:

$$-\partial_x V^V(\bar{r}_H) = -\frac{\cos\phi_V}{4\pi j\omega\varepsilon_2} \int_C H_1^{(2)}(k_\rho \rho_V)\, k_\rho^2 \left\{ k_2^2 \int_{-h_2}^{0} f_{z2}(k_\rho, z, z')\, dz + f_{v2}(k_\rho, z=0, z') \right\} dk_\rho \qquad (2.83)$$

The partial derivative appearing on the left-hand-side of (2.83) is given with respect to the observation point of source V, which are the source coordinates of source H. This in contrast to the coordinates appearing on the right-hand-side, which are the observation coordinates of source H and at the same time the source coordinates of source V. To perform the partial integration, one must remember that in actual fact the radial dependence of a certain quantity, such as the scalar potential, for a source at $\bar{\rho}'$ and evaluated at $\bar{\rho}$ is of the form $|\bar{\rho} - \rho'|$. This means that the radial dependence on the left hand side must be interpreted as $|\bar{\rho}_H - \bar{\rho}_V|$ and that on the right hand side as $|\bar{\rho}_V - \bar{\rho}_H|$. A minus sign must thus be introduced to carry out the partial integration with respect to $\bar{\rho}_V$, leading to:

$$V^V(\bar{r}_H) = \frac{1}{4\pi j\omega\varepsilon_2} \int_C H_0^{(2)}(k_\rho \rho_V)\, k_\rho \left\{ k_2^2 \int_{-h_2}^{0} f_{z2}(k_\rho, z, z')\, dz + f_{v2}(k_\rho, z=0, z') \right\} dk_\rho \qquad (2.84)$$

This scalar potential, due to the vertical current element with I = 1 [A], can be associated with the charge distribution corresponding to that current

element, which, according to the continuity equation, consists of a point charge of strength $+I/j\omega$, located at z=0, and a point charge of strength $-I/j\omega$ at $z=-h_2$. The latter will disappear because of the groundplane, so Eqn. (2.84) can be thought of as being the scalar potential of a single time harmonic point charge situated on the interface of the two dielectric layers at $\bar{\rho}_v = (x_v, y_v) = (\rho_v, \phi_v)$. Taking into account the translational invariance of the medium and the fact that, as far as the radial dependence is concerned, Eqn. (2.84) only depends on the radial distance between source and observer, we find for an arbitrarily located *unit* time harmonic point charge

$$G_v^v(\bar{r}/\bar{r}') = \frac{1}{4\pi\varepsilon_2} \int_C H_0^{(2)}(k_\rho \xi)\, k_\rho\, f_{v1}^v(k_\rho, z)\, dk_\rho \qquad (2.85)$$

with which we define the scalar Green's function of point charges which are associated with *vertical* currents, as opposed to the one introduced for charges associated with *horizontal* currents, Eqn. (2.63). The function f_{v1}^v appearing in (2.85) can be found from the term in brackets in (2.84) by substituting the expressions (2.48) and (2.53), and, after performing the integration involved, making the change of variables $z' \rightarrow z$, because the former source coordinates for the dipole are now observation coordinates for the vertical point charge. This all leads to

$$f_{v1}^v = \frac{1}{D_{TE} D_{TM}} \frac{1}{u_2} \left[T_3 (\cosh u_1(z-h_1) - \frac{u_0}{u_1} \sinh u_1(z-h_1)) \right.$$
$$\left. + (\frac{\varepsilon_2}{\varepsilon_0} u_0^2 - \frac{\varepsilon_2}{\varepsilon_1} u_1^2) \tanh u_2 h_2 \, (\cosh u_1 z + \frac{u_2}{u_1} \coth u_2 h_2 \sinh u_1 z) \right]$$

with

$$T_3 = \cosh u_1 h_1 \, (\frac{\varepsilon_2}{\varepsilon_0} u_0 u_2 + \frac{\varepsilon_2}{\varepsilon_1} u_1^2 \tanh u_2 h_2) \qquad (2.86)$$
$$+ \sinh u_1 h_1 \, (\frac{\varepsilon_2}{\varepsilon_1} u_1 u_2 + \frac{\varepsilon_2}{\varepsilon_0} u_0 u_1 \tanh u_2 h_2)$$

It must be stressed that in this case the location of the source is fixed to the interface of the two dielectric layers, $\bar{r}' = \bar{\rho}'$, and that the scalar potential is only known within the top dielectric layer, $0 \leq z \leq h_1$. But, since the coaxial feed is connected to the lower patch and we are only

interested in the fields on both patches, $z = 0$ and $z = h_1$, this will suffice.

Because we only need to know the tangential components of the excitation field, the z-component of the magnetic vector potential of the vertical current in (2.79) is not relevant. The tangential excitation field then follows simply from Eqn. (2.85), multiplied by $I/j\omega$ for an excitation current of strength I, and inserted in (2.79), giving:

$$\bar{E}^{e}_{tang}(\bar{r}) = - \frac{I}{j\omega} \nabla_t G^{v}_{v}(\bar{r}/\bar{r}') \qquad (2.87)$$

A question which might arise, is why the scalar potential of a time harmonic point charge, associated with a vertical current filament, is explicitly derived here, instead of just using the scalar potential (2.63) for a point charge, associated with a horizontal current, the latter then lying on the lower interface. This is because these two potentials are not equivalent; a contradiction which arises from the choices which are made for the form of the magnetic vector potentials for horizontal and vertical currents, i.e., $(A_x,0,A_z)$ for an x-directed source and $(0,0,A_z)$ for a z-directed source, which apparently are not unique [17]. If, however, it is distinctly stated to which type of current the charge belongs for which the scalar potentials are derived, the formulation given is theoretically correct.

2.6 The mixed-potential electric field integral equation

Now that the relationships are established between the microstrip patch currents and its radiated fields and between the feed current and its tangential excitation field, it is possible to try and solve for the patch currents by setting up an integral-equation, in which the patch surface currents appear as the unknowns. The total electric field, i.e., the sum of the radiated and excitation field, is made to satisfy a boundary condition on the surface of the good, but not necessarily perfectly, conducting microstrip patches. As outlined in the first section, the boundary condition for the tangential electric field is given by Eqn. (2.5).

Let's first examine the fields radiated by two surface current layers on both interfaces, corresponding to the currents induced on the patches. If a surface current $\bar{J}_{s1}$ is present on a surface S_1 on the air-dielectric interface and a surface current $\bar{J}_{s2}$ is present on a surface S_2 on the dielectric-dielectric interface, as in figure 2.1, then the radiated field follows from (2.74) with $S' = S_1 \cup S_2$, $\bar{J}_s = \bar{J}_{s1} + \bar{J}_{s2}$ and $\rho_s = \rho_{s1} + \rho_{s2}$;

$$E_i^r(\bar{r}) = -\sum_{j=1}^{2}\left\{ j\omega\int_{S_j} \bar{\bar{G}}_{Ai}(\bar{r}/\bar{r}_j)\cdot\bar{J}_{sj}(\bar{r}_j)ds_j + \nabla\int_{S_j} G_{vi}^H(\bar{r}/\bar{r}_j)\rho_{sj}(\bar{r}_j)ds_j \right\} \quad (2.88)$$

with $\bar{r}_1$ and $\bar{r}_2$ being the position-vectors of the microstrip patches S_1 and S_2, respectively. Within the Green's functions (2.61)-(2.63) the appropriate limits for the source-plane $z = z'$ thus have to be taken to arrive at the Green's functions appearing in (2.88).

Substitution of (2.88) and the tangential excitation field (2.87), for a coaxial feed, carrying a current I, attached to the lower patch at $\bar{r}_c = (x_c, y_c, 0)$ into boundary condition (2.5) gives

$$-\frac{I}{j\omega}\nabla_t G_v^v(\bar{r}/\bar{r}_c) = \sum_{j=1}^{2}\left\{ j\omega\int_{S_j}\bar{\bar{G}}_A(\bar{r}/\bar{r}_j)\cdot\bar{J}_{sj}(\bar{r}_j)ds_j + \nabla_t\int_{S_j} G_v^H(\bar{r}/\bar{r}_j)\rho_{sj}(\bar{r}_j)ds_j + Z_s\bar{J}_{sj}(\bar{r}) \right\} \quad (2.89)$$

$$\bar{r} \in S_1 \cup S_2$$

with

$$\bar{J}_s(\bar{r}) = J_{sx}(\bar{r})\,\hat{e}_x + J_{sy}(\bar{r})\,\hat{e}_y \quad (2.90)$$

and in which the tangential or transverse part of the dyadic Green's function is considered:

$$\bar{\bar{G}}_A(\bar{r}/\bar{r}') = \begin{pmatrix} G_A^{xx}(\bar{r}/\bar{r}') & 0 \\ 0 & G_A^{yy}(\bar{r}/\bar{r}') \end{pmatrix} = G_A^{xx}(\bar{r}/\bar{r}')\begin{pmatrix} 1 & 0 \\ 0 & 1 \end{pmatrix} \quad (2.91)$$

The subscript i, indicating in which region of the layered medium the

electric field is evaluated, has been dropped in the above expression because the fields are considered on the surfaces of both patches, which lie on the top and bottom boundary of the top dielectric layer: region 1. Subsequently, the only functions f appearing in the Green's functions (2.61) and (2.63) which are of interest are those for region 1b with the limit $z' \rightarrow h_1$ (surface current $\bar{J}_{s1}$) and those for region 1a with limit $z' \rightarrow 0$ (surface current $\bar{J}_{s2}$).

Equation (2.89) is the desired mixed potential electric field integral-equation which, ideally, has to be satisfied everywhere on the surfaces of the patches S_1 and S_2. Finding a solution for the surface currents which meets this requirement is, in general, not possible. One can therefore try and obtain an approximate solution for the above integral-equation by using a method of moments. The essence of the method of moments is that the integral-equation is transformed into a matrix-equation which can easily be solved [18]. The first step of the method of moments is rather straightforward and proceeds by first expanding the unknown currents and associated charges into a number of known basis- or expansion-functions, according to:

$$\bar{J}_{sj}(\bar{r}) = \sum_{i=1}^{N_j} \alpha_{ij}\, \bar{f}_{ij}(\bar{r}) \qquad j=1,2 \tag{2.92}$$

and

$$\rho_{sj}(\bar{r}) = \sum_{i=1}^{N_j} \alpha_{ij} h_{ij}(\bar{r}) \quad , \quad h_{ij}(\bar{r}) = -\frac{1}{j\omega} \nabla_t \cdot \bar{f}_{ij}(\bar{r}) \qquad j=1,2 \tag{2.93}$$

Because of the simple geometry of the patches, basis-functions $\bar{f}_{ij}$ and h_{ij} are chosen which are defined over the entire patch, this type of basis-function commonly being referred to as entire-domain basis-functions. This in contrast to the so-called subdomain basis functions defined over segments of the patch and used for more complicated patch shapes. It will be shown at the end of this section that for rectangular patches a convenient choice of basis-functions can be made, which will require only a small number N_j to expand the current $\bar{J}_{sj}$ on patch S_j.

Substitution of (2.92) and (2.93) in (2.89) yields:

$$- \frac{I}{j\omega} \nabla_t G_v^v(\bar{r}/\bar{r}_c) = \sum_{j=1}^{2} \sum_{i=1}^{N_j} \alpha_{ij} \left\{ j\omega \int_{S_j} \bar{\bar{G}}_A(\bar{r}/\bar{r}_j) \cdot \bar{f}_{ij}(\bar{r}_j) ds_j + \right.$$

$$\left. \nabla_t \int_{S_j} G_v^H(\bar{r}/\bar{r}_j) h_{ij}(\bar{r}_j) ds_j + Z_s \bar{f}_{ij}(\bar{r}) \right\} \qquad (2.94)$$

$$\bar{r} \in S_1 \cup S_2$$

Eqn. (2.94) still has to be satisfied at all points on both patches, because it represents a boundary condition at the surface of these patches. It is, however, still very difficult, even for the reduced integral-equation (2.94), to find a solution so that the integral-equation holds everywhere on the patches. Therefore a sort of "testing" procedure is applied to (2.94). The most simple procedure is that, in which the integral-equation is exactly satisfied at a set of discrete points on the patches, and consists of testing (2.94) by taking a product of both sides with a set of spatial Dirac-delta functions at these points and then integrate over the corresponding patch. This procedure, however, is, besides its slow convergence, not very well suited here because of the coaxial feed model used (delta-excitation), which presents itself as a singularity on the lower interface [15]. A more appropriate procedure in this case is to use the so-called Galerkin-method, in which the basis- or expansion-functions are also used as test-functions. This testing procedure involves first taking the inner-product of both sides of (2.94), which are vectors in the transverse plane, with the test-functions $\bar{f}_{ki}$, i=1,2 and k=1,$\cdots$,N_i, and then to integrate the resulting scalar quantity over the surface S_i. This leads to the following set of equations:

$$- \frac{I}{j\omega} \int_{S_i} \bar{f}_{ki}(\bar{r}_i) \cdot \nabla_t G_v^v(\bar{r}_i/\bar{r}_c)\, ds_i =$$

$$\sum_{j=1}^{2} \sum_{i=1}^{N_j} \alpha_{ij} \left\{ j\omega \int_{S_i} \bar{f}_{ki}(\bar{r}_i) \cdot \left[\int_{S_j} \bar{\bar{G}}_A(\bar{r}_i/\bar{r}_j) \cdot \bar{f}_{ij}(\bar{r}_j)\, ds_j \right] ds_i + \right. \qquad (2.95)$$

$$\left. \int_{S_i} \bar{f}_{ki}(\bar{r}_i) \cdot \left[\nabla_t \int_{S_j} G_v^H(\bar{r}_i/\bar{r}_j) h_{ij}(\bar{r}_j) ds_j \right] ds_i + Z_s \int_{S_i} \bar{f}_{ki}(\bar{r}_i) \cdot \bar{f}_{ij}(\bar{r}_i)\, ds_i \right\}$$

$$i = 1,2 \quad ; \quad k = 1,\cdots,N_i$$

in which the tangential part of the differential operator ∇ acts on the coordinates $\bar{r}_i$. The integral on the right-hand-side of (2.95) can be simplified as follows, using the two-dimensional Gauss-theorem, the fact that

the currents perpendicular to the edges of the patch vanish on these edges and Eqn. (2.93):

$$\int_{S_i} \bar{f}_{ki} \cdot \nabla_t G_v^v \, ds_i = \int_{S_i} \nabla_t \cdot [G_v^v \bar{f}_{ki}] ds_i - \int_{S_i} G_v^v \nabla_t \cdot \bar{f}_{ki} ds_i$$

$$= \oint_{L_i} [G_v^v \bar{f}_{ki}] \cdot \hat{n}_i dl_i + j\omega \int_{S_i} G_v^v h_{ki} ds_i = j\omega \int_{S_i} G_v^v h_{ki} ds_i \qquad (2.96)$$

Using the same approach, the second integral on the right-hand-side can rewritten as:

$$\int_{S_i} \bar{f}_{ki} \cdot \left[\nabla_t \int_{S_j} G_v^H h_{lj} ds_j \right] ds_i$$

$$= \int_{S_i} \nabla_t \cdot \left[\bar{f}_{ki} \int_{S_j} G_v^H h_{lj} ds_j \right] ds_i - \int_{S_i} \nabla_t \cdot \bar{f}_{ki} \left[\int_{S_j} G_v^H h_{lj} ds_j \right] ds_i$$

$$= \oint_{L_i} \left[\int_{S_j} G_v^H h_{lj} ds_j \, \bar{f}_{ki} \right] \cdot \hat{n}_i dl_i + j\omega \int_{S_i} h_{ki} \left[\int_{S_j} G_v^H h_{lj} ds_j \right] ds_i$$

$$= j\omega \int_{S_i} \int_{S_j} h_{ki} G_v^H h_{lj} ds_i ds_j \qquad (2.97)$$

In (2.96) and (2.97) L_i is the contour of patch S_i and $\hat{n}_i$ is the unit vector, normal to L_i, and lying in the plane S_i.

We thus have obtained a set of $N_1 + N_2$ linear equations, Eqns. (2.95), in $N_1 + N_2$ unknowns; the expansion mode coefficients α_{lj}. They can be solved from the matrix-equation

$$\bar{\bar{C}} \cdot \bar{\alpha} = \bar{b} \qquad (2.98)$$

which, written out, reads

$$\begin{pmatrix} C_{11,11} & \cdots & C_{11,N_1 1} & C_{11,12} & \cdots & C_{11,N_2 2} \\ \vdots & & \vdots & \vdots & & \vdots \\ C_{N_1 1,11} & \cdots & C_{N_1 1,N_1 1} & C_{N_1 1,12} & \cdots & C_{N_1 1,N_2 2} \\ C_{12,11} & \cdots & C_{12,N_1 1} & C_{12,12} & \cdots & C_{12,N_2 2} \\ \vdots & & \vdots & \vdots & & \vdots \\ C_{N_2 2,11} & \cdots & C_{N_2 2,N_1 1} & C_{N_2 2,12} & \cdots & C_{N_2 2,N_2 2} \end{pmatrix} \cdot \begin{pmatrix} \alpha_{11} \\ \vdots \\ \alpha_{N_1 1} \\ \alpha_{12} \\ \vdots \\ \alpha_{N_2 2} \end{pmatrix} = \begin{pmatrix} b_{11} \\ \vdots \\ b_{N_1 1} \\ b_{12} \\ \vdots \\ b_{N_2 2} \end{pmatrix} \qquad (2.99)$$

The elements of the excitation-vector are given by

$$b_{ki} = - I \int_{S_i} G_v^v(\bar{r}_i/\bar{r}_c) h_{ki}(\bar{r}_i) ds_i \qquad (2.100)$$

and the matrix elements by

$$\begin{aligned} C_{ki,lj} = {} & j\omega \int_{S_i}\int_{S_j} \bar{f}_{ki}(\bar{r}_i)\cdot\bar{\bar{G}}_A(\bar{r}_i/\bar{r}_j)\cdot\bar{f}_{lj}(\bar{r}_j) ds_j ds_i \\ & + j\omega \int_{S_i}\int_{S_j} h_{ki}(\bar{r}_i) G_v^H(\bar{r}_i/\bar{r}_j) h_{lj}(\bar{r}_j) ds_j ds_i \\ & + Z_s \int_{S_i} \bar{f}_{ki}(\bar{r}_i)\cdot\bar{f}_{lj}(\bar{r}_j) ds_i \end{aligned} \qquad (2.101)$$

The matrix elements constitute the modal interaction between the expansion mode k on patch i and expansion mode l on patch j. The last term in (2.101) can be identified as the ohmic loss due to two current expansion modes and this term is obviously zero for $i \neq j$, i.e., for currents on different patches.

An interesting, and quite useful, feature of the above matrix is its symmetry:

$$C_{ki,lj} = C_{lj,ki} \qquad \text{for all} \quad \begin{matrix} i=1,2 \ ; \ k=1,\cdots,N_i \\ j=1,2 \ ; \ l=1,\cdots,N_j \end{matrix} \qquad (2.102)$$

A fact which will considerably reduce the amount of computation time needed to fill the matrix. This symmetry is obvious for modes on the same patch, $i = j$, remembering that the radial dependence of the Green's functions is of the form $|\bar{\rho}_i - \bar{\rho}_j|$, which allows a simple interchange of source (j) and observation (i). For the matrixelements involving the interaction between modes of different patches, $i \neq j$, symmetry is not directly clear because source- and observation-coordinates are located on different z-planes. It is, however, fairly easy to show, by inspection of Eqns. (2.42)-(2.44), (2.53), (2.61) and (2.63), taking the appropriate limits for the source- and observation-planes, namely $z \to h_1$ and $z' \to 0$ in f_{x1a} and f_{v1a} and the limits $z \to 0$ and $z' \to h_1$ in f_{x1b} and f_{v1a}, that

$$\bar{\bar{G}}_A(\bar{r}_i/\bar{r}_j) = \bar{\bar{G}}_A(\bar{\rho}_i, z=z_i/\bar{\rho}_j, z'=z_j) = \bar{\bar{G}}_A(|\bar{\rho}_i - \bar{\rho}_j|, z=z_i, z'=z_j)$$
$$= \bar{\bar{G}}_A(|\bar{\rho}_j - \bar{\rho}_i|, z=z_j, z'=z_i) = \bar{\bar{G}}_A(\bar{\rho}_j, z=z_j/\bar{\rho}_i, z'=z_i) = \bar{\bar{G}}_A(\bar{r}_j/\bar{r}_i) \qquad (2.103)$$

and, along similar lines, that

$$G_v^H(\bar{r}_i/\bar{r}_j) = G_v^H(\bar{r}_j/\bar{r}_i) \qquad (2.104)$$

Both (2.103) and (2.104) are, in fact, a case of reciprocity applied to two points on different levels within the layered medium.

A quantity of interest which can be obtained from the "method-of-moments" matrix $\bar{\bar{C}}$, without any knowledge of the excitation-vector $\bar{b}$, is the resonant frequency of the microstrip antenna. Because a microstrip antenna is basically a resonant structure, independent of the form of excitation, its resonant behaviour only depends on the geometry and dielectric properties of the substrate layers and on the shape and size of the microstrip patches; characteristics which are all incorporated in the matrix $\bar{\bar{C}}$. The resonant frequencies of the structure correspond to roots of the determinant of $\bar{\bar{C}}$, which, in general, is complex [12]. Because we are not so much interested in the complex resonant frequency but primarily in the real part of the resonant frequency, the matrix can be evaluated for real frequencies and the modulus of the determinant subsequently investigated for minima, which occur at the real resonant frequencies, close to the complex resonant frequency where the determinant vanishes completely.

A final point of discussion in this section is the choice of the current expansion functions, appearing in (2.92). The convergence of the method of moments for obtaining the solution of the integral-equation depends largely upon the choice of basis-functions. Choosing basis-functions which are already close to the actual solution greatly reduces the number of current modes needed for expressing the patch currents in terms of a series of these modes. An appropriate choice is the use of sinusoidal basis-functions, corresponding to the eigen- or resonant-modes associated with rectangular patches [3], derived from the microstrip cavity model [19]:

$$\bar{f}_{ki}(x_i,y_i) = \hat{e}_x \sin\left[\frac{m_x^{ki}\pi}{a_i}(x_i - x_{oi})\right] \cos\left[\frac{n_x^{ki}\pi}{b_i}(y_i - y_{oi})\right]$$
$$+ \hat{e}_y \cos\left[\frac{m_y^{ki}\pi}{a_i}(x_i - x_{oi})\right] \sin\left[\frac{n_y^{ki}\pi}{b_i}(y_i - y_{oi})\right] \qquad (2.105)$$

from which the associated charge expansion functions can be found from (2.93)

$$h_{ki}(x_i,y_i) = -\frac{1}{j\omega}\left\{\frac{m_x^{ki}\pi}{a_i}\cos\left[\frac{m_x^{ki}\pi}{a_i}(x_i - x_{oi})\right]\cos\left[\frac{n_x^{ki}\pi}{b_i}(y_i - y_{oi})\right]\right.$$
$$\left. + \frac{n_y^{ki}\pi}{b_i}\cos\left[\frac{m_y^{ki}\pi}{a_i}(x_i - x_{oi})\right]\cos\left[\frac{n_y^{ki}\pi}{b_i}(y_i - y_{oi})\right]\right\} \qquad (2.106)$$

with a_i and b_i the dimension of patch i in the x- and y-direction, respectively, and x_{oi} and y_{oi} the offset of patch i with respect to the local coordinate system. Although the lower patch is assumed to be fixed to coordinate system ($x_{o2} = y_{o2} = 0$), the offsets are introduced to allow the upper patch to be shifted with respect to the lower patch in the x- and y-direction (Fig. 2.6).

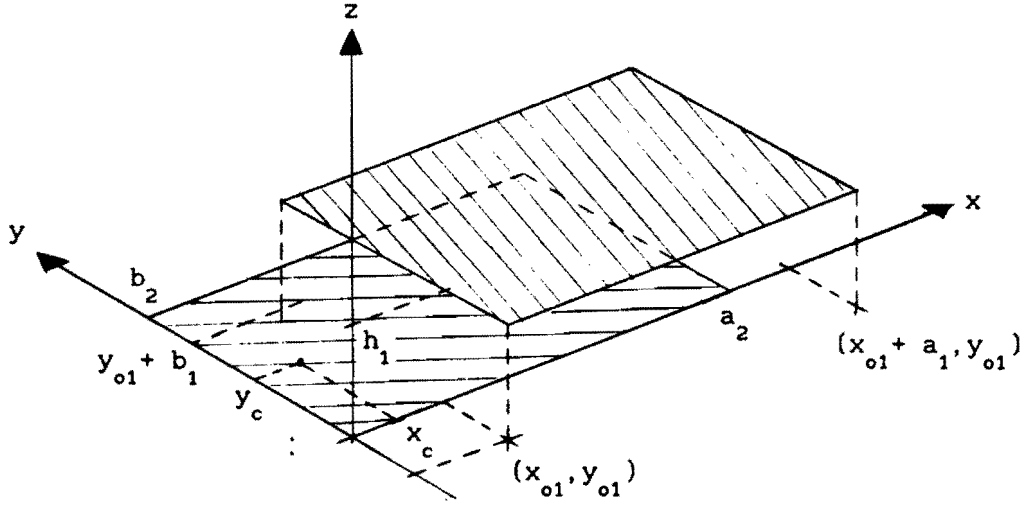

Fig. 2.6 Rectangular patches and coaxial-feed with respect to local coordinate system

Usually the x- and y-component of the patch currents are considered as

separate quantities, but the general current expansion mode (2.105), which includes a single x- and y-directed current mode as special cases, is introduced here because the solution of the integral-equation allows a more general and straightforward derivation if only one general expansion mode is used instead of two separate x- and y-directed expansion modes

If the frequency of operation is close to the resonant frequency of a particular resonant mode, whose spatial variation is determined by the integers m_x^{ki}, n_x^{ki}, m_y^{ki} and n_y^{ki}, the actual surface current can be accurately described by (2.105) for that particular mode at or near resonance, largely independent of the excitation mechanism. So, the nature of a particular current mode, which resonates for a given frequency, is relatively insensitive to the actual position of the coaxial feed at resonance. The total patch current for a given microstrip- and feed-configuration is then the sum of the currents of each individual mode which is present. The number and type of current modes present, and the extent in which each of them is excited, will depend on the dimension of the patches relative to the frequency, the dielectric constants of the substrates and the position of the coaxial feed. It would therefore be recommendable to investigate beforehand which current modes might be appreciably excited for a given microstrip antenna configuration, in order to minimize the number of current modes for expanding the patch currents in the method-of-moments solution of the integral-equation. This then reduces the order of the matrix and therefore the computation time.

For a single-layer/single-patch microstrip antenna the resonant frequencies of the resonant modes in, for instance, the x-direction of the patch can be roughly estimated as being those frequencies for which one-half wavelength in the dielectric substrate, $\lambda/(2\sqrt{\varepsilon_r})$, fits an integral number of times onto the dimension a of the patch [19]. The lowest order resonant mode then has a simple half-sinusoidal variation in the x-direction, and the variation in the orthogonal y-direction is usually assumed to be uniform. Such a simple current mode can be seen to be included in the general form Eqn. (2.105) for a proper choice of the integers m_x^{ki}, n_x^{ki}, m_y^{ki} and n_y^{ki}. For current modes in the y-direction the same can be said relative to the dimension b in that direction. If now $a \neq b$ and $\lambda/(2\sqrt{\varepsilon_r}) \approx a$ then the resonant mode in the x-direction will be predominant and the non-resonant mode in the y-direction

is not or only weakly excited depending on the ratio a/b, because the latter has a different resonant frequency. For square patches, a = b, both lowest order orthogonal current modes have the same resonant frequency and can thus both be excited, the degree of excitation in this case now strongly depending on the position of the coaxial feed. It is known in these cases that for coaxial probes located halfway between two parallel edges (center-fed) and at an arbitrary distance from one of the other two perpendicular edges, only one of the two equal current modes will be strongly excited, namely the one in the direction of the parallel edges, and the other orthogonal mode will be negligible. For off-center fed square patches the orthogonal mode can also be excited and must therefore be included in the calculations.

Even though this modal expansion treatment for the patch currents is found from the cavity model for a single-layer/single-patch microstrip antenna, it is thought that it can also be applied in our case to the upper patch, which is excited by electromagnetic coupling from the lower patch, and to the lower patch, which is directly driven by the coaxial probe, because the basic resonant nature of the structure does not depend upon the form of excitation as mentioned before. For making an educated guess regarding the current expansion modes needed to describe the patch current in a stacked microstrip antenna, which subsequently should be included in the method-of-moments solution, similar considerations as those given above for the single-patch microstrip antenna will also hold for two stacked patches. If the dimensions of the patches and the frequency are such that only the lowest order current modes are of interest, only one or two orthogonal modes per patch will be sufficient, depending on the ratio a_i/b_i and taking into account the position of the feed relative to the edges of the patches (center or off-center fed), the latter consideration also being valid for the upper patch, even though it is not directly connected to the coaxial feed.

2.7 Calculation of the input impedance

Once the patch currents have been found for a particular microstrip structure and feed arrangement, it is fairly straightforward to obtain the antenna input-impedance. First, consider the schematic drawing of the antenna, together with the coaxial feed and current source; figure 2.7.

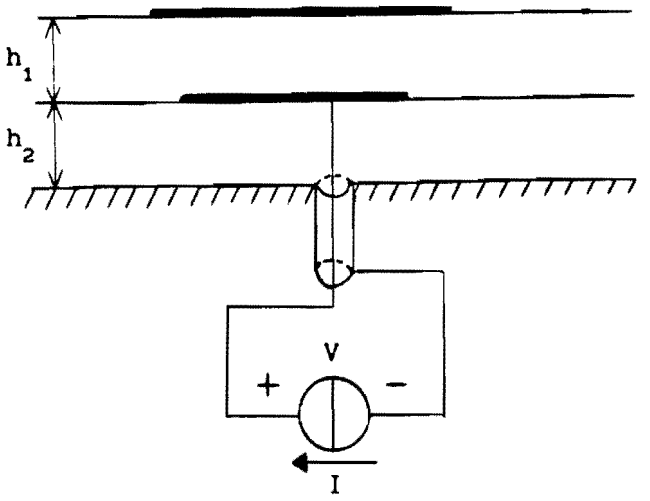

Fig. 2.7 Current and voltage for determining input-impedance

With the signs as indicated in the above figure, the input-impedance is defined as

$$Z_{in} = \frac{V}{I} \tag{2.107}$$

with I the impressed excitation current and V the voltage across the current source. This voltage is approximately equal to the potential difference between the lower microstrip patch and the groundplane at the position of the inner conductor of the coaxial feed, which can be expressed in terms of the electric fields at the coax location as follows [12]:

$$V = -\int_{-h_2}^{0} \left(\bar{E}^r(\bar{\rho}_c, z) + \bar{E}^e(\bar{\rho}_c, z) \right) \cdot \hat{e}_z \, dz \tag{2.108}$$

The first field component is the field radiated by the currents on the microstrip patches, while the second is due to the excitation current. The latter, which is commonly referred to as the self-term, because it accounts for the fields produced by the coaxial probe on itself, is usually neglected at or near resonance [12]. The input-impedance can thus be found from

$$Z_{in} = -\frac{1}{I}\int_{-h_2}^{0} E_z^r(\bar{\rho}_c, z)\, dz \qquad (2.109)$$

Evaluating the input-impedance according to (2.109) is quite involved because, besides the appearance of the line integral along z, the field component E_z^r is itself expressed in terms of superposition integrals of the patch currents and charges, weighted by the appropriate Green's functions, Eqn. (2.88). It is however possible to simplify (2.109) by invoking the Lorentz-reciprocity theorem to the situation of the field $\bar{E}^r$ due to the distribution of surface currents $\bar{J}_s$ flowing on S on the one hand, and the excitation field $\bar{E}^e$ due to the excitation current distribution $\bar{J}_c = \hat{e}_z I\delta(x-x_c)\delta(y-y_c)$ on the other hand. Using an approach similar to the derivation in section 2.5, application of the Lorentz-theorem now yields:

$$I\int_{-h_2}^{0} E_z^r(\bar{\rho}_c, z)\, dz = \int_S \bar{E}^e(\bar{r})\cdot\bar{J}_s(\bar{r})\, ds \qquad (2.110)$$

with

$$\bar{J}_s(\bar{r}) = \bar{J}_{s1}(\bar{r}) + \bar{J}_{s2}(\bar{r}) \quad ; \quad S = S_1 \cup S_2 \qquad (2.111)$$

for a two-layer microstrip. The input impedance can now be written as

$$Z_{in} = -\frac{1}{I^2}\int_S \bar{E}^e(\bar{r})\cdot\bar{J}_s(\bar{r})\, ds \qquad (2.112)$$

This expression can be further simplified by noting that the field in (2.112) is the excitation field due to the vertical current probe, tangential to the patches, and is therefore given by (2.87). Substitution of (2.87) in (2.112) and using a derivation analogous to that of Eqn. (2.68) gives

$$Z_{in} = -\frac{1}{I^2}\int_S \bar{E}^e_{tang}(\bar{r})\cdot\bar{J}_s(\bar{r})\,ds = \frac{1}{j\omega I}\int_S \nabla_t G_v^v(\bar{r}/\bar{r}_c)\cdot\bar{J}_s(\bar{r})\,ds$$
$$= \frac{1}{j\omega I}\int_S \nabla_t\cdot(G_v^v(\bar{r}/\bar{r}_c)\bar{J}_s(\bar{r}))\,ds - \frac{1}{j\omega I}\int_S G_v^v(\bar{r}/\bar{r}_c)\nabla_t\cdot\bar{J}_s(\bar{r})\,ds$$
$$= \frac{1}{j\omega I}\oint_L (G_v^v(\bar{r}/\bar{r}_c)\cdot\bar{J}_s(\bar{r}))\cdot\hat{n}\,dl + \frac{1}{I}\int_S G_v^v(\bar{r}/\bar{r}_c)\rho_s(\bar{r})\,ds$$
$$= \frac{1}{I}\int_S G_v^v(\bar{r}/\bar{r}_c)\rho_s(\bar{r})\,ds \qquad (2.113)$$

Substituting the "method-of-moments" solution for the charge distribution (2.93) into (2.113), for a two-layer microstrip, and using the expression for the elements of the excitation vector (2.100) then gives:

$$Z_{in} = \frac{1}{I}\sum_{j=1}^{2}\int_{S_j} G_v^v(\bar{r}_j/\bar{r}_c)\rho_{sj}(\bar{r}_j)ds_j = \frac{1}{I}\sum_{j=1}^{2}\sum_{l=1}^{N_j}\alpha_{lj}\int_{S_j} G_v^v(\bar{r}_j/\bar{r}_c)h_{lj}(\bar{r}_j)ds_j$$
$$= -\frac{1}{I^2}\sum_{j=1}^{2}\sum_{l=1}^{N_j}\alpha_{lj}b_{lj} \qquad (2.114)$$

which is a particularly simple expression for the input-impedance, since both α_{lj} and b_{lj} are known once the matrix-equation (2.98) has been solved.

2.8 Surface waves and surface wave poles

In the theory presented in the previous sections it is assumed that the Green's functions are available for use in solving the integral-equation with the method of moments. However, these Green's functions are themselves given as integrals, which first have to be investigated in order for them to be calculated and used in the Green's function treatment of the microstrip radiation problem. Especially because those integrals cannot be found in closed form due to the complex integrands, their behaviour is of importance if they are to be evaluated numerically. This section deals with the surface waves present in the layered medium and how they appear within the Green's functions. In the next section the actual integration in the complex plane is then treated for evaluating these functions.

Surface waves are a wave phenomenon which can be present in a microstrip structure, because these structures have an inhomogeneous nature. Roughly speaking they can be identified as waves, propagating along the boundary of two different media and exponentially decaying or evanescent with distance normal to this boundary. To investigate these in our case, we consider the incidence of two types of waves from the air region upon the microstrip structure at an arbitrary angle with respect to the z-axis. Since all waves can be decomposed into a TM- and a TE-part, we let these two types be a transverse magnetic (TM) and a transverse electric (TE) wave with respect to to the z-axis.

It can be shown that for two dielectric layers, backed by a perfectly conducting groundplane, the factors D_{TM} and D_{TE}, appearing in the Green's functions, Eqns. (2.46) and (2.41), correspond to the denominators of the reflection coefficients of the TM- and TE-wave, respectively,

$$R_{TM} \propto \frac{1}{D_{TM}}$$
$$R_{TE} \propto \frac{1}{D_{TE}} \qquad (2.115)$$

which are the ratios of the amplitude of the reflected wave to that of the incident wave [20]. To find any waves which are guided by the microstrip structure and can exist without the presence of any form of excitation, the so-called eigenmodes of the structure, the incident wave is removed, i.e., the amplitude of the incident wave approaches zero, which, in our formulation, then corresponds to an infinite reflection factor. The guidance conditions for these eigenmodes can thus be found by investigating the occurrence of infinite reflection coefficients for TM- and TE-waves [21], which is the case if :

$$D_{TM} = 0 \qquad (2.116)$$

or

$$D_{TE} = 0 \qquad (2.117)$$

Expressions (2.116) and (2.117) can thus be identified as the characteristic

equations for either a TM- or a TE-eigenmode, guided by the structure, and they yield the propagation constants for these modes. Since any zeros of D_{TM} and D_{TE} appear as poles in the integrands of the integrals defining the Green's functions, which are thus directly related to the existence of any TM- or TE-eigenmodes, it is important to examine the characteristic equations (2.116) and (2.117) in order to determine, if possible, the number and location of its roots.

Written out, (2.116) and (2.117) read

$$\cosh u_1 h_1 \left[\frac{\varepsilon_2}{\varepsilon_0} u_0 + u_2 \tanh u_2 h_2 \right] + \sinh u_1 h_1 \left[\frac{\varepsilon_2}{\varepsilon_1} u_1 + \frac{\varepsilon_1 u_0}{\varepsilon_0 u_1} u_2 \tanh u_2 h_2 \right] = 0 \qquad (2.118)$$

for TM-modes, and

$$\cosh u_1 h_1 \left[u_0 + u_2 \coth u_2 h_2 \right] + \sinh u_1 h_1 \left[u_1 + \frac{u_0 u_2}{u_1} \coth u_2 h_2 \right] = 0 \qquad (2.119)$$

for TE-modes, with

$$\begin{aligned} u_0 &= (k_\rho^2 - k_0^2)^{1/2} \quad ; \quad k_0^2 = \omega^2 \mu_0 \varepsilon_0 \\ u_1 &= (k_\rho^2 - k_1^2)^{1/2} \quad ; \quad k_1^2 = k_0^2 \varepsilon'_{r1} (1 - j\tan\delta_1) \\ u_2 &= (k_\rho^2 - k_2^2)^{1/2} \quad ; \quad k_2^2 = k_0^2 \varepsilon'_{r2} (1 - j\tan\delta_2) \end{aligned} \qquad (2.120)$$

Two problems arise in finding the solutions of the equations (2.118) and (2.119). First, these equations are transcendental and no analytical solution can be found. Secondly, because of the presence of dielectric losses in (2.120) the solutions of both (2.118) and (2.119) are, in general, complex. One therefore has to resort to numerical techniques for solving these equations. It would, however, be convenient if something could be said about the number of TM- and/or TE-modes present for a given microstrip structure, in order to correctly take them into account when evaluating the integrals which define the Green's functions.

This can be done by attempting to find the conditions under which roots start to appear in the above characteristic equations, or, in other words, possible TM- or TE-modes start to appear in the microstrip structure. Due to dielectric losses this is, again, quite complicated, but because these losses are usually small ($\tan\delta \approx 0.0001\text{-}0.01$) we first examine the case without losses and investigate the effect of these losses on the roots of (2.118) and (2.119) later.

In the lossless case the roots of (2.118) and (2.119), if any, lie on the real axis λ of the complex k_ρ-(=λ+jν)-plane and they lie within the interval $[k_0, \max(k_1,k_2)] = [k_0, k_0\sqrt{\varepsilon'_{rmax}}\,]$, [22]. Of course, roots also lie on the negative real axis due to the symmetry with respect to the origin in the functions (2.120), but here only roots on the positive real axis are considered. A root in this interval then corresponds to the radial component of the wavevector for a particular TM- or TE-eigenmode and it is easy to see from (2.38) that the axial component of the wavevector in the air region is purely imaginary. The z-dependence in this region is of the form $\exp[-jk_{z0}(z-h_1)]$, so that with the proper root for $k_{z0} = (k_0^2 - \lambda^2)^{1/2}$ the wave is evanescent in the z-direction. Together with the propagation constant in the radial direction, the waves arising from the characteristic equations (2.116) and (2.117) can thus be classified as TM- and TE-surface-wave modes.

Several of these TM- or TE-surface-wave modes can be excited in the microstrip structure, depending on the configuration, i.e., the dielectric constants and the thicknesses of the substrate layers and on the frequency. Denoting the radial propagation constant as β_{TMn} for the TM- and β_{TEn} for the TE-surface-wave modes, then all TM_n- or TE_n-surface mode turn on when their radial propagation constants equal k_0: $\beta_{TMn} = k_0$ and $\beta_{TEn} = k_0$ for all n [22] [23]. It is now possible to determine the cut-off conditions for each mode by substituting the cut-off wavenumbers $\beta_{TMn} = k_0$ and $\beta_{TEn} = k_0$ into the equations (2.118) and (2.119) with

$$
\begin{aligned}
u_0 &= (\lambda^2 - k_0^2)^{1/2} \quad ; \quad k_0^2 = \omega^2\mu_0\varepsilon_0 \\
u_1 &= j(k_1^2 - \lambda^2)^{1/2} \quad ; \quad k_1^2 = \omega^2\mu_0\varepsilon_1 = k_0^2\varepsilon'_{r1} \\
u_2 &= j(k_2^2 - \lambda^2)^{1/2} \quad ; \quad k_2^2 = \omega^2\mu_0\varepsilon_2 = k_0^2\varepsilon'_{r2}
\end{aligned}
\qquad (2.121)
$$

This yields

$$\cot\,[h_2(k_2^2 - k_0^2)^{1/2}] = \frac{(k_1^2 - k_0^2)^{1/2}}{(k_2^2 - k_0^2)^{1/2}}\ \tan\,[h_1(k_1^2 - k_0^2)^{1/2}] \qquad (2.122)$$

for the TE-surface modes, and

$$-\tan\,[h_2(k_2^2 - k_0^2)^{1/2}] = \frac{\varepsilon_2}{\varepsilon_1}\,\frac{(k_1^2 - k_0^2)^{1/2}}{(k_2^2 - k_0^2)^{1/2}}\ \tan\,[h_1(k_1^2 - k_0^2)^{1/2}] \qquad (2.123)$$

for the TM-surface modes. These equations have multiple solutions, each solution corresponding to a configuration of parameters f, h_1, h_2, ε'_{r1} and ε'_{r2} for which a particular surface-wave mode can only just be excited with cut-off wavenumbers $\beta_{TMn} = k_0$ and $\beta_{TEn} = k_0$. This can be made more clear using a graphical representation of the cut-off conditions (2.122) and (2.123). Introducing the variable

$$x = \frac{2\pi h_1}{\lambda_0}\ (\varepsilon'_{r1} - 1)^{1/2} \qquad (2.124)$$

with λ_0 the wavelength in vacuum, and the constant

$$C = \frac{h_2}{h_1}\,\frac{(\varepsilon'_{r2} - 1)^{1/2}}{(\varepsilon'_{r1} - 1)^{1/2}} \qquad (2.125)$$

they can be written as

$$\frac{h_1}{h_2}\ C\ \cot\,(Cx) = \tan\,(x) \qquad (2.126)$$

and

$$-\frac{\varepsilon'_{r1}}{\varepsilon'_{r2}}\,\frac{h_1}{h_2}\ C\ \tan\,(Cx) = \tan\,(x) \qquad (2.127)$$

for the TE- and TM-modes, respectively. For the TE-modes both sides of (2.126)are depicted in figure 2.8 for an arbitrary value of the constant C.

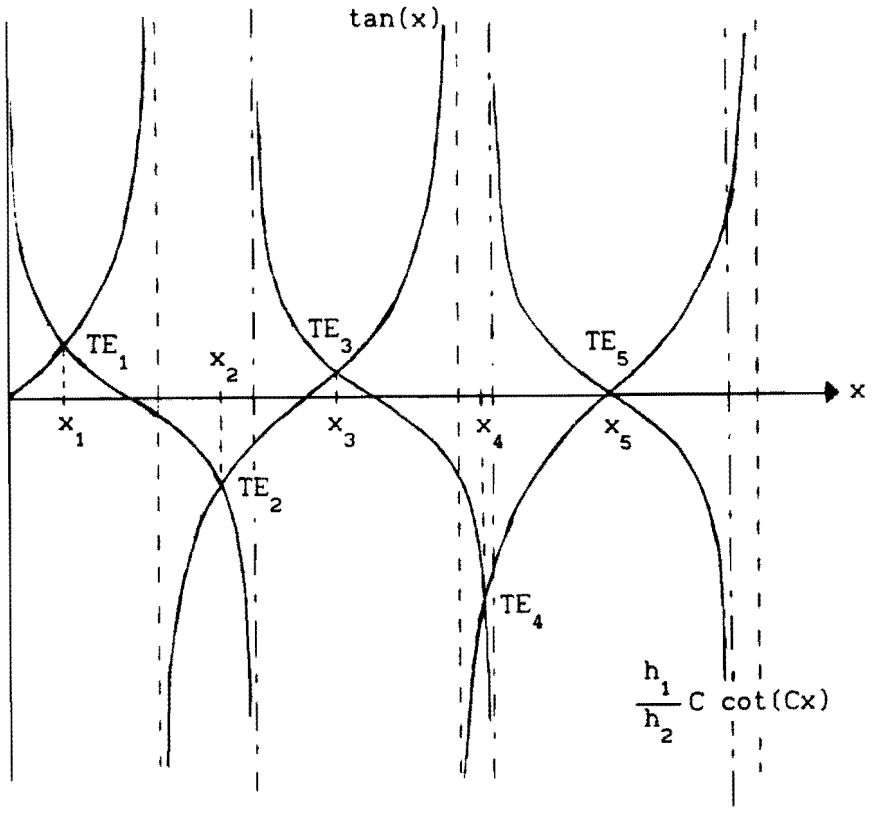

Fig. 2.8 Graphical representation of the TE-surface-wave mode cut-off conditions

From this figure it can be seen that for a fixed C, the variable x determines whether a given TE_n-mode is below or above cut-off. If, for instance, $x < x_1$, with x_1 being the first root of (2.126) corresponding to the cut-off condition of the first TE-mode, all TE-surface-wave modes are below cut-off and can therefore not exist within the micro strip structure. If $x = x_1$, the TE_1-mode is exactly at cut-off, corresponding to a propagation constant $\beta_{TEn} = k_0$ and all other TE-modes are still below their cut-off condition. For x between x_1 and x_2 only the TE_1-mode can exist with propagation constant somewhere within the interval $k_0 \leq \beta_{TE1} \leq \max(k_1, k_2)$; the exact location now being determined directly from (2.116) using numerical methods. Going further along the x-axis; for $x = x_2$ the TE_1-mode can exist and the TE_2-mode is just at cut-off with $\beta_{TE2} = k_0$, and so on and so forth.

Plotting both sides of the cut-off condition for the TM-surface-wave modes,

Eqn. 2.127, show the conditions for which the various TM-modes are at cut-off as the intersection of the two curves, figure 2.9.

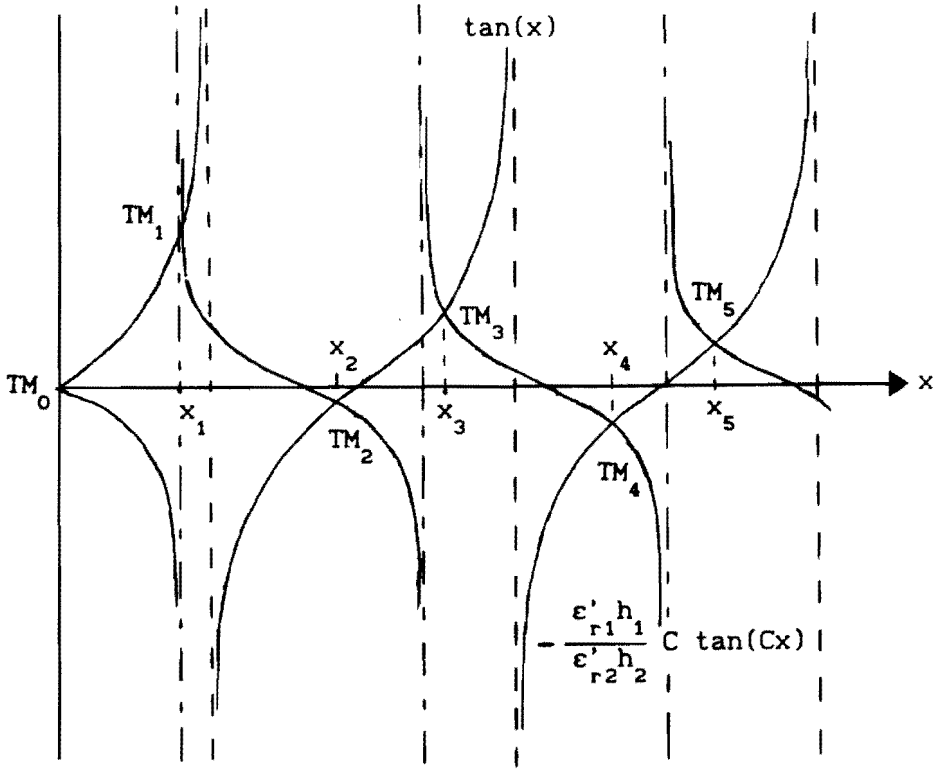

Fig. 2.9 Graphical representation of the TM-surface-wave mode cut-off conditions

The same explanation as that given above for the TE-modes can be given here as to the interpretation of this figure with respect to the cut-off and possible existence of TM-surface-wave modes for a given microstrip structure, the configuration being incorporated in the parameters C and x. From this figure it is directly clear that, no matter what substrate thicknesses, permittivities or frequency of operation are used, there is always at least one TM-mode at or above cut-off. This mode shall be denoted as the dominant TM_0-surface-wave mode, and it has a zero cut-off frequency for a given layered medium. Its propagating characteristics are determined from the propagation constant β_{TE0}, which can be found as the zero of (2.118), and for the lossless case it lies in the interval $k_0 \leq \beta_{TM0} \leq \max(k_1, k_2)$.

It can now be stated that there is always the TM_0-mode present and in the Green's function formulation it appears as a surface-wave pole in the integrands of these functions. Other modes, both TM and TE, could also be present, but their possible existence depends on the microstrip parameters h_1, h_2, ε'_{r1} and ε'_{r2} and on the frequency f (λ_0). It is of interest to investigate the conditions under which the TM_0-mode is the only one that can exist and all other modes are below cut-off; especially in view of the calculation of the Green's functions and the numerical search for the root of (2.118). After the TM_0-mode, the first surface-wave mode that can be excited is the TE_1-mode and the condition for the presence of at least and at most one surface-wave mode can thus be formulated as: $x < x_1$ (Fig. 2.8). For given microstrip parameters, x_1 is the first solution of (2.126) and from (2.124) the maximum usable frequency, corresponding to the cut-off frequency of the TE_1-mode, for which this condition is met can be found. As a practical example, it can be easily verified that for $2 \leq \varepsilon'_r \leq 10.5$, $h_{1,2} \leq 3$ mm. and $f < 2$ GHz. this condition is always satisfied, this range of parameters roughly corresponding to that used in the microstrip phased array design [1].

In the evaluation of the Green's functions in the next section, it will be assumed that the condition stated is always met and that therefore D_{TE} has no zeros at all and D_{TM} has exactly one zero, which, as is the case for a single-layer microstrip structure, is a simple or first order zero.

If dielectric losses are now introduced, the surface-wave poles no longer lie on the real axis. They instead become complex, having a small negative imaginary part, depending on the amount of loss present [13]. They thus lie just below the real axis in the fourth quadrant of the complex k_ρ-plane for zeros with positive real part and just above the real axis in the second quadrant for those with negative real part. Because the deviation from the real axis is small, the cut-off frequency of the first TE-surface-wave mode, which equals the maximum frequency for which exactly one surface mode can be present, can still be derived accurately enough from the lossless case, as stated above.

2.9 Evaluation of the Sommerfeld-type integrals

The Green's functions which have been derived for the microstrip structure, are given as integrals of functions in the complex plane of the spectral variable k_ρ, and they have a form similar to the so-called Sommerfeld integrals [10]. In our case they have the general form

$$\int_C H_n^{(2)}(k_\rho \xi)\, k_\rho^{n+1}\, f(k_\rho, z, z')\, dk_\rho \qquad (2.128)$$

A proper integration path C must now be chosen in order to correctly evaluate these integrals. This choice is particularly influenced by the presence of the two-valued complex functions u_0, u_1 and u_2, Eqn. (2.38), in the functions f, and the restrictions imposed on the axial component of the wavevector k_{z0} by the radiation condition: Eqn. (2.39). Because of these double-valued functions it is essential for the integrals to represent a proper field solution that integrands are single-valued and uniquely determined along the integration path C, with the correct values of u_0, u_1 and u_2 chosen.

To investigate this we shall consider, instead of the quantities u_0, u_1 and u_2, the actual axial wavenumbers k_{z0}, k_{z1} and k_{z2} as a function of the radial wavenumber k_ρ, given by

$$k_{zi} = (k_i^2 - k_\rho^2)^{1/2} \qquad (2.129)$$

The value of this complex root for a given k_ρ depends on the argument of the quantity between parentheses in (2.129), resulting in two different values k_{zi}, differing only in sign, for two mathematically equivalent values $k_i^2-k_\rho^2$, the latter differing an amount of 2π with respect to their argument.

As shown in the Appendix, it is possible for the mapping $k_\rho \rightarrow k_z$ of the form (2.129) to define two separate sheets or branches for the complex k_ρ-plane, such that the mapping of these two sheets onto the entire complex k_{zi}-plane is now one-to-one, and (2.129) becomes single-valued. For these two sheets the argument of a point k_ρ on one of them then differs 2π with that of the same point on the other sheet. The two sheets together are known as a Riemann-surface and the separation between them are indicated by so-called branch cuts, which originate from the branch points. If, for instance, an

arbitrary curve is located on one of the sheets of the k_ρ-plane and this curve crosses a branch cut then this can be seen as the curve moving from one sheet of the k_ρ-plane to the other.

For a complex function, which is evaluated along this curve, passing from one sheet to another means that the function is possibly no longer single-valued or uniquely determined on this curve. As a safeguard against this, one can impose the requirement that a curve along which a function is evaluated, may not cross any of the branch cuts.

Returning to the Sommerfeld-integrals, it can now be stated that the integration path C must lie entirely on either one of the two sheets of the k_ρ-plane, defined by the functions (2.129), for a proper evaluation of these integrals. The choice of the proper sheet is determined by the radiation condition, Eqn. (2.39). From this condition it follows that that sheet of the k_ρ-plane must be chosen which maps onto the lower half of the k_{z0}-plane; $\mathrm{Im}(k_{z0}) < 0$. The layout of the k_ρ-plane can be inferred from the Appendix and is depicted in figure 2.10.

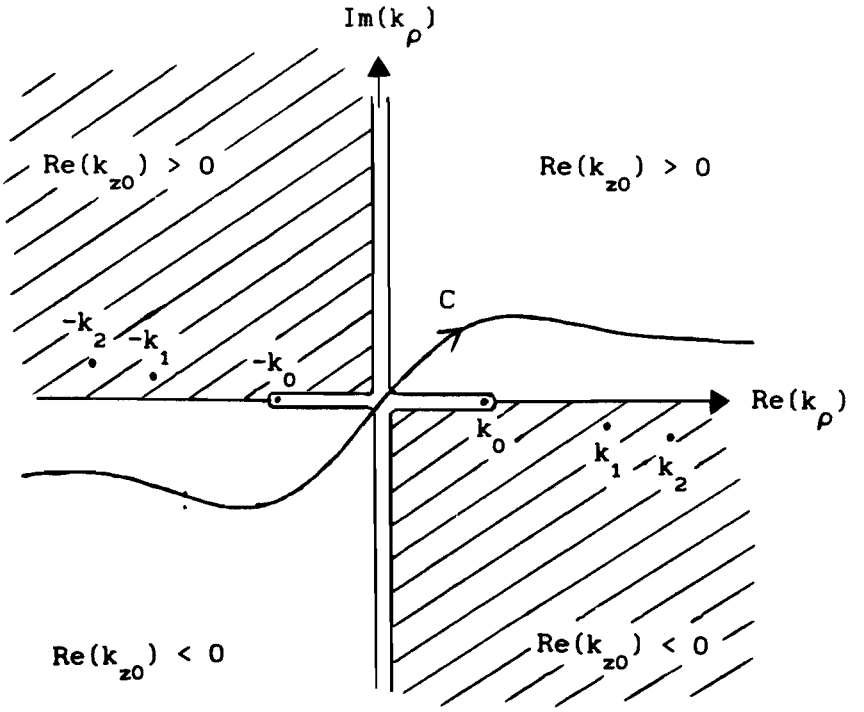

Fig. 2.10 Proper sheet of the k_ρ-plane ($\mathrm{Im}(k_{z0}) < 0$)

The hatched regions in the above figure indicate regions, which, when mapped onto the k_{z0}-plane, give values for k_{z0} with negative real parts, in contrast with the radiation condition, and can thus be classified as forbidden regions. This means that the integration path C is restricted to lie in the first and third quadrant of the complex k_ρ-plane only. An arbitrary infinite integration path C going from the third to the first quadrant and crossing between both at the origin is shown in figure 2.10 [9]. It looks as though the integration path crosses the branch cuts at the origin, but it merely touches them there, which can be made more clear if a small negative imaginary loss-term is introduced in k_0^2; see the Appendix.

In figure 2.10 the only branch cuts which are present are those arising from the function $k_{z0}(k_\rho)$. The other two-valued functions $k_{z1}(k_\rho)$ and $k_{z2}(k_\rho)$ do not introduce any branch cuts in the k_ρ-plane. This is because, first of all, the axial wavenumbers k_{z1} and k_{z2} in the dielectric layers are not restricted to a range of values due to some condition, as was the case for k_{z0} due to the radiation condition. The integration path C may thus lie on either of the two sheets of the Riemann-surface of the k_ρ-plane, arising from the two valued functions $k_{z1} = (k_1^2 - k_\rho^2)^{1/2}$ and $k_{z2} = (k_2^2 - k_\rho^2)^{1/2}$, and is not restricted to any region on these sheets, provided it does not cross their respective branch cuts because the integrands must still be single-valued. But, more important, it can easily be shown by inspection from Eqns. (2.42)-(2.44), (2.48), (2.49) and (2.53) that the integrands of the Sommerfeld-type integrals are even functions of both u_1 and u_2. This implies that the values of the integrands do not depend on the sign of the complex roots of $(k_1^2 - k_\rho^2)$ and $(k_2^2 - k_\rho^2)$ for a particular k_ρ and are therefore always single-valued with respect to the functions $k_{z1}(k_\rho)$ and $k_{z2}(k_\rho)$. Consequently, branch cuts are not needed in this case to ensure the single-valuedness of the integrands.

The topology of the complex k_ρ-plane given in figure 2.10 is not yet complete. This is because the Hankelfunctions appearing in the Sommerfeld-integral (2.128) are, in general, multivalued [26]. For values $k_\rho\xi$ with arguments between $-\pi$ and π they are however single-valued, so the Hankelfunction introduces a branch cut along the negative real axis arising from the branch point at the origin of the k_ρ-plane, where the Hankelfunction has a logarithmic singularity.

Now that the k_ρ-plane has been completely specified, a proper integration path has to chosen. As stated above, this infinite path must lie in the third and first quadrant, and, as long as it remains within these regions, an arbitrary integration path can be specified through continuous deformation of the path. However, a complex integration path with both real and imaginary parts is quite laborious, so one usually deforms C into either the imaginary (ν) or the real (λ) axis of the k_ρ-plane [9,pp.194-206]. Since losses may be present, the first approach will not do and the latter is thus chosen and has proven to be the most efficient one [13].

When deforming the integration path into the real axis care has to be taken, because various singularities are, or can be, situated on the real axis. These singularities must therefore first be investigated, and, if necessary, appropriate action must be taken to account for the various types of singularities, for instance by letting the integration path go round a particular singularity.

Possible singularities which lie on the real axis occur at $k_\rho = 0$, due to the Hankelfunction $H_n^{(2)}$, and at the roots of the complex function u_0, namely at $\lambda = \pm k_0$. The latter are branch points, due to u_0 (or k_{z0}), which are another type of singularity, besides for instance poles, where the derivative of the function does not exist [27,p.296]. It can even be shown more specifically that the functions f appearing in (2.128), when evaluated along the real axis, have a discontinuous derivative at $\lambda = k_0$ [9]. The singularities at $\lambda = \pm k_0$ are however so-called removable singularities because it is easy to show that, when taking the limit $k_\rho \to \pm k_0$ or $u_0 \to 0$ in the functions f $= f_{xi}$, f_{zi} or f_{vi}, Eqns. (2.42)-(2.44), (2.48), (2.49) and (2.53), the integrand remains finite. Subsequently, the integrand has a zero residue at these branch points. The logarithmic Hankel singularity at $k_\rho = 0$ can as easily be removed, because, as can be seen from the general form of the Sommerfeld-type integrals (2.128), a factor k_ρ is also part of the integrand.

Other singularities, which are only situated on the real axis in the case without losses, are first of all the roots of the complex functions u_1 and u_2, located at $k_\rho = \pm k_1$ and $k_\rho = \pm k_2$, respectively, and secondly any roots of the factors D_{TM} and D_{TE}, the TM- and TE-surface-wave poles. The former are, as has been shown, not branch points like $k_\rho = \pm k_0$ and therefore the derivatives

of the integrands at these points exist and are continuous [9], but they are still present as roots in certain denominators within the functions f = f_{xi}, f_{zi} and f_{vi}. Simple inspection of these functions will reveal that they also remain finite at $k_\rho = \pm k_1$, and $k_\rho = \pm k_2$, and that therefore any integration can be performed through these points, which can lie on the real axis depending on the amount of loss introduced.

The location of the surface-wave poles also depend on the amount of loss present. It was assumed that only the dominant TM_0-surface-wave mode can be excited, and if its corresponding pole is denoted as $\lambda_p + j\nu_p$, then it was shown in the previous section that with regard to its position the following holds (fourth quadrant pole):

$$\begin{cases} k_0 \leq \lambda_p \leq k_0\sqrt{\varepsilon'_{rmax}} \\ \nu_p \leq 0 \end{cases} \qquad (2.129)$$

with $\nu_p = 0$ in the lossless case. This surface-wave pole, which is of first order, is a singularity which cannot be removed and is always present on or very close to the real axis. If it is situated on the real axis the integration path must go around it, but let us at first assume that a certain amount of loss is introduced and that therefore the integrands do not become singular at any point on the real axis.

The above shows that the integration path C can under these circumstances be deformed into the real axis, without any difficulties:

$$\int_C H_n^{(2)}(k_\rho \xi)\; k_\rho^{n+1}\; f(k_\rho, z, z')dk_\rho = \int_{-\infty}^{\infty} H_n^{(2)}(\lambda\xi)\; \lambda^{n+1}\; f(\lambda, z, z')d\lambda \qquad (2.130)$$

Using the following properties of Hankel- and Besselfunctions [28]:

$$\begin{aligned} H_n^{(2)}(ze^{-\pi j}) &= -\, e^{n\pi j}\, H_n^{(2)}(z) \\ H_n^{(1)}(z) + H_n^{(2)}(z) &= 2\, J_n(z) \end{aligned} \qquad (2.131)$$

and the fact that f is an even function of λ

$$f(-\lambda, z, z') = f(\lambda, z, z') \qquad (2.132)$$

the Sommerfeld-type integral can be rewritten as

$$\int_{-\infty}^{\infty} H_n^{(2)}(\lambda\xi)\ \lambda^{n+1}\ f(\lambda,z,z')d\lambda \ = 2\int_{0}^{\infty} J_n(\lambda\xi)\ \lambda^{n+1}\ f(\lambda,z,z')d\lambda \qquad (2.133)$$

which is a form particularly well suited for numerical evaluation.

Although the integrands which contain the term D_{TM} are regular all along the real integration axis when losses are present, the complex surface-wave pole has a strong influence on the behaviour of the integrands near this pole. This may present numerical difficulties when calculating the Sommerfeld-integrals. It is even so that the integral, as it is formulated according to (2.133), is theoretically incorrect in the limiting case $\nu_p \to 0$, in which case the pole is situated on the real axis at $\lambda = \lambda_p$. A technique called "extraction of the singularity" can deal with these problems satisfactorily in all cases, i.e., with or without losses [13]. First, the singular part of the integrand is extracted according to:

$$\begin{aligned} J_n(\lambda\xi)\ \lambda^{n+1}\ f(\lambda,z,z') &= \left\{ J_n(\lambda\xi)\ \lambda^{n+1}\ f(\lambda,z,z') - F_{sing}(\lambda) \right\} + F_{sing}(\lambda) \\ &= F_{reg}(\lambda) + F_{sing}(\lambda) \end{aligned} \qquad (2.134)$$

The singular part is given by the principal part of the Laurent-series, evaluated for points on the real axis, which, because $\lambda_p + j\nu_p$ is a simple pole, is given by

$$F_{sing}(\lambda) = \frac{R}{\lambda - (\lambda_p + j\nu_p)} \qquad (2.135)$$

with R being the residue of the integrand at the pole. Writing the function f as $f(k_\rho,z,z') = g(k_\rho,z,z')/D_{TM}(k_\rho)$ with $g(k_\rho,z,z') \neq 0$ for $\lambda_p + j\nu_p$, this residue can be calculated as follows:

$$\begin{aligned} R &= J_n((\lambda_p + j\nu_p)\xi)\ (\lambda_p + j\nu_p)^{n+1} \lim_{k_\rho \to \lambda_p + j\nu_p} (k_\rho - \lambda_p - j\nu_p) f(k_\rho,z,z') \\ &= J_n((\lambda_p + j\nu_p)\xi)\ (\lambda_p + j\nu_p)^{n+1} \lim_{k_\rho \to \lambda_p + j\nu_p} (k_\rho - \lambda_p - j\nu_p) \frac{g(k_\rho,z,z')}{D_{TM}(k_\rho)} \end{aligned}$$

$$= J_n((\lambda_p + j\nu_p)\xi)\ (\lambda_p + j\nu_p)^{n+1}\ \frac{g(\lambda_p + \nu_p, z, z')}{D'_{TM}(\lambda_p + \nu_p)} \qquad (2.136)$$

The last step in (2.136) follows from expanding $D_{TM}(k_\rho)$ in a Taylor-series around $k_\rho = \lambda_p + \nu_p$.

After extracting the singularity the remaining regular part is well-behaved and will be integrated using numerical integration procedures. The singular part can be integrated analytically, and if the semi-infinite integration interval is divided into three parts, $[0, k_0]$, $[k_0, k_0\sqrt{\varepsilon'_{rmax}}]$ and $[k_0\sqrt{\varepsilon'_{rmax}}, \infty]$, then the integral over the middle interval, in which the real part of the singularity lies, yields [13]

$$\int_{k_0}^{k_0\sqrt{\varepsilon'_{rmax}}} F_{sing}(\lambda)\, d\lambda = \frac{R}{2}\ \ln\left\{ \frac{\nu_p^2 + (k_0\sqrt{\varepsilon'_{rmax}} - \lambda_p)^2}{\nu_p^2 + (k_0 - \lambda_p)^2} \right\}$$
$$+ jR\left[\arctan\left\{ \frac{k_0\sqrt{\varepsilon'_{rmax}} - \lambda_p}{\nu_p} \right\} + \arctan\left\{ \frac{\lambda_p - k_0}{\nu_p} \right\} \right] \qquad (2.137)$$

To show that extraction of the singularity also proves to be correct when no losses are present, taking the limit $\nu_p \to 0$ ($\nu_p \leq 0$) in (2.137) gives:

$$\int_{k_0}^{k_0\sqrt{\varepsilon'_{rmax}}} F_{sing}(\lambda)\, d\lambda = R\ \ln\left\{ \frac{k_0\sqrt{\varepsilon'_{rmax}} - \lambda_p}{\lambda_p - k_0} \right\} - j\pi R \qquad (2.138)$$

This is precisely the same result which would have been obtained if the integration was performed through a small semi-circle around the pole and using residue-calculus [24].

The numerical integration of the regular part of the integrand and also the integration of the integrand, without extraction, over the other integration intervals on the real axis shall be dealt with in the next chapter. There, also other various topics relating to the numerical evaluation of the microstrip antenna, such as for instance the calculation of the "method-of-moments" matrix, will be investigated.

3 COMPUTATIONAL DETAILS

If the theoretical analysis of the stacked microstrip antenna given in the previous chapter is to be used for accurately predicting the antenna characteristics which are of interest here, namely its resonant behaviour and input-impedance, it has to be implemented in computer software. The numerical implementation of the analysis of the microstrip antenna must above all focus on efficient and accurate numerical techniques for dealing with the calculation of the "method-of-moments" matrix and the Green's functions, because they have a great influence of the accuracy of the overall results. Furthermore, some thought has to be given to the aspect of computation time, since electromagnetic problems like those presented in this report often require lengthy computations. This chapter deals with all the various items which are needed to translate the given analysis into a form suited to efficient numerical computations. Full advantage has been taken of the work performed by Mosig et.al. on this subject [3][9][13].

3.1 Calculation of the "method-of-moments" solution of the microstrip problem

First the calculation of the expansion-mode coefficients α_{1j} from the matrix-equation (2.98)/(2.99) shall be investigated. The numerical evaluation will be divided into three parts, which are the filling of the matrix $\bar{\bar{C}}$, the calculation of the excitation vector $\bar{b}$ and obtaining the solution of the set of linear equations with complex coefficients $\bar{\bar{C}} \cdot \bar{\alpha} = \bar{b}$. Especially the first one will require a detailed examination because of the four-fold integrals present in the matrix elements, Eqn. (2.101). In the following these three consecutive steps will be investigated separately.

3.1.1 Calculation of the matrix elements

The Galerkin solution of the mixed-potential integral-equation has resulted in a matrix-equation in which the matrix-elements are given by modal

interactions of the test- and expansion-functions, given by Eqn. (2.101). The last term of these matrix-elements (ohmic-loss term) is a simple surface integration over the rectangular patch S_i of an inner product of two known current expansion functions $\bar{f}_{ki}$ and $\bar{f}_{lj}$, these functions having the general form given by expression (2.105). This term is zero for current modes on different patches, and for current modes of the same patch it can easily be found in closed form.

More difficult, however, is the computation of the other two terms in the matrix-element $C_{ki,lj}$, which are the contributions from the magnetic vector potential $\bar{A}$ and the scalar potential V and which cannot be found in closed form. This is because these terms, first of all, involve a four-fold spatial integration over two patches, which can either be the integration over the two different patches or two integrations over the same patch. The second difficulty is the presence of the Green's functions in those integrals, who themselves are also given as integrals for which no closed expression can be found. If it is assumed that the Green's functions are available in the form of a numerical routine of some sort, applying a numerical integration procedure for handling multiple integrations directly to these four-fold integrals would still not be recommendable because of the accuracy which can be obtained with regard to the four numerical integrations, and particularly the computation time needed to calculate the integrals.

It is possible however, as will be shown in detail below, to reduce the four-fold integrals to double integrals, using a particularly convenient change in variables, after which two of the four integrations are performed analytically [3]. This will result in a significant reduction in computation time since now only two integrations have to be carried out using numerical integration procedures, which then will also have an effect on the precision of the calculations because analytic integrations are always more accurate.

As a first step, the form of the quadruple integrals, present in the matrix-elements must be investigated. Substituting Eqn. (2.91) for the dyadic Green's function $\bar{\bar{G}}_A$ into the first term of (2.101), and writing the current modes (2.105) as $\bar{f}_{ki} = f^x_{ki}\hat{e}_x + f^y_{ki}\hat{e}_y$ this integral has the following form:

$$\int_{S_i}\int_{S_j} G_A^{xx}(\bar{r}_i/\bar{r}_j)\{\, f_{ki}^x(\bar{r}_i)f_{lj}^x(\bar{r}_j) + f_{ki}^y(\bar{r}_i)f_{lj}^y(\bar{r}_j)\,\}\, ds_j ds_i \qquad (3.1)$$

Separating the charge expansion function h_{ki}, Eqn. (2.106), into an "x- and y-component" according to $h_{ki} = h_{ki}^x + h_{ki}^y$ the second term reads

$$\int_{S_i}\int_{S_j} G_v^H(\bar{r}_i/\bar{r}_j)\{\, h_{ki}^x(\bar{r}_i)h_{lj}^x(\bar{r}_j) + h_{ki}^x(\bar{r}_i)h_{lj}^y(\bar{r}_j) + h_{ki}^y(\bar{r}_i)h_{lj}^x(\bar{r}_j) + h_{ki}^y(\bar{r}_i)h_{lj}^y(\bar{r}_j)\,\}\, ds_j ds_i \qquad (3.2)$$

Both (3.1) and (3.2) are sums of integrals of a more or less similar form and we shall therefore investigate the following general four-fold integral:

$$\int_{S_i}\int_{S_j} G(\bar{r}_i/\bar{r}_j)\, f_i(\bar{r}_i)\, f_j(\bar{r}_j)\, ds_j ds_i \qquad (3.3)$$

in which a general Green's function G stands for either G_A^{xx} or G_v^H and the functions f_i and f_j for f_{ki}^x, f_{ki}^y, h_{ki}^x or h_{ki}^y and f_{lj}^x, f_{lj}^y, h_{lj}^x or h_{lj}^y, respectively. The latter are simple products of trigonometric functions as can be seen from expressions (2.105) and (2.106).

The key to the reduction of the integral (3.3) to a double integral is the fact that the radial dependence of the Green's functions is of the form $|\bar{\rho} - \bar{\rho}'|$, Eqn. (2.59a). The Green's function can thus be written as follows:

$$G(\bar{r}_i/\bar{r}_j) = G(|\bar{\rho}_i - \bar{\rho}_j|, z_i, z_j) = G(x_i - x_j, y_i - y_j, z_i, z_j) \qquad (3.4)$$

If one now makes the change of variables

$$\begin{aligned}
x_i - x_j = p_1 \quad &: \quad x_i = \tfrac{1}{2}p_1 + \tfrac{1}{2}p_2 \\
x_i + x_j = p_2 \quad &: \quad x_j = \tfrac{1}{2}p_2 - \tfrac{1}{2}p_1 \\
y_i - y_j = q_1 \quad &: \quad y_i = \tfrac{1}{2}q_1 + \tfrac{1}{2}q_2 \\
y_i + y_j = q_2 \quad &: \quad y_j = \tfrac{1}{2}q_2 - \tfrac{1}{2}q_1
\end{aligned} \qquad (3.5)$$

the integral can be rewritten according to

$$\iiiint G(x_i - x_j, y_i - y_j, z_i, z_j)\, f_i(x_i, y_i)\, f_j(x_j, y_j)\, dx_i dy_i dx_j dy_j$$

$$= \iiiint G(p_1, q_1, z_i, z_j)\, f_i(\tfrac{1}{2}p_1 + \tfrac{1}{2}p_2, \tfrac{1}{2}q_1 + \tfrac{1}{2}q_2)$$

$$f_j(\tfrac{1}{2}p_2 - \tfrac{1}{2}p_1, \tfrac{1}{2}q_2 - \tfrac{1}{2}q_1) \left| \frac{\partial(x_i, x_j, y_i, y_j)}{\partial(p_1, p_2, q_1, q_2)} \right| dp_1 dp_2 dq_1 dq_2 \qquad (3.6)$$

with the Jacobian or functional determinant given by

$$\frac{\partial(x_i, x_j, y_i, y_j)}{\partial(p_1, p_2, q_1, q_2)} = \begin{vmatrix} \frac{\partial x_i}{\partial p_1} & \frac{\partial x_i}{\partial p_2} & \frac{\partial x_i}{\partial q_1} & \frac{\partial x_i}{\partial q_2} \\ \frac{\partial x_j}{\partial p_1} & \frac{\partial x_j}{\partial p_2} & \frac{\partial x_j}{\partial q_1} & \frac{\partial x_j}{\partial q_2} \\ \frac{\partial y_i}{\partial p_1} & \frac{\partial y_i}{\partial p_2} & \frac{\partial y_i}{\partial q_1} & \frac{\partial y_i}{\partial q_2} \\ \frac{\partial y_j}{\partial p_1} & \frac{\partial y_j}{\partial p_2} & \frac{\partial y_j}{\partial q_1} & \frac{\partial y_j}{\partial q_2} \end{vmatrix} = \frac{1}{4} \qquad (3.7)$$

Expression (3.6) shows that with this change of variables the Green's function is only a function of the integration variables (p_1, q_1). It is now possible to perform the integration over (p_2, q_2) analytically since f_i and f_j are products of sine- and cosine-functions.

The main problem now is to find the integration boundaries for (p_1, q_1) and (p_2, q_2). They are no longer as simple as those for (x_i, y_i) and (x_j, y_j) and they are also interrelated. Let us first look at the original integration boundaries for integration over the patches S_1 and S_2 as depicted in figure 3.1, given with respect to local coordinates (x,y) fixed to the lower patch, and for an arbitrary shift of the upper patch with respect to the lower patch.

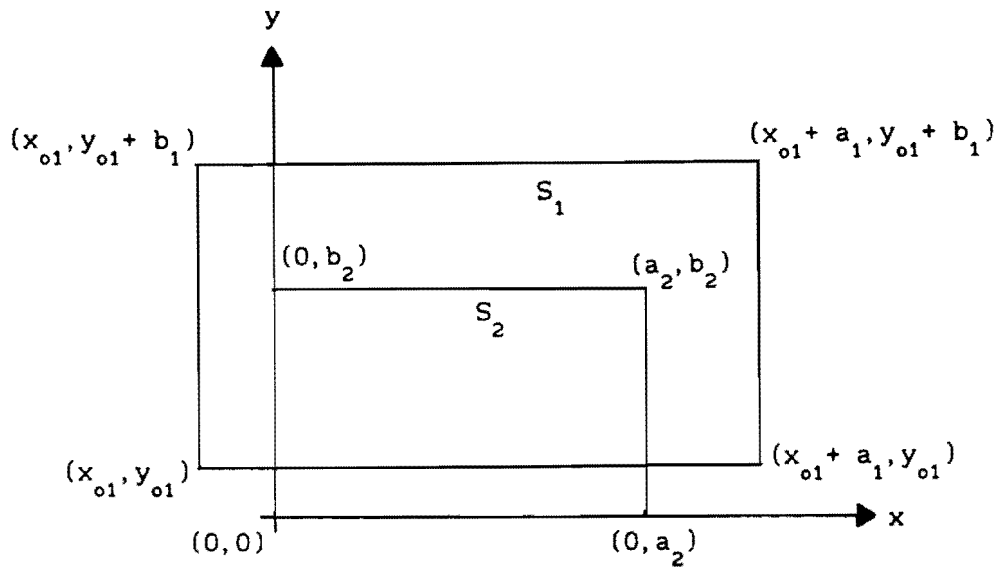

Fig. 3.1 Top view patches S_1 and S_2 in coordinate system (x,y)

As a generalization, the lower and upper integration boundaries for patch $S_{i,j}$ shall be denoted as $x^-_{i,j}$ and $x^+_{i,j}$, respectively, in the x-direction and as $y^-_{i,j}$ and $y^+_{i,j}$, respectively, in the y-direction ($i,j = 1,2$). These boundaries are given with respect to the local coordinate system shown in figure 3.1, and in terms of the dimension of the patches and the offset they are given by: $x^-_1 = x_{o1}$, $x^+_1 = x_{o1} + a_1$, $y^-_1 = y_{o1}$, $y^+_1 = y_{o1} + b_1$, $x^-_2 = 0$, $x^+_2 = a_2$, $y^-_2 = 0$, $y^+_2 = b_2$. Furthermore it is assumed that there is always an overlap between the upper and lower patch: $x^-_i < x^+_j$, $x^+_i > x^-_j$, $y^-_i < y^+_j$, $y^+_i > y^-_j$ for $i,j = 1,2$ and $i \neq j$. For $i = j$ these last conditions are always met. This last assumption does not impose any actual restriction on the design of the stacked microstrip antenna because there is always some overlap needed to provide a good electromagnetic coupling between the upper and lower patch so that the microstrip antenna acts as one single device. No overlap means that the microstrip structure actually consists of two separate microstrip patch antennas on different layers, of which one has a poor coupling with the coaxial feed.

In general, the integration boundaries for p_1, q_1, p_2 and q_2 must now be

found from those for x_i, y_i, x_j and y_j. Observing the change of variables (3.5), the integration boundaries for (p_1,p_2) can be found exclusively from those for (x_i,x_j), and also those for (q_1,q_2) from only the boundaries for (y_i,y_j). Since the formulas describing the change of variables $(x_i,x_j) \rightarrow (p_1,p_2)$ are exactly the same as those for $(y_i,y_j) \rightarrow (q_1,q_2)$ only the first one shall be considered in detail in the following.

Because x_i and x_j are independent integration variables on their respective integration intervals $[x_i^-,x_i^+]$ and $[x_j^-,x_j^+]$, the "surface" over which the integration is performed in the x_i-x_j-plane is a rectangle (Fig. 3.2 for arbitrary boundary values).

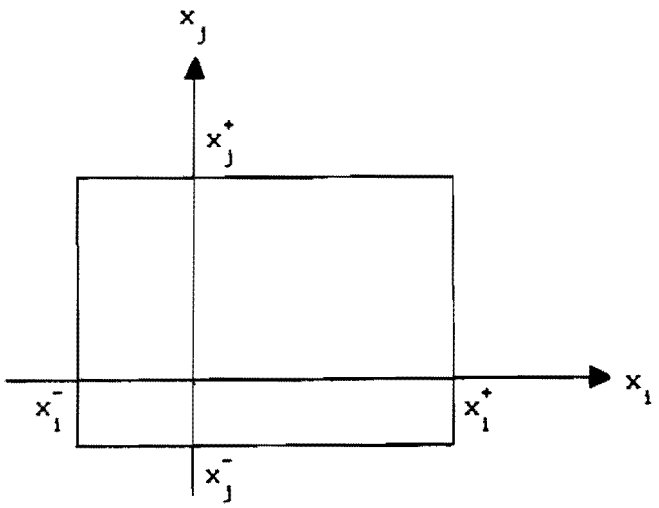

Fig. 3.2 Integration surface in the x_i-x_j-plane

This integration-surface is transformed into a surface of integration in the p_1-p_2-plane by using Eqns. (3.5), resulting in figure 3.3, in which two separate cases which can be distinguished are depicted, namely $x_i^- - x_j^+ < x_i^- - x_j^- \leq x_i^+ - x_j^+ < x_i^+ - x_j^-$ (Fig. 3.3a) and $x_i^- - x_j^+ < x_i^+ - x_j^+ \leq x_i^- - x_j^- < x_i^+ - x_j^-$ (Fig. 3.3b).

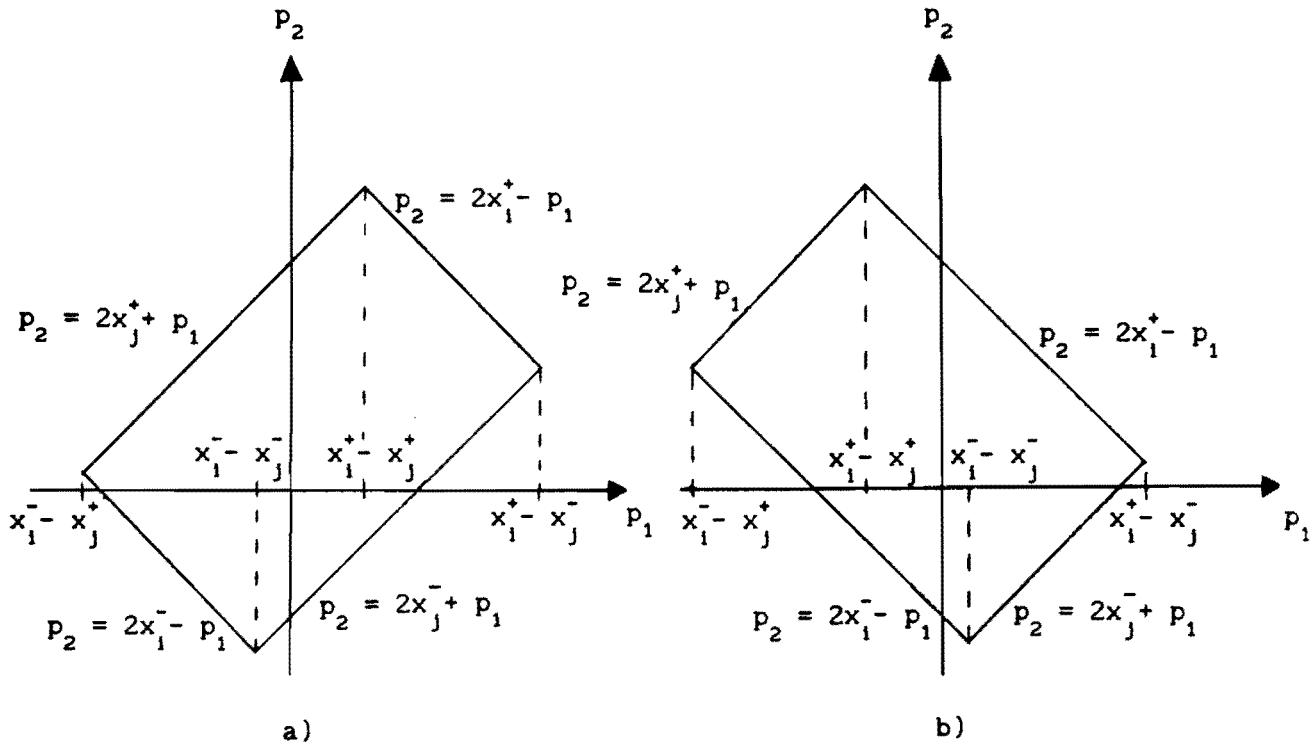

Fig. 3.3 Integration surface in the p_1-p_2-plane, (a) $x_i^- - x_j^- \leq x_i^+ - x_j^+$ and (b) $x_i^+ - x_j^+ \leq x_i^- - x_j^-$

These figures show that the boundaries for integration over p_2 now depend on the value of the integration variable p_1 and also on the particular interval on the p_1-axis in which p_1 lies. Changing x into y and p into q in figure 3.3 gives the integration boundaries for q_1 and q_2.

With figure 3.3 in mind the four-fold integral (3.6) can now be written as

$$\frac{1}{4} \int_{x_i^- - x_j^+}^{x_i^+ - x_j^-} \int_{y_i^- - y_j^+}^{y_i^+ - y_j^-} G(p_1, q_1, z_i, z_j)\, F(p_1, q_1)\, dp_1 dq_1 \qquad (3.8)$$

with the analytic function F given by

$$F(p_1, q_1) = \int_{p_2^-(p_1)}^{p_2^+(p_1)} \int_{q_2^-(q_1)}^{q_2^+(q_1)} f_i(\tfrac{1}{2}p_1 + \tfrac{1}{2}p_2, \tfrac{1}{2}q_1 + \tfrac{1}{2}q_2)\, f_j(\tfrac{1}{2}p_2 - \tfrac{1}{2}p_1, \tfrac{1}{2}q_2 - \tfrac{1}{2}q_1)\, dp_2 dq_2 \qquad (3.9)$$

The integration boundaries $p_2^-(p_1)$, $p_2^+(p_1)$, $q_2^-(q_1)$ and $q_2^+(q_1)$ in (3.9) can be found from figure 3.3. The actual calculation of the analytic integral (3.9) with all the appropriate sinusoidal expansion functions inserted for f_i and f_j shall not be performed here. This is because, although very straightforward, it is rather tedious, due to the fact that according to figure 3.3 two specific cases must be considered and that furthermore in each of these cases the integral (3.9) must be calculated for all functions f_i and f_j appearing in (3.1) and (3.2) and for all combinations (p_1,q_1), since both p_1 and q_1 can each lie in one of three integration intervals, namely three intervals with boundaries $x_i^- - x_j^+$, $x_i^- - x_j^+$, $x_i^+ - x_j^+$ and $x_i^+ - x_j^-$ for the variable p_1 and similar ones for q_1, see figure 3.3, and these intervals determine the actual integration boundaries $p_2^-(p_1)$, $p_2^+(p_1)$, $q_2^-(q_1)$ and $q_2^+(q_1)$. This amounts to a total of 84 different integrals $F(p_1,q_1)$ which should be calculated. It is easier to implement the calculation of (3.9) in a general routine, since the actual expansion functions all have a similar form, Eqns. (2.105) and (2.106), for which the indefinite integrals are easily found, after which the value for p_1 and the proper boundaries $p_2^-(p_1)$, $p_2^+(p_1)$, $q_2^-(q_1)$ and $q_2^+(q_1)$ can be inserted.

A numerical integration procedure must be used for dealing with the double integral (3.8), which can be identified as a double spatial integration over a rectangle in the p_1-q_1-plane. However, a numerical difficulty arises when calculating the interaction between two expansion modes on the same patch ($z_i = z_j$) because the Green's functions G_A^{xx} and G_v^H exhibit a spatial singularity of type ξ^{-1} when source ($\bar{\rho}'$ or $\bar{\rho}_j$) and observation ($\bar{\rho}$ or $\bar{\rho}_i$) point coincide, which in the p_1-q_1-plane occurs at the origin $p_1 = q_1 = 0$. In these cases integral (3.8), although it exists formally, can be greatly simplified numerically by first reducing it to an integration over the first quadrant of the p_1-q_1-plane according to (*valid only for $i = j$*)

$$\frac{1}{4}\int_0^{x_i^+-x_j^-}\int_0^{y_i^+-y_j^-} G(p_1,q_1,z_i,z_j)\,\{F(p_1,q_1) + F(p_1,-q_1) + F(-p_1,q_1) + F(-p_1,-q_1)\}\,dp_1dq_1 \qquad (3.10)$$

using the fact that $x_i^- - x_j^- = x_i^+ - x_j^+ = 0$ (Fig. 3.3), and that the dependence of G on the variables p_1 and q_1 is of the form $\xi = |\bar{\rho}_i - \bar{\rho}_j| = ((x_i - x_j)^2 +$

$$(y_i - y_j)^2)^{1/2} = (p_i^2 + q_i^2)^{1/2}.$$

Secondly the spatial singularity in (3.10) at $p_i = q_i = 0$ can be removed by changing to polar coordinates [3], $p_i = \xi\cos\theta$ and $q_i = \xi\sin\theta$, resulting in

$$\frac{1}{4}\int_0^{\pi/2}\int_0^{\xi^+(\theta)} G(\xi, z_i, z_j)\,\{F(\xi\cos\theta, \xi\sin\theta) + F(\xi\cos\theta, -\xi\sin\theta) + F(-\xi\cos\theta, \xi\sin\theta) + F(-\xi\cos\theta, -\xi\sin\theta)\}\,\xi d\xi d\theta \qquad (3.11)$$

with

$$\xi^+(\theta) = \frac{x_i^+ - x_j^-}{\cos\theta} \quad \text{for} \quad 0 \le \theta \le \arctan\left(\frac{y_i^+ - y_j^-}{x_i^+ - x_j^-}\right)$$

$$\xi^+(\theta) = \frac{y_i^+ - y_j^-}{\sin\theta} \quad \text{for} \quad \arctan\left(\frac{y_i^+ - y_j^-}{x_i^+ - x_j^-}\right) \le \theta \le \frac{\pi}{2} \qquad (3.12)$$

For i = j the integrals (3.1) and (3.2) shall thus be calculated according to (3.11)-(3.12) and a so-called "product-rule" for calculating double integrals numerically shall be employed on both integration intervals (3.12) separately, using a 61-point Gauss-Kronrod integration rule for the integrations over ξ and θ [31]. The routine given in [31] has been slightly modified so that it can be used to accommodate the real and imaginary part of the complex integrand (G_A^{xx} and G_v^H are complex) simultaneously.

The integrals which make up the cross-terms in the matrix-elements $C_{ki,lj}$, $i \neq j$, can be computed directly from (3.8). Although there is no spatial singularity at $p_i = q_i = 0$, the Green's function can still have a strong variation near this point, especially for thin upper substrates. This is because even though source ($\bar{r}_j$) and observation ($\bar{r}_i$) points lie on different z-planes, the fields or potentials at the latter point are significantly influenced by the singularity if $\bar{r}_i$ in the z_i-plane lies just above or below $\bar{r}_i$ in the z_j-source-plane. A fixed point globally adaptive integration routine, taking more integration points near $(p_i, q_i) = (0,0)$, and using the product-rule and 61-point Gauss-Kronrod integration routines for integration over p_i and q_i will suffice for accurately calculating the integral (3.8) for $i \neq j$.

Due to the symmetry of the "method-of-moments" matrix, only those matrix elements on and above the main diagonal need to be calculated, see Eqns. (2.99) and (2.102).

The procedure presented in this section for reducing the four-fold integral into a two-fold integral seems to be less suited if instead of rectangular patches, circular patches were used together with appropriate entire-domain basis functions for expanding the patch currents on circular patches. For circular patches integrals like (3.3) can best be handled in polar coordinates $(x_i, y_i) = (\rho_i \cos\phi_i, \rho_i \sin\phi_i)$ and $(x_j, y_j) = (\rho_j \cos\phi_j, \rho_j \sin\phi_j)$. But then the radial dependence of the Green's functions, $\xi = |\bar{\rho}_i - \bar{\rho}_j|$ has the form

$$\left(\rho_i^2 + \rho_j^2 - 2\rho_i\rho_j \cos(\phi_i - \phi_j) \right)^{1/2} \qquad (3.13)$$

A simple change of variables like Eqns. (3.5), so that the Green's functions only depend on two integration variables, instead of the previous four, is not available in this case. Staying with rectangular coordinates instead for integrating over the circular patches, and changing variables according to (3.5) make things even more complicated for circular patches, because the original integration boundaries for $x_{i,j}$ depend on those for $y_{i,j}$, $x^-_{i,j} = x^-_{i,j}(y_{i,j})$ and $x^+_{i,j} = x^+_{i,j}(y_{i,j})$, or vice versa, so that finding the integration boundaries for (p_1, q_1) and (p_2, q_2) may not be possible.

Thus, using the space domain approach with entire domain basis-functions, as presented in this report for rectangular microstrip patches, does not lend itself particularly well for analyzing microstrip antennas with circular patches or even more complicated patch shapes. In these cases one can consider subdomain basis-functions instead of entire-domain basis-functions [9][12][15] or use the spectral domain approach [6][7][8].

3.1.2 Calculation of the excitation elements

Much simpler is the calculation of the excitation vector $\bar{b}$, whose elements are given by Eqn. (2.100) as a double integral over one of the microstrip patches of the product of the Green's function $G_v^v(\bar{r}/\bar{r}')$ and the charge expansion function $h_{k1}(\bar{r})$. The main problem which arises here is integration over that patch which contains the coaxial probe's insertion point, namely the lower patch S_2. The Green's function G_v^v has a first order singularity if the observation- or integration-variable $\bar{r} = \bar{r}_i$ coincides with the source- or coaxial-feed-point $\bar{r}' = \bar{r}_c$. As in the previous section this singularity can be removed by changing to polar coordinates.

Observing figure 3.1, the origin of the x-y-coordinate system is first shifted towards the feed point (x_c, y_c) by making a change of variables $x_2 - x_c \rightarrow x$ and $y_2 - y_c \rightarrow y$, which yields *(i = 2 only)*:

$$b_{k2} = - I \int_{x_2^-}^{x_2^+} \int_{y_2^-}^{y_2^+} G_v^v(x_2 - x_c, y_2 - y_c, z=0)\, h_{k1}(x_2, y_2)\, dx_2 dy_2 \qquad k=1, \cdots, N_2$$

$$= - \int_{x_2^- - x_c}^{x_2^+ - x_c} \int_{y_2^- - y_c}^{y_2^+ - y_c} G_v^v(x, y, z=0)\, h_{k1}(x + x_c, y + y_c)\, dxdy \qquad (3.14)$$

Changing to polar coordinates $x = \xi\cos\theta$ and $y = \xi\sin\theta$ and remembering that the spatial variation of the Green's function in the transverse direction is of the form $|\bar{\rho}_2 - \bar{\rho}_c| = ((x_2 - x_c)^2 + (y_2 - y_c)^2)^{1/2} = (x^2 + y^2)^{1/2}$, the excitation elements for the expansion modes on the lower patch can be calculated according to

$$b_{k2} = - I \int_0^{2\pi} \int_0^{\xi^+(\theta)} G_v^v(\xi, z=0)\, h_{k1}(\xi\cos\theta + x_c, \xi\sin\theta + y_c)\, \xi d\xi d\theta \qquad (3.15)$$

with

$$
\begin{aligned}
\xi^+(\theta) &= \frac{x_2^+ - x_c}{\cos\theta}\,, && 0 \le \theta \le \arctan\left(\frac{y_2^+ - y_c}{x_2^+ - x_c}\right)\\
\xi^+(\theta) &= \frac{y_2^+ - y_c}{\sin\theta}\,, && \arctan\left(\frac{y_2^+ - y_c}{x_2^+ - x_c}\right) \le \theta \le \arctan\left(\frac{y_2^+ - y_c}{x_2^- - x_c}\right) + \pi\\
\xi^+(\theta) &= \frac{x_2^- - x_c}{\cos\theta}\,, && \arctan\left(\frac{y_2^+ - y_c}{x_2^- - x_c}\right) + \pi \le \theta \le \arctan\left(\frac{y_2^- - y_c}{x_2^- - x_c}\right) + \pi\\
\xi^+(\theta) &= \frac{y_2^- - y_c}{\sin\theta}\,, && \arctan\left(\frac{y_2^- - y_c}{x_2^- - x_c}\right) + \pi \le \theta \le \arctan\left(\frac{y_2^- - y_c}{x_2^+ - x_c}\right) + 2\pi\\
\xi^+(\theta) &= \frac{x_2^+ - x_c}{\cos\theta}\,, && \arctan\left(\frac{y_2^- - y_c}{x_2^+ - x_c}\right) + 2\pi \le \theta \le 2\pi
\end{aligned}
\qquad (3.16)
$$

To obtain a reasonable accuracy, the surface of interaction is divided into eight subintervals (eight right-angled triangles originating at the origin) with the integration boundaries given by (3.16) including three additional boundaries at $\theta = \pi/2$, π and $3\pi/2$. For each sub-integration range the product-rule for handling two-fold integrals is again employed using a fixed 61-point Gauss-Kronrod integration rule for integration over both ξ and θ [31], similar to the surface integration for calculating the matrix-elements.

Concerning the calculation of the interaction between expansion modes on the top patch and the tangential excitation field, $i = 1$, the same remark can be made as in the previous section with regard to the strong variation in G_v^v for integration points on S_1 close above the coaxial feed-point (x_c, y_c). Here too, it will be sufficiently accurate to integrate directly in rectangular coordinates (x_1, y_1) over the rectangular patch S_1, Eqn. (2.100), using the product rule, and making this routine globally adaptive when integrating close to (x_c, y_c).

3.1.3 Solution of the matrix-equation

Solving the set of linear equations with complex coefficients and a complex right-hand-side, which make up the matrix-equation $\bar{\bar{C}} \cdot \bar{\alpha} = \bar{b}$, is very

straightforward. The only problem which might arise is that for frequencies close to the resonant frequency, the determinant of the matrix is small, as outlined in section 2.6. This means that the system of linear equations might be ill-conditioned.

However, the order of the matrix is usually small since in most cases a few expansion modes are sufficient for accurately expanding the patch currents, for instance two modes per patch yield a 4x4 matrix. Furthermore, the fact that, even though the determinant shows a minimum at the *real* resonant frequency, it only vanishes completely at the *complex* resonant frequency, which indicates that standard routines for solving systems of linear equations can be used and will give correct results, since only real frequencies are considered.

Here, a simple direct method for solving matrix-equation (2.98), namely LU-decomposition, will be adequate [32]. The numerical routine from [32] only works for real matrices and therefore it has been altered so that it will be able to handle complex matrix-equations as they occur in the microstrip problem. Another possibility for handling complex matrices is to decompose the complex matrix-equation (2.98) into a real and imaginary part and forming a new matrix-equation, which has twice the size of the original one, and then solve it using a "real" procedure. These two approaches are formally equivalent and they give exactly the same results.

3.2 Calculation of the Sommerfeld-type integrals

The theory presented in section 2.9 showed that Sommerfeld-type integrals which make up the Green's functions can be transformed into a semi-infinite integral along the positive real axis, expression (2.133). Furthermore, one problem which could present major numerical difficulties, namely the surface-wave pole, has already been eliminated by extraction of this singularity. Other difficulties which shall be considered in this section are the infinite and discontinuous derivative of the integrand at the branch point $\lambda = k_0$ and the oscillating tail of the integrand at infinity [13].

As was done in section 2.9 the semi-infinite integration interval is divided into three sub-intervals, $[0,k_0]$, $[k_0,k_0\sqrt{\varepsilon'_{rmax}}]$ and $[k_0\sqrt{\varepsilon'_{rmax}},\infty]$. In the first interval the imaginary part of the integrand has an infinite derivative at $\lambda = k_0$, so that much more integration points are needed close to this point for a certain accuracy in the numerical integration to be obtained. However, this infinite derivative can be eliminated with a change of variables $\lambda = k_0 \cos t$ [13]:

$$\int_0^{k_0} J_n(\lambda\xi)\ \lambda^{n+1}\ f(\lambda,z,z')d\lambda = \int_0^{\pi/2} J_n(\xi k_0\cos t)\ (k_0\cos t)^{n+1}\ f(k_0\cos t,z,z')\ k_0\sin t\ dt \qquad (3.17)$$

Expression (3.17) shall be used for both the imaginary and real part of f, even though for the latter the change in variables is not strictly necessary. Integral (3.17) can now be calculated sufficiently accurate using a fixed point integration over the entire integration range $[0,\pi/2]$, such as for instance a single 31-point Gauss-Kronrod rule [31].

In the second integration interval $[k_0,k_0\sqrt{\varepsilon'_{rmax}}]$, two specific cases can be distinguished, namely one in which the integrands contain the term D_{TM} and from which the singular part has been extracted and the other in which the integrands do not contain D_{TM}. Both can, however, be denoted by $F_{reg}(\lambda)$, because in the latter case the regular function according to (2.134) is simply the original integrand since the residue R at the pole is zero in that case.

In this interval the real part of the integrand has an infinite derivative at $\lambda = k_0$ which can also easily be eliminated with the change of variables $\lambda = k_0 \cosh t$ [13]:

$$\int_{k_0}^{k_0\sqrt{\varepsilon'_{rmax}}} F_{reg}(\lambda)\ d\lambda = \int_0^{\operatorname{arccosh}(k_0\sqrt{\varepsilon'_{rmax}})} F_{reg}(k_0\cosh t)\ k_0\sinh t\ dt \qquad (3.18)$$

after which the same routine used for calculating (3.17) can be applied to

the integral (3.18), since the resulting function is now sufficiently well-behaved.

The last integration interval is the infinite integration range $[k_0\sqrt{\varepsilon'_{rmax}}, \infty]$ in which the integrand exhibits an oscillating tail extending to infinity. It can be shown by taking the limit $\lambda \to \infty$ that the asymptotic behaviour of the functions $f(\lambda, z, z')$ which are of interest in the solution of the microstrip problem, namely f_{x1a} and f_{x1b}, Eqns. (2.42), in the Green's function $G_A^{xx}(\bar{r}/\bar{r}')$ and f_{v1a}^H and f_{v1b}^H, Eqns. (2.53), in the Green's function $G_v^H(\bar{r}/\bar{r}')$, is of the form

$$\lim_{\lambda \to \infty} f(\lambda, z, z') \sim \frac{1}{\lambda} e^{-\lambda|z - z'|} \tag{3.19}$$

and the asymptotic behaviour of the function f_{v1}^v, Eqn. (2.86), appearing in the Green's function $G_v^v(\bar{r}/\bar{r}')$ is of the form

$$\lim_{\lambda \to \infty} f_{v1}^v(\lambda, z) \sim \frac{1}{\lambda} e^{-\lambda z}, \quad 0 \le z \le h_1 \tag{3.20}$$

Together with the asymptotic form of the Besselfunctions $J_n(\lambda\xi)$, [28], the factor λ^{n+1} present in the integrand of (2.133) and $n = 0$ since only Besselfunctions of zero order occur in G_A^{xx}, G_v^H and G_v^v, see Eqns. (2.61), (2.63) and (2.85), the total integrands behave asymptotically as

$$\lim_{\lambda \to \infty} J_0(\lambda\xi)\, \lambda\, f(\lambda, z, z') \sim \sqrt{\frac{2}{\pi\lambda\xi}} \cos(\lambda\xi - \pi/4)\, e^{-\lambda|z - z'|} \tag{3.21}$$

$$\lim_{\lambda \to \infty} J_0(\lambda\xi)\, \lambda\, f_{v1}^v(\lambda, z) \sim \sqrt{\frac{2}{\pi\lambda\xi}} \cos(\lambda\xi - \pi/4)\, e^{-\lambda z}, \quad 0 \le z \le h_1 \tag{3.22}$$

Both (3.21) and (3.22) show that in those cases in which the source- and observation-planes do not coincide the integrands show an exponential convergence, i.e., for $z \neq z'$ in (3.21) and $z \neq 0$ in (3.22), and the integral always converges. In these cases a fast convergence of the infinite integration is expected and can be carried out using a simple integration-rule per half-cycle of the oscillating Bessel-function $J_0(\lambda\xi)$.

More complicated are those cases in which the Green's functions need to be calculated for source- and observation-points in the same plane, $z = z'$ in (3.21) and $z = 0$ in (3.22). The integrand is now slowly convergent, depending on the source-observer distance ξ, and the integration has to be extended over a long integration-interval to obtain a desired accuracy. However, for these types of integrals, having an asymptotic behaviour of the form (3.21) and (3.22), very efficient methods have been developed called the "method-of-averages" and "method-of-weighted-averages". A detailed account of these methods is given in [9,p.195] and shall not be treated here. Very fast convergence of the integrals can be obtained when using these methods, with the integration range typically extending only over the first five to ten half-cycles, after the starting point $k_0\sqrt{\varepsilon'_{rmax}}$, of the oscillating Besselfunction. For calculating the integral over each half cycle a 15-point Gauss-Kronrod rule will be adequate [32].

Special attention must be paid to the minimum value ξ for which these methods can be used in the cases $z = z'$ and $z = 0$, since $\xi = 0$ corresponds to the source- and observation-points coinciding, and the Green's function has a spatial singularity for $\xi = 0$. The Sommerfeld integrals do not converge at all for $\xi = 0$, which can easily be seen from (3.21) and (3.22) with $J_0(\lambda\xi) = 1$ for $\xi = 0$ and the asymptotic forms (3.19) and (3.20) inserted, which results in a constant non-oscillating integrand extending to infinity. So a minimum value ξ_{min} must be chosen carefully for which the "method-of-averages" still provides convergence of the integral within a given integration range $[k_0\sqrt{\varepsilon'_{rmax}}\ ,\ \lambda_{max}]$ of, say, 10 to 15 half-cycles of $J_o(\lambda\xi)$. The upper boundary λ_{max} corresponds to that real maximum number λ for which $\exp(\lambda h_{max})$, originating from the hyperbolic functions with arguments u_1h_1 and u_2h_2 present in the integrand, does not result in exponential overflow on the computer, h_{max} being the maximum substrate height. The fact that for $0 \le \xi \le \xi_{min}$ the Green's functions are not calculated is of no great importance since the singularity at $\xi = 0$ is adequately removed, as was shown in the previous sections.

A crucial point concerning the calculation of the integrals which should be observed carefully, is that the integration interval must always lie on the proper sheet of the k_ρ-plane, as outlined in section 2.9. In practical

computations this comes down to taking the correct root for the complex root functions $k_{z0}(\lambda)$ or $u_0(\lambda)$, which must result in

$$k_{z0} = + (k_0^2 - \lambda^2)^{1/2} \quad \rightarrow \quad u_0 = + j(k_0^2 - \lambda^2)^{1/2} \text{ for } \lambda \leq k_0 \qquad (3.23a)$$

and

$$k_{z0} = - j(\lambda^2 - k_0^2)^{1/2} \quad \rightarrow \quad u_0 = + (\lambda^2 - k_0^2)^{1/2} \text{ for } \lambda \geq k_0 \qquad (3.23b)$$

since the radiation condition (2.39) must be satisfied.

A final point of discussion in this section is the calculation of the surface-wave pole or the zero of the complex transcendental equation $D_{TM}(k_\rho) = 0$. If the pole is not found accurately enough, it is clear that the integrand, after extracting the singularity, is still singular at the *exact* pole location, so that this "regular" function $F_{reg}(\lambda)$, still exhibits strong variations near the exact pole. A very accurate routine should thus be used for calculating the root of D_{TM}. Separating $D_{TM}(k_\rho) = 0$ according to $\mathrm{Re}\{D_{TM}(\lambda,\nu)\} = 0$ and $\mathrm{Im}\{D_{TM}(\lambda,\nu)\} = 0$, an accurate routine for finding the zero of a system of *non-linear* equations in a number of variables can be used, such as for instance a modified Powell-hybrid method in double machine precision [33].

3.3 Numerical interpolation of the Green's functions

A numerical process which will considerably reduce the overall computation time, is that of using an interpolation routine to calculate the Green's functions from a set of precomputed values [9][12].

In the process of computing the matrix-elements $c_{ki,lj}$ and the excitation elements b_{ki}, a value of a particular Green's function is needed for all integration points, and if this Green's function is then calculated from its integral representation every time an integrand value is required by some integration routine, this process becomes extremely inefficient and time-consuming. But, since the spatial variation of all Green's functions,

for a given microstrip structure, only depends on the variable ξ, i.e., the source-observer distance, it is possible to calculate them beforehand for a set of discrete points in a given range $[\xi_{min}, \xi_{max}]$ and store these values in interpolating tables, and then to interpolate between them whenever the value of a particular Green's function for some ξ is required in the evaluation of $c_{ki,lj}$ and b_{ki}.

Since the Green's functions exhibit a spatial variation somewhat similar to ξ^{-1}, a quadratic distribution of interpolation points [9]

$$\xi_i = \frac{(\xi_{max} - \xi_{min})}{(N^2 - 1)} (i^2 - 1) + \xi_{min} \quad , \quad i = 1, \cdots, N \tag{3.24}$$

with more interpolation points close to the singularity $\xi = 0$, is a choice well suited to this situation. The lower boundary ξ_{min} for the range of interpolation points is determined by the minimum value ξ for which the Green's functions can be calculated, see section 3.2, and the upper boundary ξ_{max} is determined by the maximum source-observer distance ξ, for given patch sizes and offset, needed for calculating $c_{ki,lj}$, see section 3.1.

The interpolation scheme used for a value ξ between ξ_i and ξ_{i+1} is that of calculating an approximation for $G(\xi)$ from a third-order interpolation polynomial $p(\xi)$ through the points $[\xi_{i-1}, G(\xi_{i-1})]$, $[\xi_i, G(\xi_i)]$, $[\xi_{i+1}, G(\xi_{i+1})]$ and $[\xi_{i+2}, G(\xi_{i+2})]$ using Newton's divided difference interpolation formula [24]:

$$p(\xi) = G(\xi_{i-1}) + (\xi - \xi_{i-1}) G[\xi_{i-1}, \xi_i] + (\xi - \xi_{i-1})(\xi - \xi_i) G[\xi_{i-1}, \xi_i, \xi_{i+1}]$$

$$+ (\xi - \xi_{i-1})(\xi - \xi_i)(\xi - \xi_{i+1}) G[\xi_{i-1}, \xi_i, \xi_{i+1}, \xi_{i+2}] \tag{3.25}$$

valid for arbitrarily spaced interpolation points. The first, second and third divided differences are given by

$$G[\xi_{i-1},\xi_i] = \frac{G(\xi_i) - G(\xi_{i-1})}{\xi_i - \xi_{i-1}}$$

$$G[\xi_{i-1},\xi_i,\xi_{i+1}] = \frac{G[\xi_i,\xi_{i+1}] - G[\xi_{i-1},\xi_i]}{\xi_{i+1} - \xi_{i-1}} \qquad (3.26)$$

$$G[\xi_{i-1},\xi_i,\xi_{i+1},\xi_{i+2}] = \frac{G[\xi_i,\xi_{i+1},\xi_{i+2}] - G[\xi_{i-1},\xi_i,\xi_{i+1}]}{\xi_{i+2} - \xi_{i-1}}$$

respectively. For points lying in the end-intervals $[\xi_{min} = \xi_1, \xi_2]$ and $[\xi_{N-1}, \xi_N = \xi_{max}]$ expression (3.25) can still be used with i = 2 and i = N-2, respectively.

With regard to the number of interpolation points N, it has been shown that the accuracy with which the matrix- and excitation-elements are calculated strongly depends on N [9]. More interpolation points increases the accuracy, which is obvious because the deviation between the actual function and its approximation becomes smaller, but it also increases the time needed for calculating all Green's functions for all interpolation points (3.24), and since there are eight Green's functions needed in the case of a stacked-patch microstrip antenna and three for a single-patch microstrip antenna the number of interpolation points should not be to large. Therefore, accuracy and computation time have to be carefully weighed, one against the other. For our purpose N = 125 has shown to be a good compromise.

4 RESULTS

The design of an actual stacked microstrip antenna which meets certain requirements, such as for instance one which possibly can be used in the microstrip phased array antenna mentioned in the introduction, necessarily has to be based on a more or less "trial and error" approach, analyzing a given antenna configuration using the rigorous analysis presented in this report. This is because, compared to a conventional single-layer/single-patch microstrip antenna, the addition of an extra dielectric layer and a second microstrip patch, and also the possible displacement between the two patches, more than doubles the degrees of freedom in the design. The difficulty is that one cannot predict the influence of the various microstrip parameters on the characteristics of stacked microstrip antennas, for instance by simply considering them as two individual single-layer microstrip antennas placed on top of each other. The electromagnetic coupling between the two patches, the presence of two, possibly different, substrate layers and particularly the effect of the upper parasitic microstrip patch do not lend themselves to any quantitative speculations with respect to the characteristics of stacked microstrip antennas with varying design parameters, which obviously is the reason for conducting the present research.

In this chapter some results are presented which are mainly focused on one particular stacked-patch configuration and variation of only a few of the microstrip parameters. These results are primarily aimed at giving some insight into the frequency- and impedance-behaviour of stacked rectangular microstrip antennas, and to this end the characteristics of the antenna will be presented graphically in four forms as a function of the frequency, namely the determinant of the "method-of-moments" matrix for identifying any resonances of the structure, the input-impedance obviously for investigating their impedance behaviour, the voltage-standing-wave-ratio (VSWR) and the impedance values plotted in a Smith-chart for studying their bandwidth and matching abilities.

The numerical software which has been developed for analyzing stacked rectangular microstrip antennas based on the previous analysis has been thoroughly tested, and a good agreement has been observed with both theoretical and experimental results presented in [3][7][8] for the dual

rectangular stacked antenna and in [34] for a single-patch microstrip antenna, with and without dielectric cover. The latter two are special cases of the stacked-patch configuration and can thus easily be analyzed using the same method.

4.1 Comparison with single-patch microstrip antennas

At first, it would be most interesting to investigate whether stacked microstrip antennas are indeed capable of achieving a broader bandwidth compared to single-patch microstrip antennas. For making a comparison, examples of both types of microstrip antennas are considered having the same total substrate height, permittivities and patch sizes and shapes, and in the case of the stacked microstrip structure with the upper and lower patch being exactly aligned (no offet).

With regard to the shape of the microstrip patches the choice has been made in favor of square patches with the coaxial feed situated halfway between two edges (center-fed) of the lower patch to which it is connected, and also halfway relative to the edges of the upper patch. This is done, because it allows the microstrip antenna to be capable of creating circular polarization, using two spatially orthogonal coaxial feeds which are excited with a relative phase shift of $\pm 90^{\circ}$, each of them thus exciting a linearly polarized wave, orthogonal in space, and being in time phase quadrature [19]. For the analysis of the microstrip antenna with the method of moments, the fact that the patches are fed at the center between two edges means that the patch currents at resonance can be accurately described by only one current mode per patch in the resonant direction corresponding to a particular feed position, as outlined in section 2.6.

With reference to figure 2.6 for equal square patches, $a_{i,j} = b_{i,j}$ for all $i,j = 1,2$, if the x-direction is now chosen as the resonant direction with the coaxial probe at $y_c = \frac{1}{2} b_{1,2}$ and x_c chosen arbitrarily, and with no offset of the upper patch in the x- and y-direction, $x_{01} = y_{01} = 0$, then an x-directed current $\bar{J}_{si} = \hat{e}_x \sin(\pi\, x/a_i)$ is employed on both patches.

For this particular patch configuration a stacked microstrip antenna has been

analyzed with $h_1 = h_2 = 0.79$ mm., $\varepsilon'_{r1} = \varepsilon'_{r2} = 2.33$ and $\tan\delta_1 = \tan\delta_2 = 0.001$, and also for making a comparison a single-patch microstrip antenna, having a substrate height h = 1.58 mm. and the same dielectric properties. In both cases square patches having dimensions 60 x 60 mm. are used in the analysis. For identifying the resonant behaviour of the microstrip antennas, figure 4.1 shows the modulus of the determinant of the "method-of-moments" matrix for both cases as a function of the frequency.

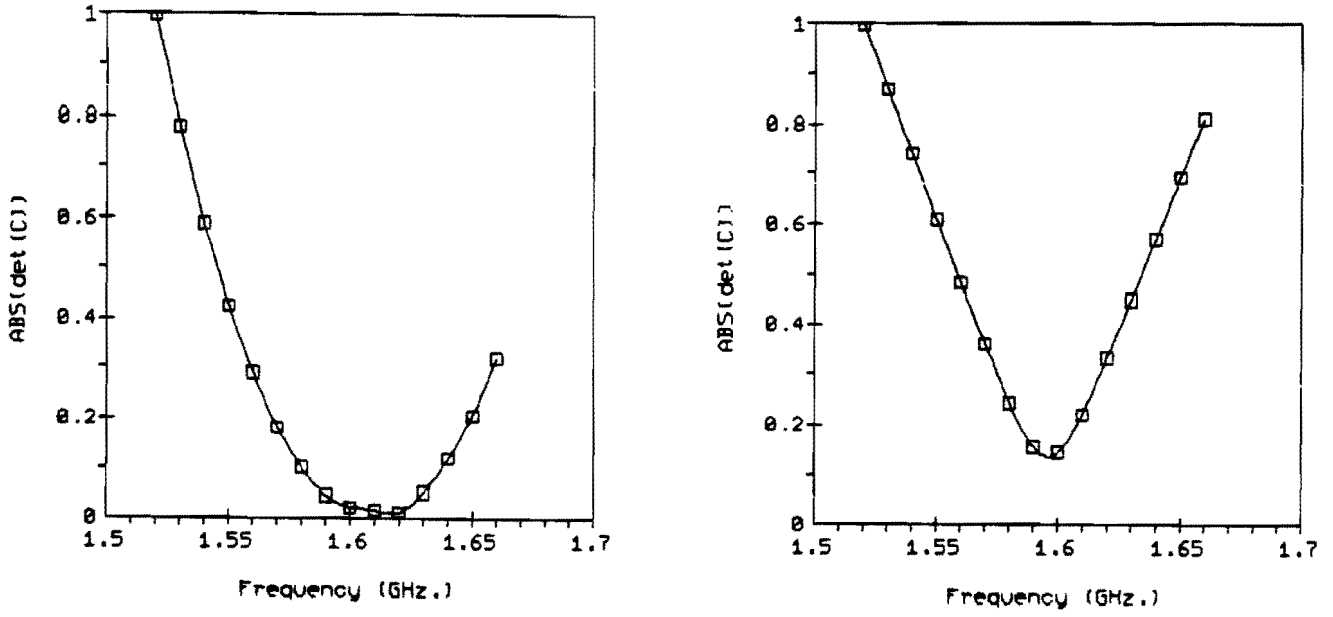

(a) (b)

Fig. 4.1 Determinant of "method-of-moments" matrix: (a) stacked microstrip antenna, $h_{1,2} = 0.79$ mm. and (b) single-patch microstrip antenna, h = 1.58 mm.

From the above figure it can be seen that the stacked microstrip antenna apparently has a broader resonance behaviour compared to the single-patch antenna. This phenomenon can be examined more closely by looking at the input-impedance, which is depicted in figure 4.2 for both the single- and double-patch microstrip antenna, and for a coaxial feed situated at ($x_c = 10$ mm., $y_c = 30$ mm.).

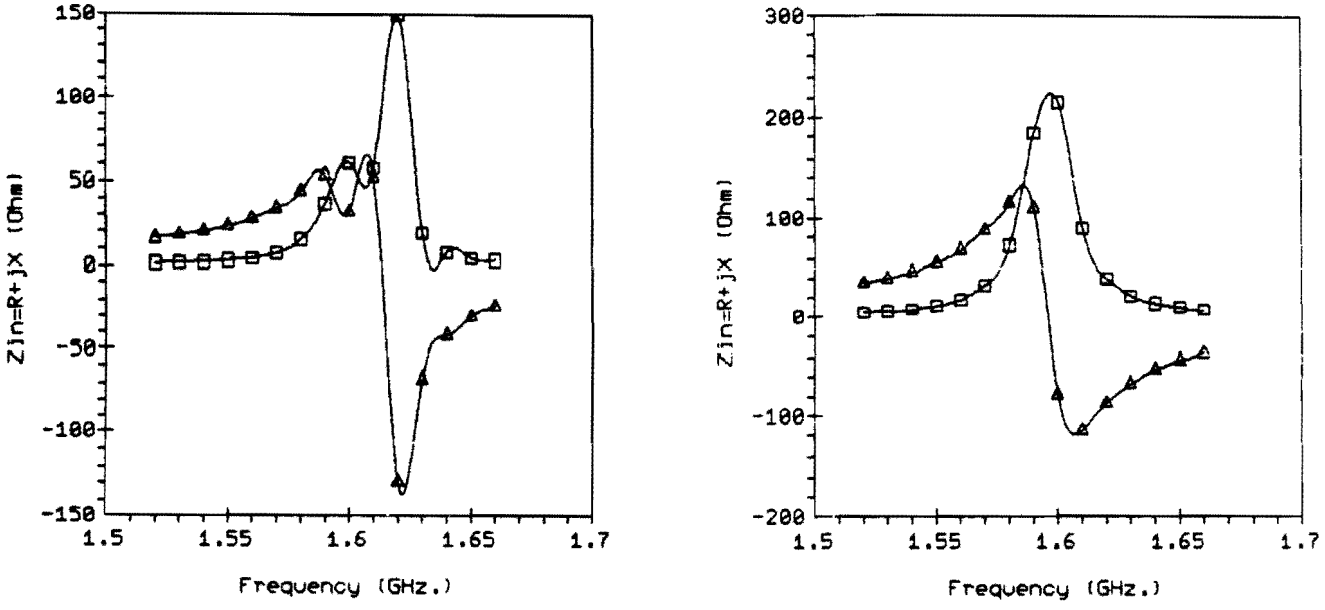

(a) (b)

Fig. 4.2 Input-impedance Z_{in}, (x_c, y_c) = (10 mm., 30 mm.): (a) stacked microstrip antenna, $h_{1,2}$ = 0.79 mm. and (b) single-patch microstrip antenna, h = 1.58 mm. □ = real part, Δ = imaginary part

Figure 4.2a reveals that the broader resonance in figure 4.1a actually originates from two very close resonances compared to the single resonance in figure 4.2b for a single-patch antenna. The upper resonance, which has the largest impedance value, has a behaviour similar to the resonance of the single-patch case, the resonant frequency being identified as that frequency for which the imaginary part of the input-impedance is zero and the real part has a maximum. The behaviour at the lower resonance is somewhat different because the imaginary part of the input-impedance does not vanish where the real part has a maximum, even though the form of the impedance curve at this resonance has the characteristic resonant behaviour, which means that the corresponding resonant frequency cannot be defined in the usual way.

The input-impedance alone as shown in figure 4.2 does not indicate whether or not stacked microstrip antennas exhibit an improved impedance-bandwidth, which is the band of frequencies for which the antenna is properly matched to the coaxial feed line. For investigating the bandwidth we look at the Voltage-Standing-Wave-Ratio (VSWR) of both microstrip antennas connected to a 50 Ohm coaxial cable, because the bandwidth requirements for microstrip

antennas are usually specified as a range of frequencies for which the VSWR is below some value, e.g., VSWR < 1.5 or VSWR < 2, so that within this range the device is properly matched to a specific feeding network. The choice for a feed line with a characteristic impedance of 50 Ω is somewhat arbitrary, but since they are the most common they will be used here for reference purposes.

The VSWR near resonance for the microstrip antennas from figure 4.2 is now shown in figure 4.3

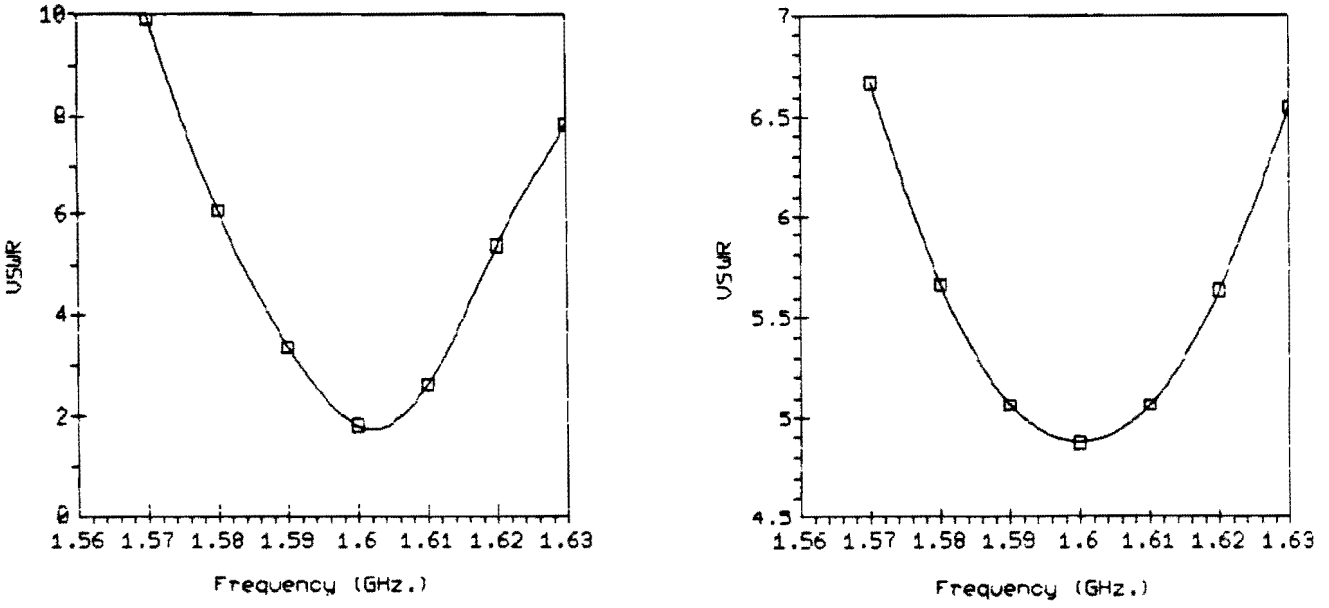

(a) (b)

Fig. 4.3 VSWR, (x_c, y_c) = (10 mm., 30 mm.): (a) stacked microstrip antenna, $h_{1,2}$ = 0.79 mm. (b) single-patch microstrip antenna, h = 1.58 mm.

Although no perfect matching (VSWR = 1) occurs at any frequency for this particular feed location, the bandwidth can still be estimated from these figures because the overall behaviour of the VSWR-curves does not change significantly if the feed is shifted towards the center of the patch; this only results in a reduction of all impedance values. If both antennas would be perfectly matched to the coaxial feed at the frequency where the VSWR-curve shows a minimum, the stacked microstrip antenna would have a bandwidth less than 1% of the minimum-VSWR frequency, which is about the same as that for the single-patch microstrip antenna. This can be understood

because, even though the stacked-patch configuration exhibits two close resonances, the impedance values at these resonances differ approximately a factor 2.5, and the bandwidth at both resonances is as small as that of the single resonance for the single-patch microstrip antenna. So, for the above stacked microstrip antenna no improvement in bandwidth is achieved.

It is instructive to plot the impedance values in a Smith-chart because this helps investigating the matching characteristics of the microstrip antenna as well as finding possible ways of increasing the impedance-bandwidth. For the two situations of figures 4.2-4.3 the impedance locus in the Smith-chart is shown in figure 4.4.

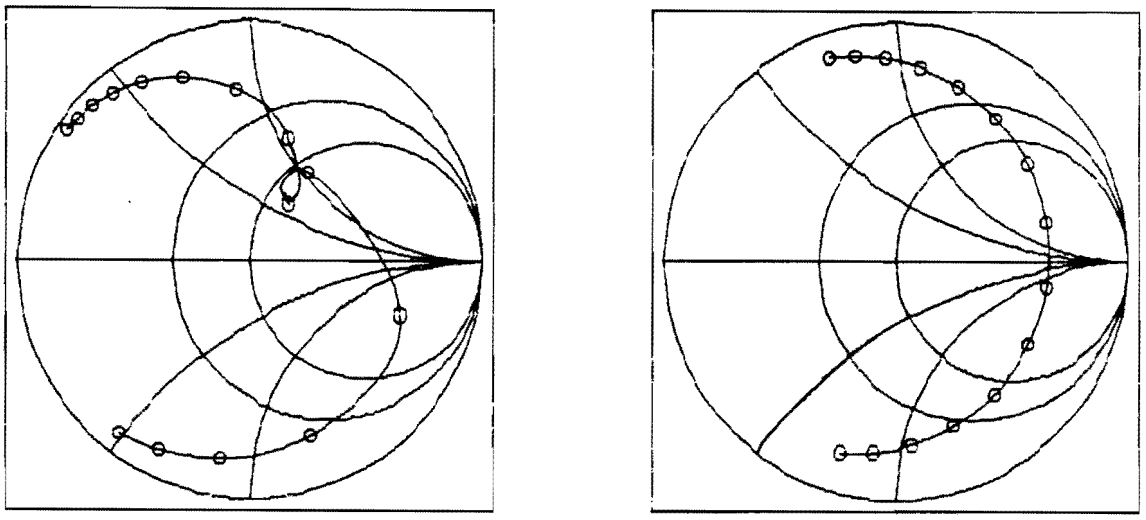

(a) (b)

Fig. 4.4 Impedance locus (1.52-0.01-1.66 GHz.), (x_c, y_c) = (10 mm., 30 mm.): (a) stacked microstrip antennna, $h_{1,2}$ = 0.79 mm. (b) single-patch microstrip antenna, h =1.58 mm.

Figure 4.4b shows the well-known impedance locus for single-patch microstrip antennas, namely a circle-like curve passing through the zero-imaginary-impedance line in the Smith-chart at the resonant frequency. The introduction of a second microstrip patch then obviously results in the appearance of a small loop in the impedance-curve at the lower resonance, as can be seen in figure 4.4a. This also explains why there is practically no increase in bandwidth compared to the single-patch case, because this loop at the lower

resonance is very small and it covers only a relatively small frequency band.

The above Smith-chart indicates however a possible design objective for increasing the bandwidth and the impedance matching, which is to create a stacked microstrip antenna having a larger loop in the impedance-curve which at he same time covers a larger frequency band and if possible is also located around the 50 Ω point on the Smith-chart for VSWR values less than some specified value.

Increasing the bandwidth for the conventional single-layer/single-patch microstrip antenna can be achieved by increasing the thickness of the substrate layer. To investigate the effect of an increase in substrate height, again two cases are compared, namely a stacked microstrip antenna with the same patch geometry and dielectric properties as above but with substrate thicknesses $h_1 = h_2 = 1.57$ mm., and a single-patch microstrip antenna with a total substrate height h = 3.14 mm. The resonant behaviour can again be observed from the determinant of the "method-of-moments" matrix (Fig. 4.5), which in this case indeed shows a broader resonance for both microstrip antennas compared to figure 4.1.

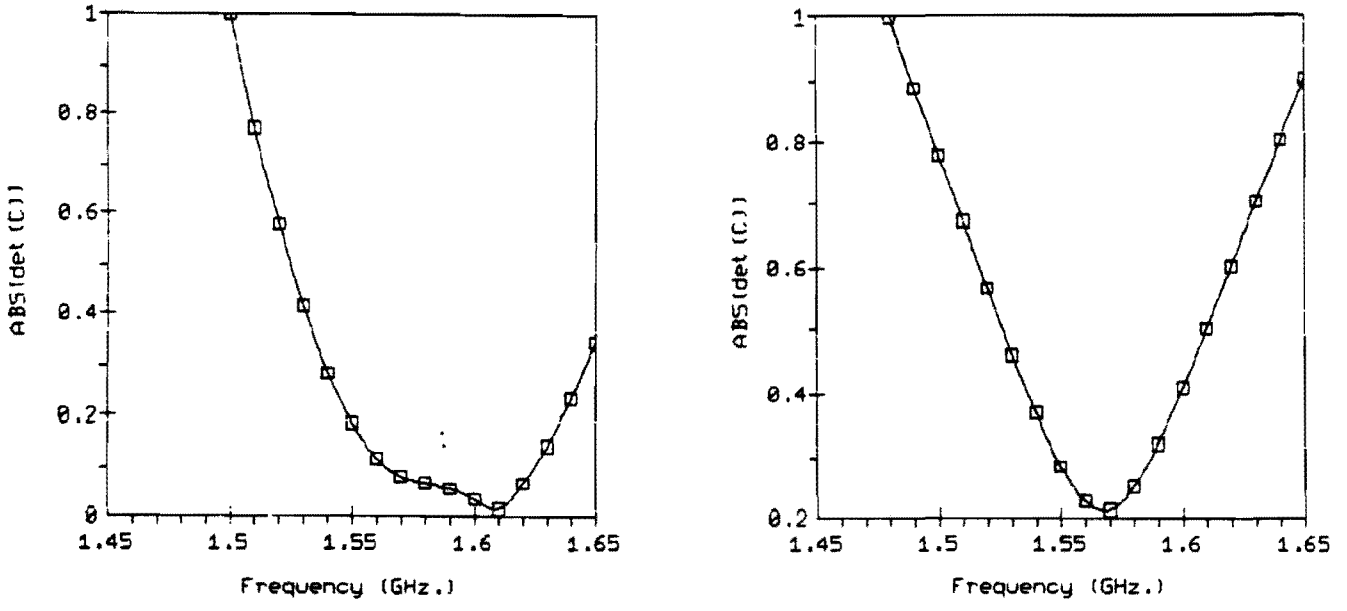

(a) (b)

Fig. 4.5 Determinant of "method-of-moments" matrix: (a) stacked microstrip antenna, $h_{1,2} = 1.57$ mm. and (b) single-patch microstrip antenna, h = 3.14 mm.

The input-impedance for both cases is shown in figure 4.6 for a coaxial feed situated at (x_c, y_c) = (15 mm., 30 mm.). Compared to the first case, figure 4.2, increasing the substrate thickness does not seem to have any noticeable effect on the upper resonance whereas the lower resonance now shows a significant broadening of the impedance-curve.

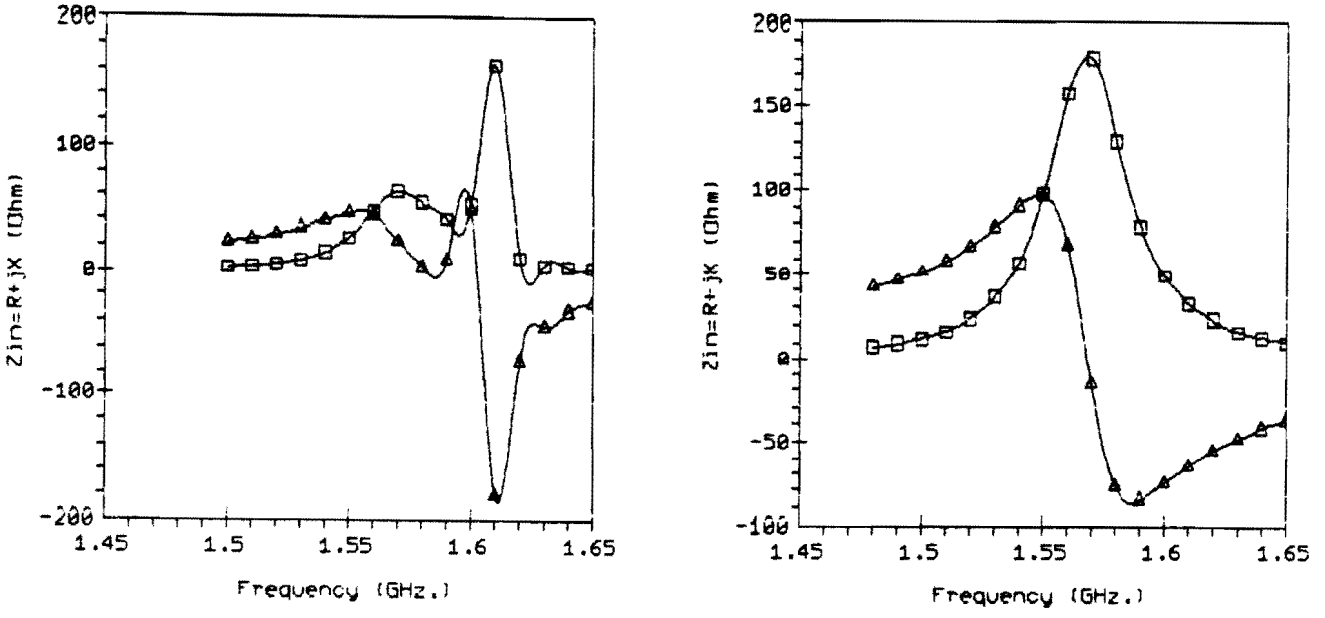

(a) (b)

Fig. 4.6 Input-impedance Z_{in}, (x_c, y_c) = (15 mm., 30 mm.): (a) stacked microstrip antenna, $h_{1,2}$ = 1.57 mm. and (b) single-patch microstrip antenna, h = 3.14 mm.

But, the resonance for the single-patch case too shows a broader resonance, compared to figure 4.2b, which is to be expected. To examine more closely the effect of thicker substrate layers on the impedance-bandwidth and for comparing the single- and double-patch microstrip structures in this case, the VSWR-curves corresponding to figure 4.6 are shown in figure 4.7. These figures reveal that a larger bandwidth can indeed be obtained with thicker substrate layers, but that no improvement in bandwidth is observed for the stacked microstrip antenna compared to the single-patch case. In fact, the bandwidth for the stacked patches even appears to be slightly less compared with that of the single-patch case.

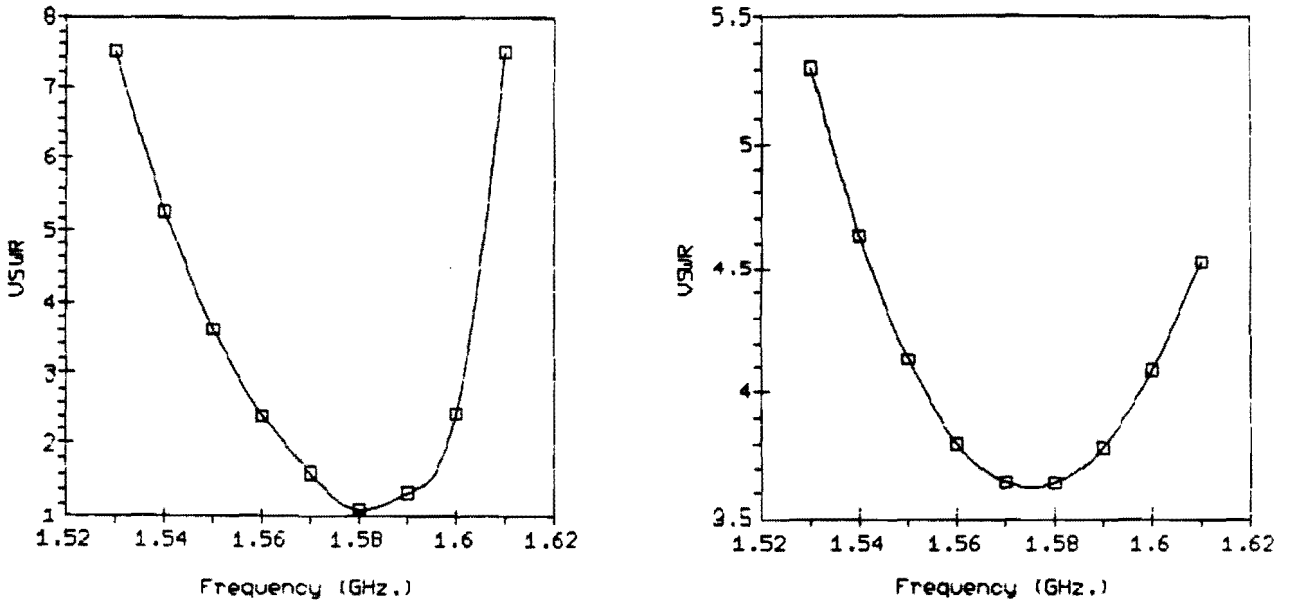

(a) (b)

Fig. 4.7 VSWR, (x_c, y_c) = (15 mm., 30 mm.): (a) stacked microstrip antenna, $h_{1,2}$ = 1.57 mm. (b) single-patch microstrip antenna, h = 3.14 mm.

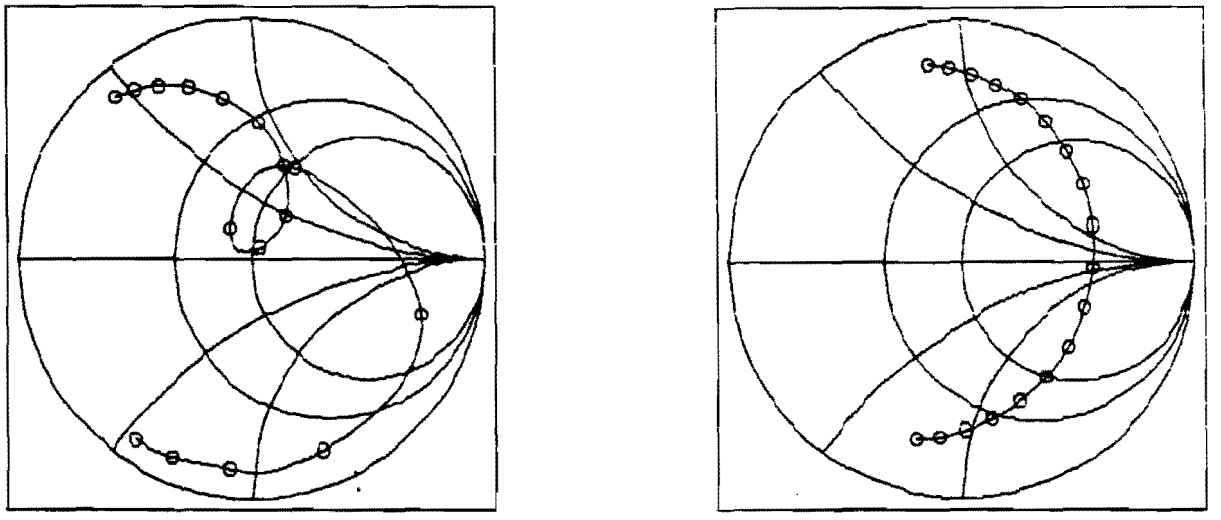

(a) (b)

Fig. 4.8 Impedance locus (1.52-0.01-1.66 GHz.), (x_c, y_c) = (15 mm., 30 mm.): (a) stacked microstrip antennna, $h_{1,2}$ = 1.57 mm., (b) single-patch microstrip antenna, h = 3.14 mm.

The impedance locus in the Smith-chart for the single-patch microstrip antenna with h = 3.14 mm. (Fig. 4.8b) is similar to that with h = 1.58 mm. (Fig. 4.4b), only with a larger concentration of frequencies around the resonance, indicating a larger bandwidth. The differences in the impedance locus with varying substrate thickness for the stacked microstrip configuration are more significant (Figs. 4.4a and 4.8a), namely an enlargement in the impedance-loop which also covers a larger frequency band, but this improvement apparently is still not sufficient for achieving a definite enhancement of the impedance-bandwidth compared to single-patch microstrip antennas.

The examples presented above indicate that for two equal stacked patches with their edges exactly aligned, no improvement in bandwidth is observed compared to a single-patch microstrip antenna, the latter having a substrate thickness equal to the total substrate height of the stacked-patch configuration. For a fixed substrate height, different stacked microstrip geometries may have an effect on the impedance-bandwidth, and some of the effects of using either patches of different sizes or introducing an offset between the two patches shall be presented in the next sections.

As two final examples in this section, two stacked rectangular microstrip antennas have been analyzed for the same patch geometry as above, but with a further increase in total substrate height. The first one incorporates different substrate heights, namely h_1 = 3.18 mm. and h_2 = 1.57 mm., and the same dielectric properties: $\varepsilon'_{r1} = \varepsilon'_{r2} = 2.33$ and $\tan\delta_1 = \tan\delta_2 = 0.001$. For four different coaxial-feed points on the center line in the x-direction between two edges , $y = \frac{1}{2}b_{1,2}$, the input-impedance-curves and the impedance-loci in the Smith-chart are given in figures 4.9-4.12.

These figures show that the shapes of the impedance curves are more or less insensitive to a change in feed position, they only shift towards lower impedance values, as was expected. Furthermore, it can be concluded that the increase in thickness of the upper substrate layer causes a further broadening of the lower resonance compared to figure 4.6a, which results in a larger frequency-band incorporated in the characteristic impedance-loop in the Smith-chart, without any significant change in the shape and size of this loop.

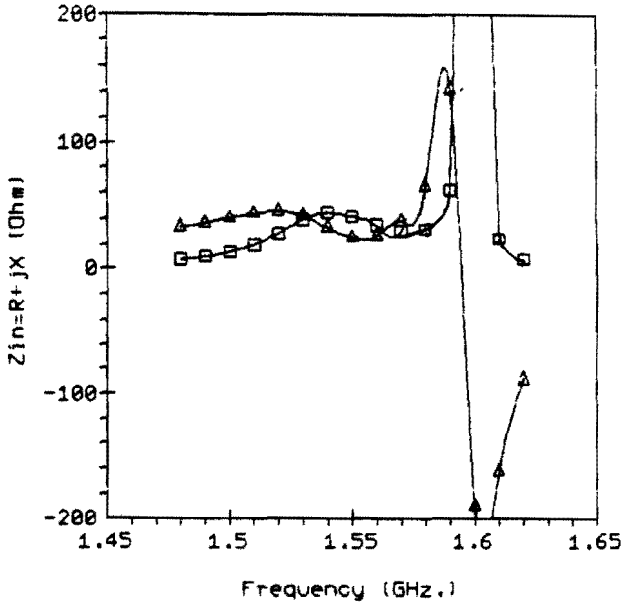

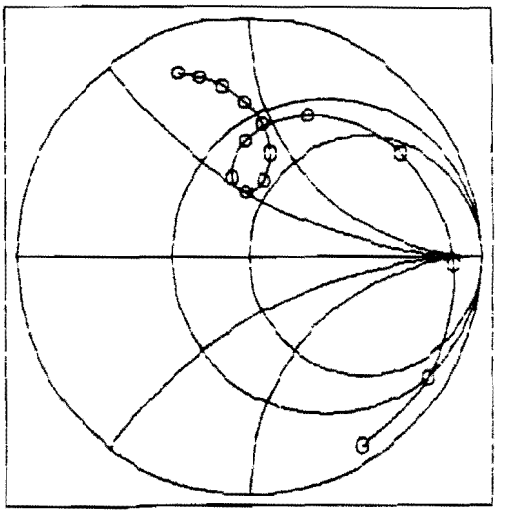

(a) (b)

Fig. 4.9 Input-impedance (a) and (b) impedance-locus (1.48-0.01-1.62 GHz.) for (x_c, y_c) = (5 mm., 30 mm.), h_1 = 3.18 mm. and h_2 = 1.57 mm.

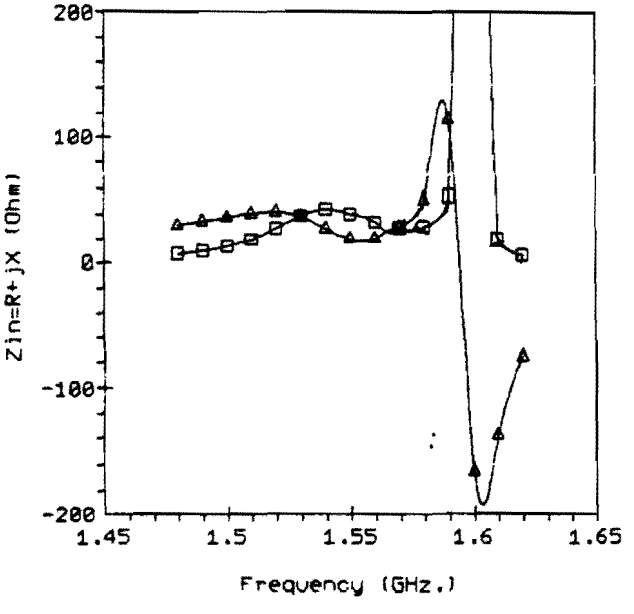

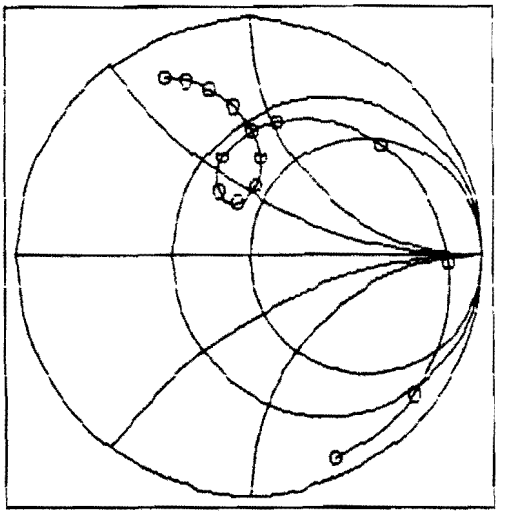

(a) (b)

Fig. 4.10 Input-impedance (a) and (b) impedance-locus (1.48-0.01-1.62 GHz.) for (x_c, y_c) = (10 mm., 30 mm.), h_1 = 3.18 mm. and h_2 = 1.57 mm.

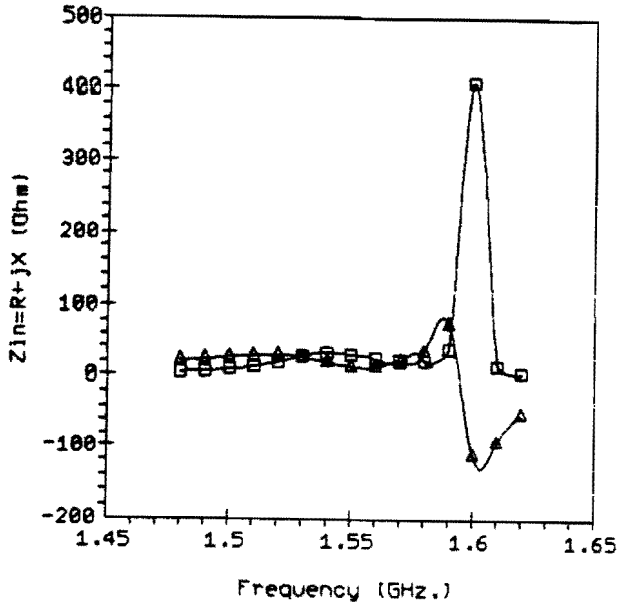

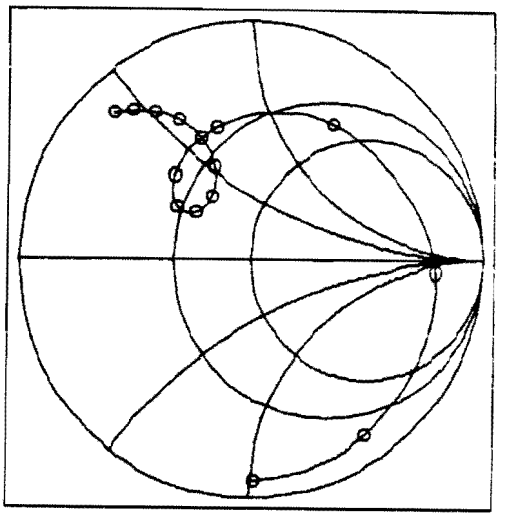

(a) (b)

Fig. 4.11 Input-impedance (a) and (b) impedance-locus (1.48-0.01-1.62 GHz.) for (x_c, y_c) = (15 mm., 30 mm.), h_1 = 3.18 mm. and h_2 = 1.57 mm.

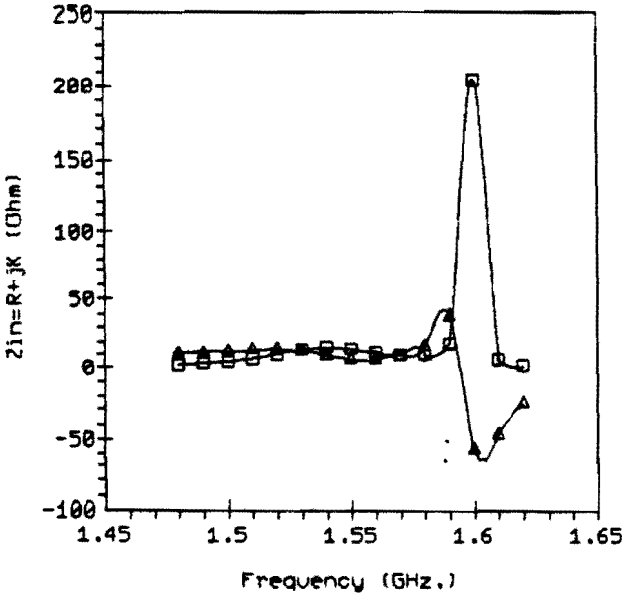

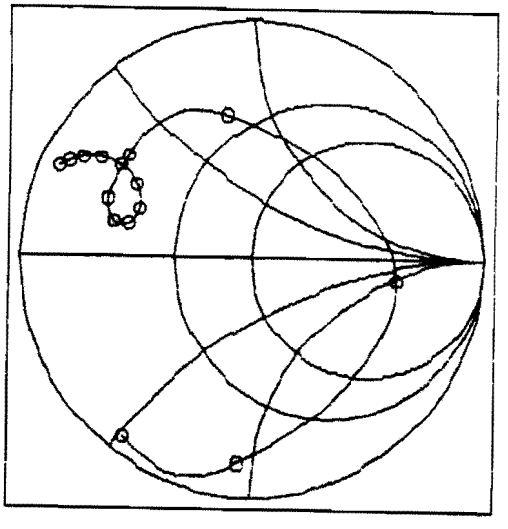

(a) (b)

Fig. 4.12 Input-impedance (a) and (b) impedance-locus (1.48-0.01-1.62 GHz.) for (x_c, y_c) = (20 mm., 30 mm.), h_1 = 3.18 mm. and h_2 = 1.57 mm.

This effect can even further be enhanced by also increasing the thickness of the lower substrate layer: h_2 = 3.18 mm. For this second case several curves for different positions of the coaxial feed are depicted in figures 4.13-4.15.

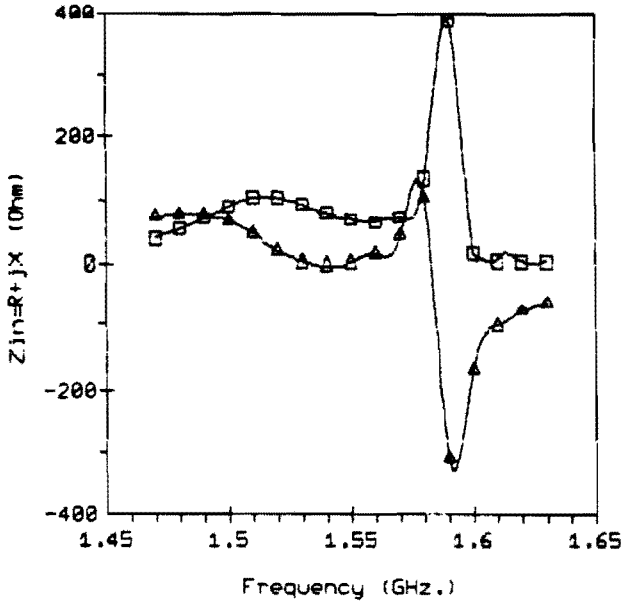

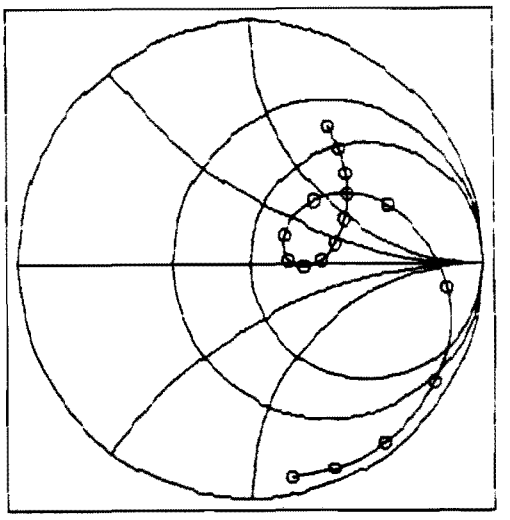

(a) (b)

Fig. 4.13 Input-impedance (a) and (b) impedance-locus (1.47-0.01-1.63 GHz.) for (x_c, y_c) = (10 mm., 30 mm.), h_1 = 3.18 mm. and h_2 = 3.18 mm.

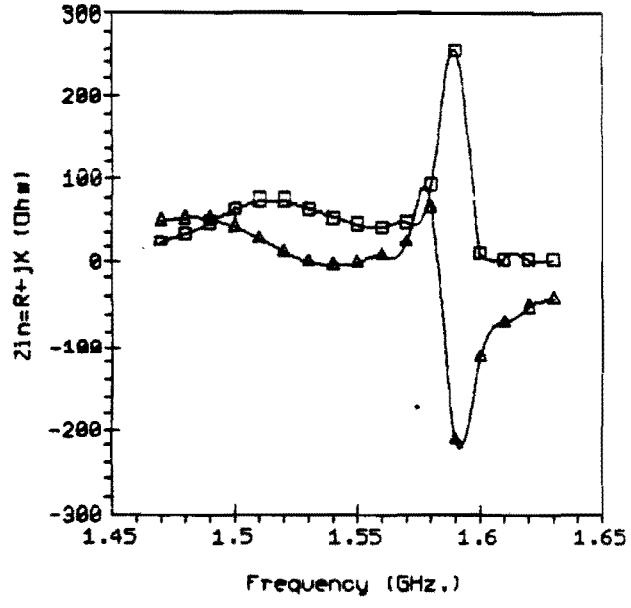

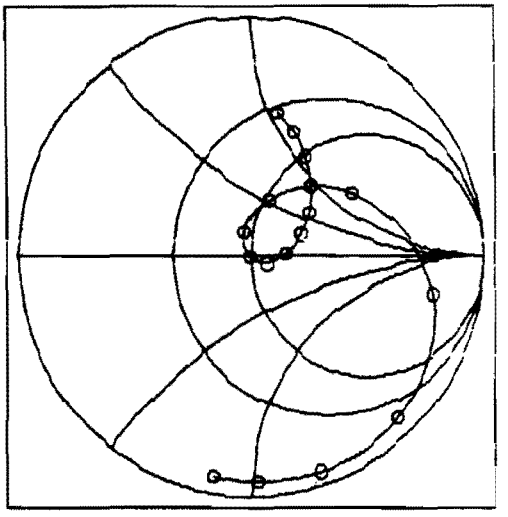

(a) (b)

Fig. 4.14 Input-impedance (a) and (b) impedance-locus (1.47-0.01-1.63 GHz.) for (x_c, y_c) = (15 mm., 30 mm.), h_1 = 3.18 mm. and h_2 = 3.18 mm.

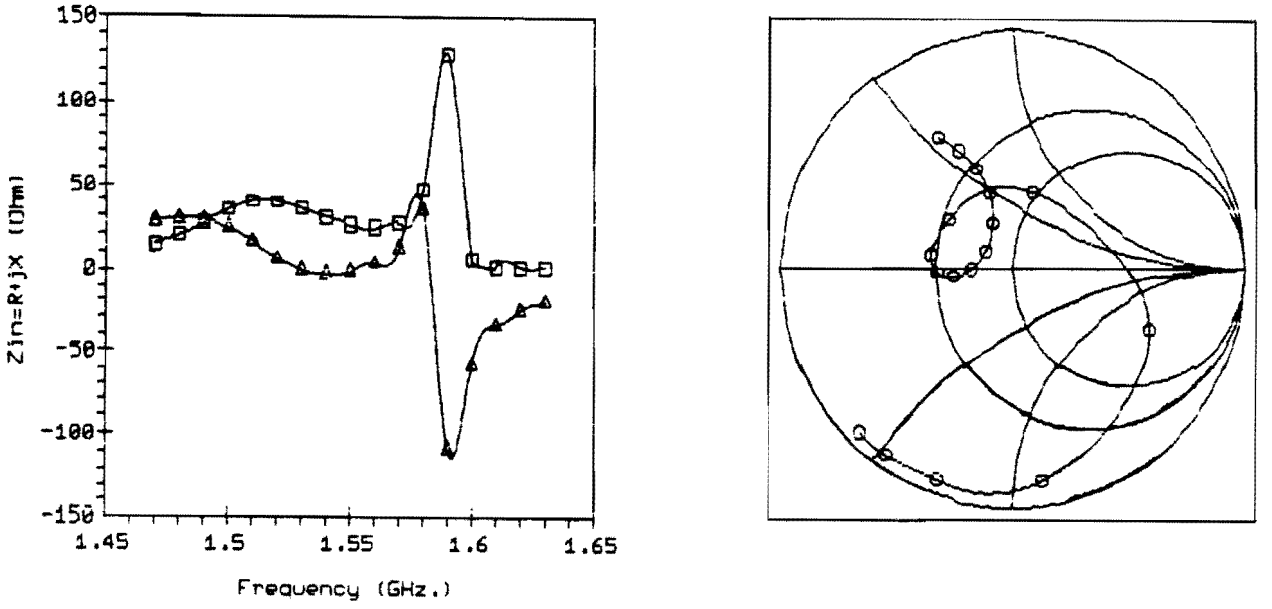

(a) (b)

Fig. 4.15 Input-impedance (a) and (b) impedance-locus (1.47-0.01-1.63 GHz.) for (x_c, y_c) = (20 mm., 30 mm.), h_1 = 3.18 mm. and h_2 = 3.18 mm.

Especially the second case, (x_c, y_x) = (15 mm., 30 mm.), shows a good impedance match to the coaxial feed at the lower resonance. The bandwidth for a VSWR < 1.5 is approximately 50 MHz. (≈ 3.2% of 1.55 GHz.) and for VSWR < 2 only slightly larger, namely approximately 70 MHz. (≈ 4.5% of 1.55GHz.). But, with reference to the first two examples of this section, this bandwidth will not differ much from from a single-patch microstrip antenna with the same total substrate height (h = 6.36 mm.). Furthermore, the use of such thick substrate layers has a great disadvantage, namely an increased excitation of the dominant TM_0-surface-wave-mode which is always present in the microstrip structure. Especially when the stacked microstrip element is used in an array, surface waves will strongly effect the array properties, because of the mutual coupling between the patches.

4.2 Displacement of the upper microstrip patch

The results presented in the previous section where aimed at determining the effect of the substrate thickness on the antenna characteristics, and a fixed microstrip-patch-geometry was investigated while varying the height of the dielectric layers. Since no noticeable enhancement of the impedance-bandwidth was observed this way, the effect of another parameter in the design of stacked microstrip antennas, namely the offset between the upper and lower patch will be examined in this section.

The influence of a shift in the upper patch with respect to the lower patch is investigated for stacked microstrip antennas with fixed equal substrate layers having a thickness $h_1 = h_2 = 1.57$ mm., dielectric constant $\varepsilon'_{r1} = \varepsilon'_{r2} = 2.33$ and loss-tangent $\tan\delta_1 = \tan\delta_2 = 0.001$. Again, the microstrip patches are equal size square patches, 60×60 mm., but here the upper patch will be shifted in the x-direction, and will have no offset in the y-direction, $y_{o1} = 0$. The choice for a shift in only the x-direction has been made because if the patch configuration is again center-fed in the y-direction on the lower patch, $y_c = \frac{1}{2}b_2$, the feed is also centered in the y-direction with respect to the upper patch, $y_c = \frac{1}{2}b_1$, so that only one current mode per patch in the resonant x-direction can be used in the analysis for accurately representing the patch currents, namely $\bar{J}_{s2} = \hat{e}_x \sin(\pi\, x/a_2)$ on the lower patch and $\bar{J}_{s1} = \hat{e}_x \sin(\pi\, (x-x_{o1})/a_1)$ on the upper patch.

First, it is interesting to examine the resonant behaviour of the microstrip antenna for various offsets in the x-direction, $x_{o1} = -1$, 1, 2 and 5 mm., by looking at the determinant of the "method-of-moments" matrix (Fig 4.16)

Compared to figure 4.5a (no offset) a broadening of the resonance curves is observed from these figures. This effect is only minimal for the offsets $x_{o1} = -1$ mm. and $x_{o1} = 1$ mm., but for a further displacement between the upper and the lower patch, $x_{o1} = 2$ mm. and $x_{o1} = 5$ mm., two clearly distinguishable resonances are visible. This indicates that the shift in the upper patch causes the two resonances, which are still very close together in figures 4.16a/b, to separate for an increasing offset x_{o1}.

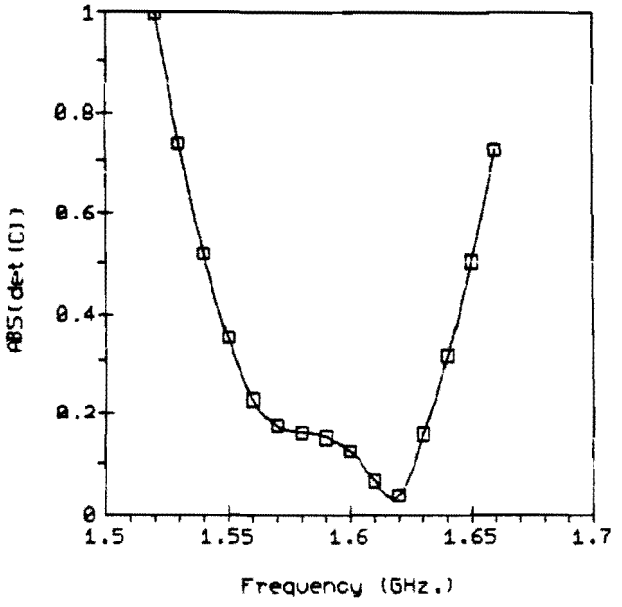

(a)

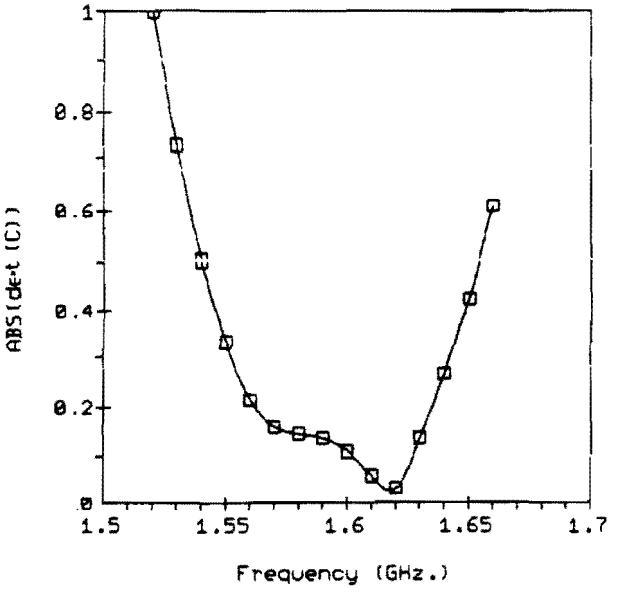

(b)

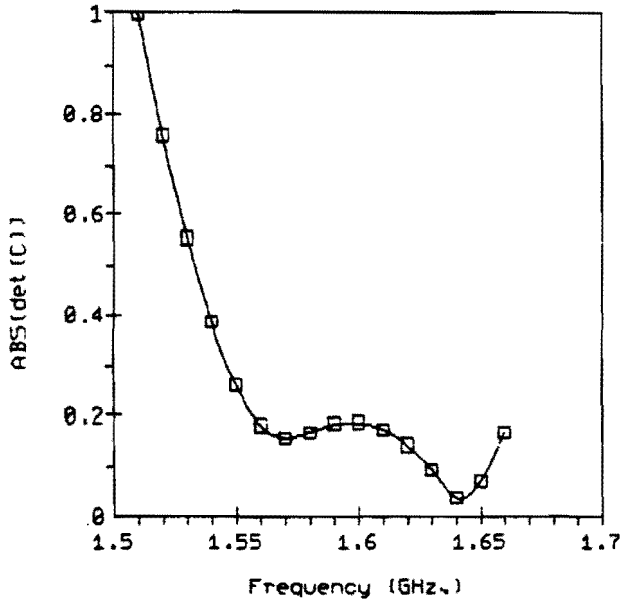

(c)

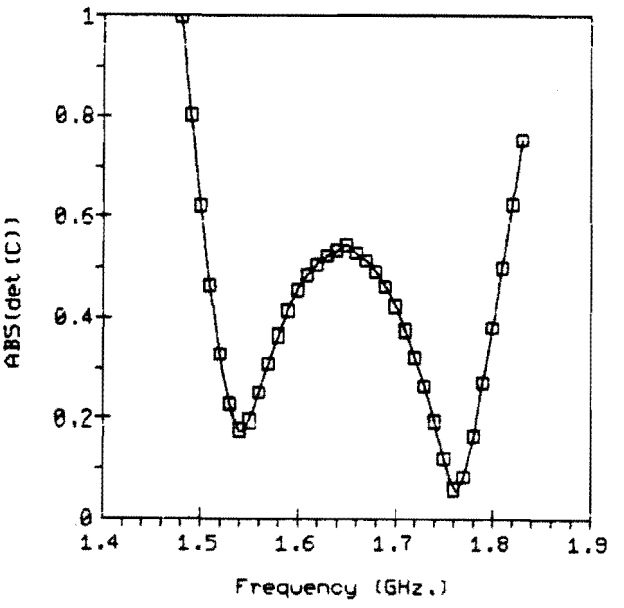

(d)

Fig. 4.16 Determinant of the "method-of-moments" matrix for an offset patch geometry: (a) x_{o1} = -1 mm. (b) x_{o1} = 1 mm. (c) x_{o1} = 2 mm. (d) x_{o1} = 5 mm.

This effect of the separation of the resonances can also be observed from the

input-impedance curves for a coaxial feed at (x_c, y_c) = (5 mm., 30 mm.), depicted below.

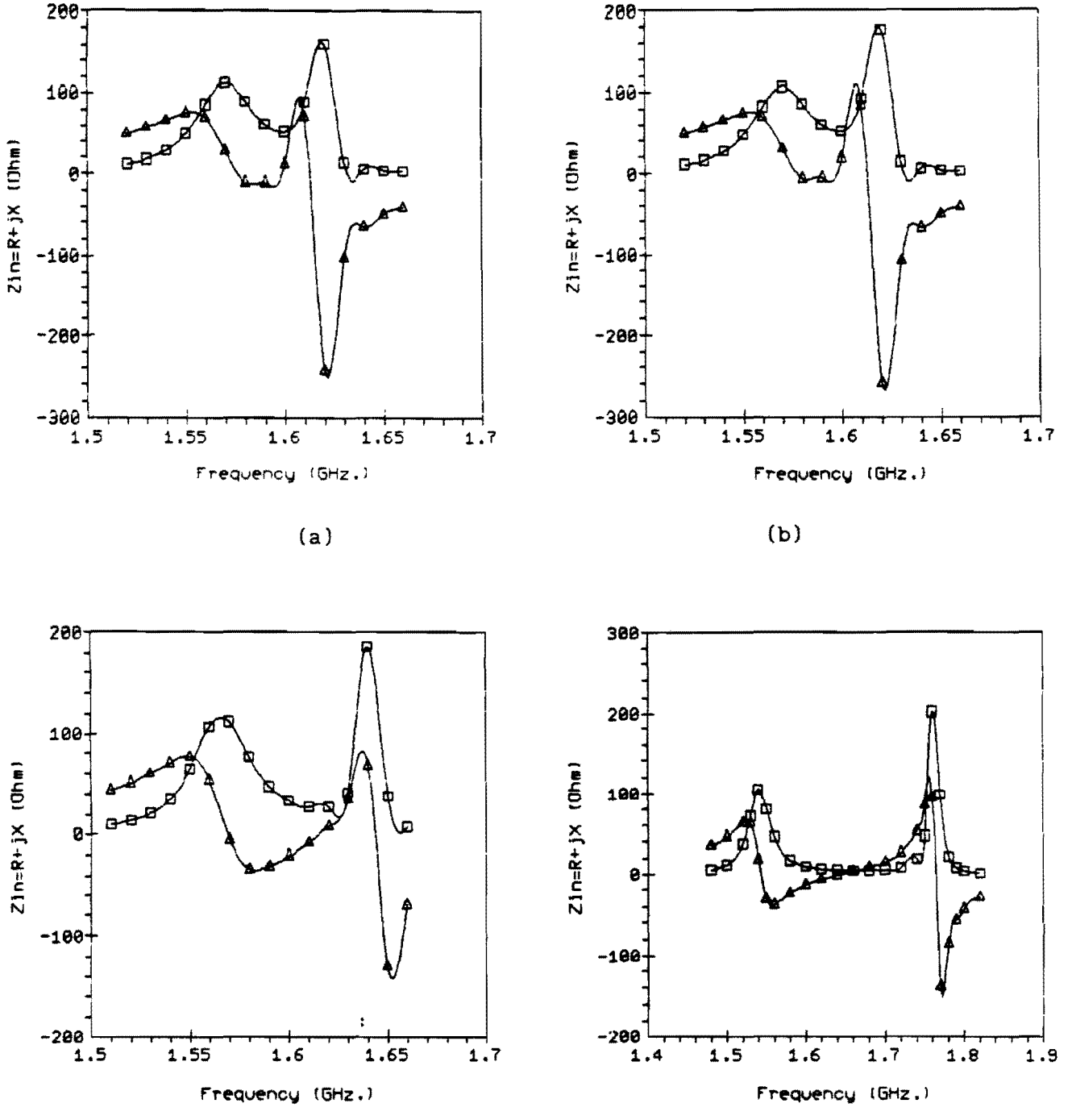

Fig. 4.17 Input-impedance for offset patch geometry, (x_c, y_c) = (5 mm., 30 mm.): (a) x_{o1} = -1 mm. (b) x_{o1} = 1 mm. (c) x_{o1} = 2 mm. (d) x_{o1} = 5 mm.

These impedance-curves clearly show two resonances, the degree of separation between them depending on the particular offset, and with a relatively broad lower resonance and narrow upper resonance. These figures further reveal that there is hardly any difference between a positive and a negative shift in the upper patch, x_{o1} = +1 mm. and x_{o1} = -1 mm., which can also be observed from figure 4.16. Apparently, the patch currents for such small shifts in either direction are equally perturbed, and subsequently also the input-impedance. Another interesting feature which can be observed from figure 4.17 is that the difference in impedance values at the two resonances is much less than that in the case without offset (Fig. 4.6a)

The bandwidth of these types of offset-stacked microstrip antennas and possible matching abilities are investigated from the VSWR-curve and the impedance-locus in the Smith-chart, which are presented in figures 4.18-4.20 for the case x_{o1} = 1 mm. and for three different feed points: (x_c, y_c) = (5 mm., 30 mm.), (10 mm., 30 mm.) and (15 mm., 30 mm.).

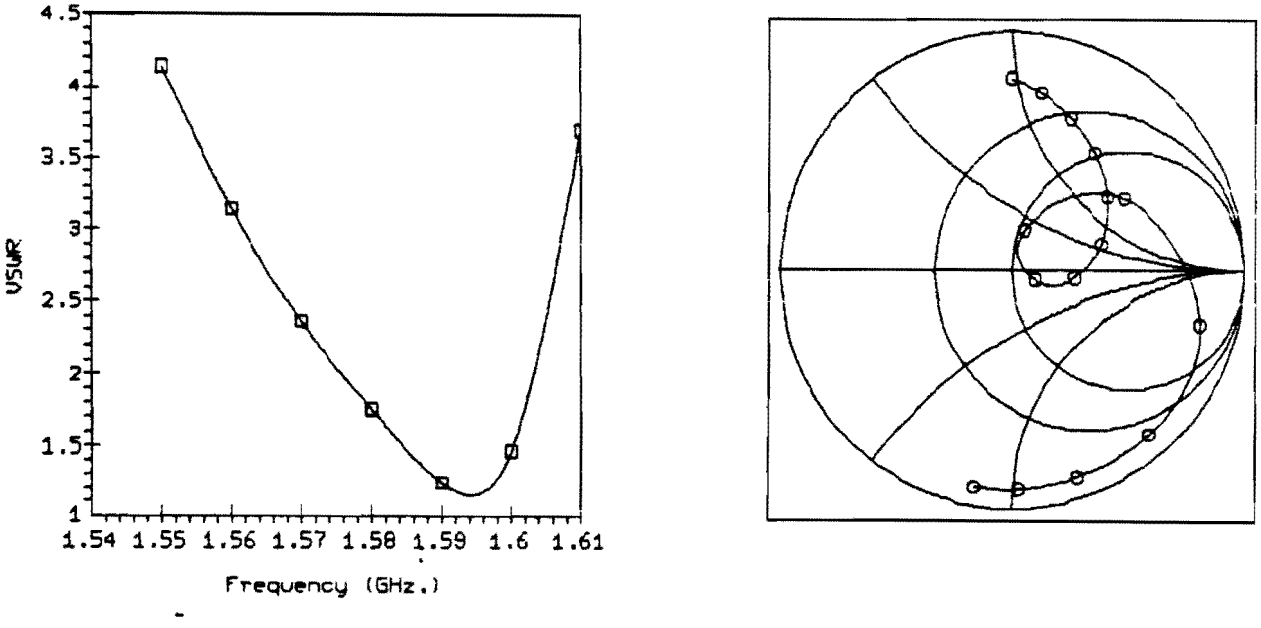

(a) (b)

Fig. 4.18 VSWR (a) and (b) impedance-locus (1.52-0.01-1.66 GHz.), x_{o1} = 1 mm., (x_c, y_c) = (5 mm., 30 mm.)

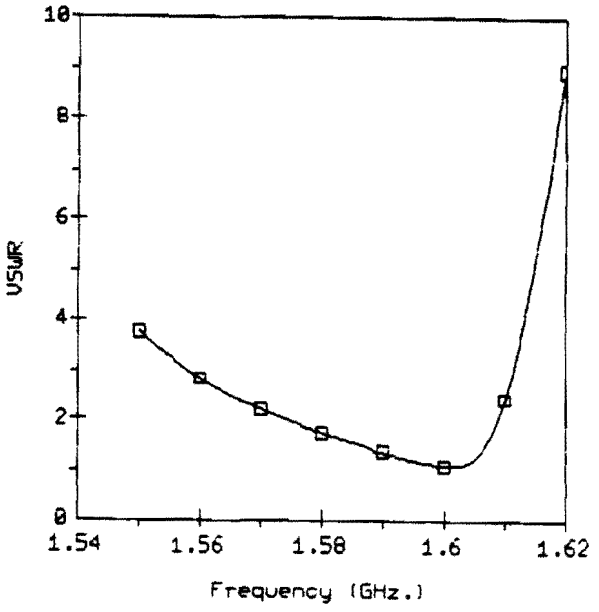

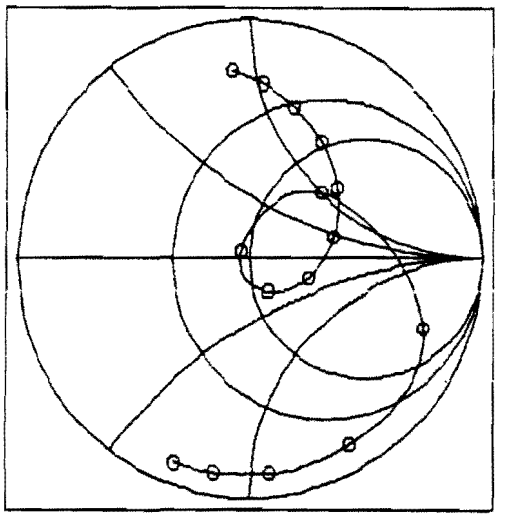

(a) (b)

Fig. 4.19 VSWR (a) and (b) impedance-locus (1.52-0.01-1.66 GHz.), x_{o1} = 1 mm., (x_c, y_c) = (10 mm., 30 mm.)

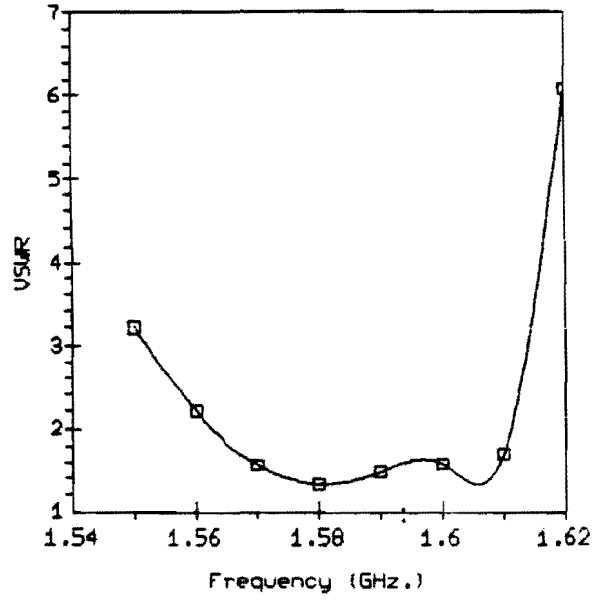

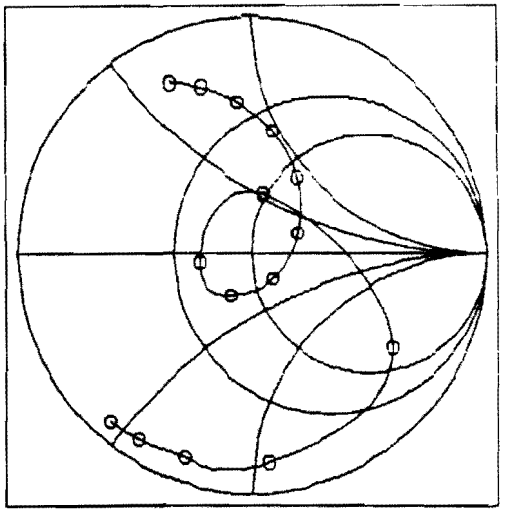

(a) (b)

Fig. 4.20 VSWR (a) and (b) impedance-locus (1.52-0.01-1.66 GHz.), x_{o1} = 1 mm., (x_c, y_c) = (15 mm., 30 mm.)

From these figures it can be observed that this displacement of the upper patch causes a definite increase in the impedance-bandwidth compared to the case without offset (Fig. 4.7a) and even compared to the single-patch case with the same substrate height (Fig. 4.7b). This is obviously due to the larger impedance-loop and the fact that this loop is situated more or less symmetrically around the 50 Ω point (VSWR = 1) on the Smith-chart through a proper choice of the position of the coaxial feed (Fig. 4.20b). For frequencies on this loop the device exhibits a rather constant VSWR of approximately 1.3-1.7 for a frequency range of 50 MHz. This enlargement of the characteristic impedance-loop, apparently inherent to stacked microstrip antennas, is extended even further for a larger displacement between the two patches, as can be seen in figures 4.21-4.22 for an offset x_{o1} = 2 mm.

Again, a relatively constant VSWR (≈ 1.9 in figure 4.21) is observed for frequencies on the impedance-loop, and over an even broader frequency band. But, even though this loop is situated symmetrically around the 50 Ω point on the Smith-chart, the impedance match has become worse due to the dimension of this impedance-loop.

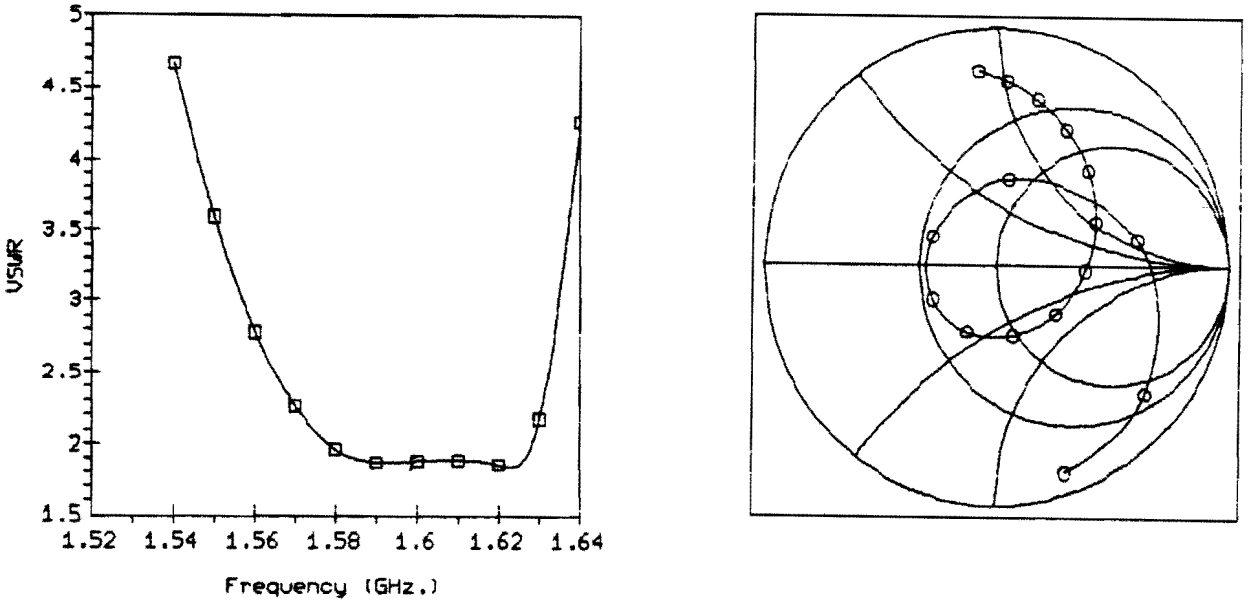

(a) (b)

Fig. 4.21 VSWR (a) and (b) impedance-locus (1.51-0.01-1.66 GHz.), x_{o1} = 2 mm., (x_c, y_c) = (5 mm., 30 mm.)

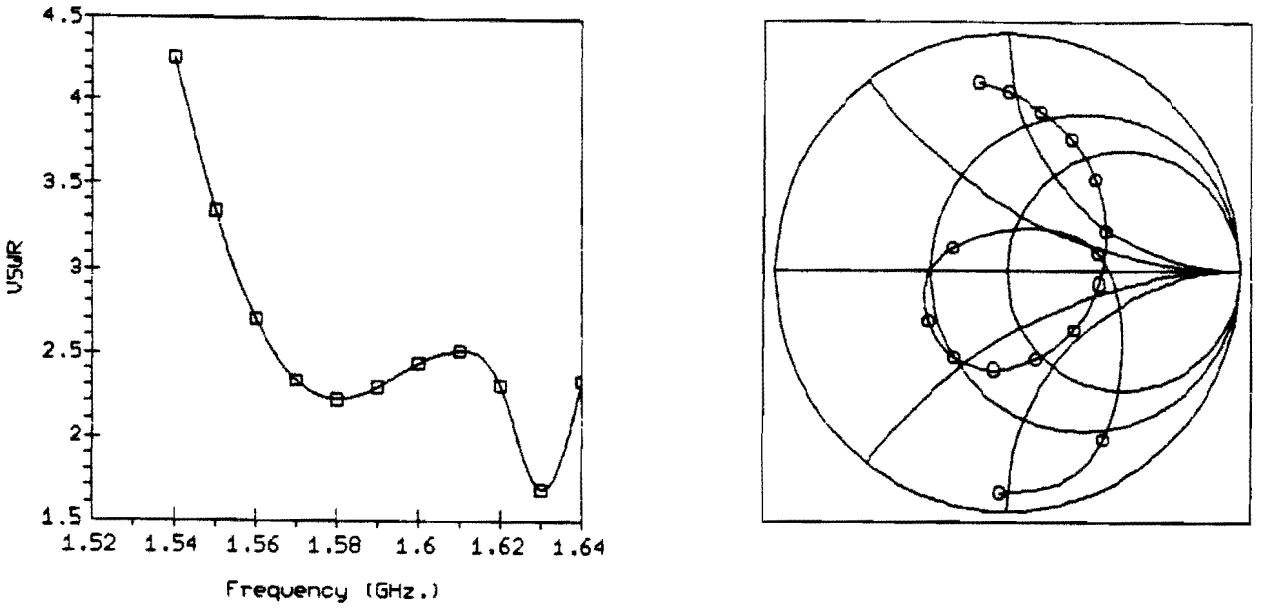

(a) (b)

Fig. 4.22 VSWR (a) and (b) impedance-locus (1.51-0.01-1.66 GHz.), x_{o1} = 2 mm., (x_c, y_c) = (10 mm., 30 mm.)

Ideally, one would aim at obtaining an impedance-loop which provides a proper impedance matching, for instance VSWR < 1.5, for all frequencies in a desired, and preferably large, frequency range. The two examples presented above indicate that for the offset stacked microstrip antennas this can only be achieved to a certain extent, since improving the impedance match by introducing only a small offset invariably reduces the bandwidth over which the antenna is matched to the feed. So, only a relatively small enhancement of the impedance-bandwidth can be obtained using the offset as a design parameter for stacked patch configurations with equally sized stacked patches and a fixed substrate height.

Another interesting feature which can be observed from figures 4.21-4.22 is that when the offset is increased, the stacked microstrip antenna tends towards exhibiting dual-frequency behaviour, with two close, but definitely separate, resonances. This effect can observed more clearly from figures 4.16-4.17, and especially the stacked-patch antenna with the largest offset, x_{o1} = 5 mm., shows typical dual frequency behaviour. As an example of these dual-frequency microstrip antennas, which are also of interest in

microstrip antenna technology, for the case with an offset x_{o1} = 5 mm., the VSWR-curve and corresponding impedance locus are depicted in figure 4.23 for (x_c, y_c) = (5 mm., 30 mm.).

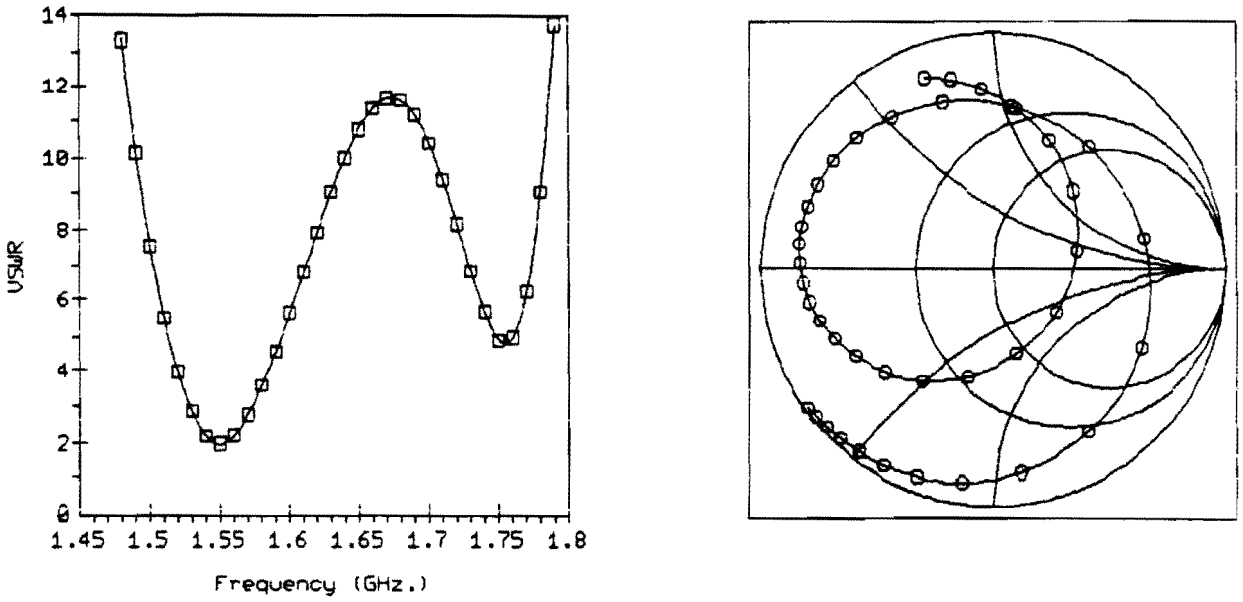

(a) (b)

Fig. 4.23 VSWR (a) and (b) impedance-locus (1.48-0.01-1.82 GHz.), x_{o1} = 5 mm., (x_c, y_c) = (5 mm., 30 mm.)

With regard to the influence of the displacement of the upper microstrip patch relative to the lower patch it can be concluded that, when two equal patches are employed and the thickness of the substrate layers remain fixed, a broader bandwidth can be obtained over which the device exhibits a constant VSWR, but that the proper impedance match to the feed line remains a problem. It is still difficult to achieve both a significant increase in bandwidth and at the same time a good impedance match between the microstrip antenna and its feeding structure. Possibly a combination of both an increase in substrate thickness and the introduction of an offset between the two microstrip patches will yield a sufficient impedance match over a large frequency band, but these microstrip structures have not yet been investigated, and with reference to the examples presented above no spectacular increase in the bandwidth is to be expected compared to a single-patch microstrip antenna. However, when considering this last option

one must keep in mind the increase in the amount of power transferred to the surface wave for thicker substrates and the increased complexity of the stacked microstrip antenna compared to a simple conventional single-layer/single-patch antenna, especially since small errors in for instance the offset will cause a significant change in the antenna characteristics, which then possibly makes it more advantageous to use single-patch antennas with an external matching network for increasing the impedance-bandwidth. More promising is the possibility of creating a dual-frequency microstrip antenna through a large displacement between the two patches.

A major drawback however of the offset stacked-patch configuration is that the whole microstrip device becomes asymmetric. This implies that the objective of creating a circularly polarized microstrip element, using two spatially orthogonal coaxial feeds, cannot be met, because for an asymmetric microstrip antenna with square patches the two feeds would not excite two equal orthogonal current modes, which then would not give rise to two linearly polarized orthogonal radiated waves which, with a proper phase shift, results in circular polarization. Therefore only linearly polarized microstrip antenna elements, either with a moderately improved bandwidth or dual-frequency, can be created employing equal patches and a shift.

So far, all the stacked microstrip antennas analyzed have been fed with the coaxial feed centered in one of the directions of the patches. To illustrate that the analysis method presented in the previous chapters also works well for off-center fed microstrip patches, a stacked microstrip antenna has been analyzed consisting of two square patches of equal size, 8×8 mm., the upper patch shifted sideways, x_{o1} = -1 mm. and y_{o1} = 0 mm., and the feed located on the diagonal of the lower patch at (x_c, y_c) = (2 mm., 2 mm.). Since the feed is now no longer situated symmetrically between two edges of either of the two patches, the patch currents will have both an x- and y-component because there is no preference to any resonant direction due to the equal x- and y-dimensions of the patches. Therefore, two separate orthogonal current modes with a half-sinusoidal variation in the direction of the current have been employed on each patch in the analysis. Further microstrip parameters are: $h_1 = h_2 = 1.57$ mm., $\varepsilon'_{r1} = \varepsilon'_{r2} = 2.33$ and $\tan\delta_1 = \tan\delta_2 = 0.0015$. This particular microstrip structure also serves as an example in various articles

[3][7]. Figure 4.24 shows the impedance-locus.

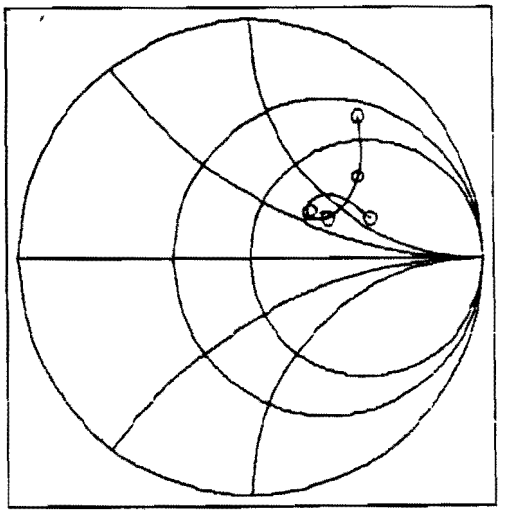

Fig. 4.24 Impedance-locus off-center-fed stacked microstrip antenna (8.5-0.6-10.9 GHz.)

4.3 Different dimensions of the two microstrip patches

In the last section it was observed that stacked microstrip antennas with an offset between the two equal patches yield some interesting characteristics, such as a constant VSWR over a large frequency band and dual frequency behaviour. However, an offset between the two equally sized patches results in asymmetric microstrip antenna elements, which make them unsuitable for obtaining circular polarization. It is thought that the characteristics of these offset-patch microstrip geometries are primarily due to that particular edge of the upper microstrip patch extending in the x-direction across the corresponding edge of the lower patch. If this is assumed it would be possible to create a symmetric stacked microstrip antenna with similar characteristics by stacking to square patches with the top patch having larger dimensions than the bottom one, and subsequently extending all edges of the upper patch an equal distance across the edges of the lower patch in all directions.

This assumption is examined by analyzing a stacked microstrip configuration with an upper square patch having dimensions 62×62 mm. and a lower patch with dimensions 60×60 mm., and an offset $x_{o1} = y_{o1} = -1$ mm. between the upper and lower patch. If the antenna is center-fed at the lower patch, its feed will also be positioned symmetrically between the two edges of the upper patch, and thus only one current mode per patch in the resonant direction is used in the analysis. The parameters for the substrate layers are: $h_1 = h_2 = 1.59$ mm., $\varepsilon'_{r1} = \varepsilon'_{r2} = 2.33$ and $\tan\delta_1 = \tan\delta_2 = 0.001$.

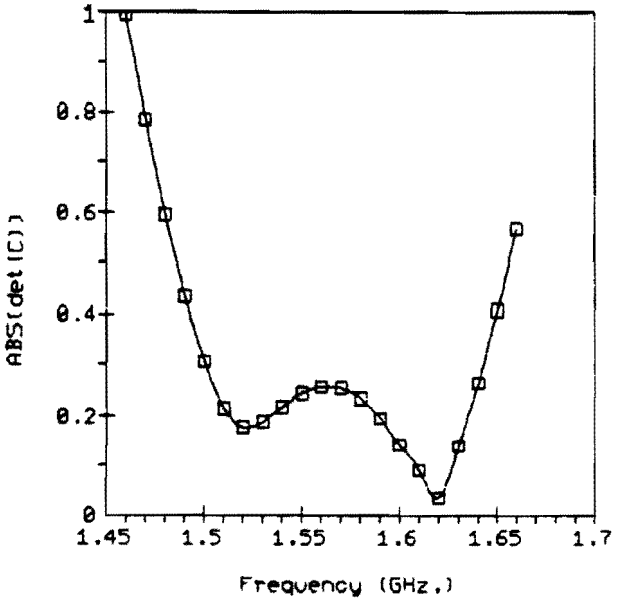

Fig. 4.25 Determinant of the "method-of-moments" matrix for a stacked microstrip structure with differently sized patches, $a_1 = b_1 = 62$ mm., $a_2 = b_2 = 60$ mm., $x_{o1} = y_{o1} = -1$ mm.

The resonance curve depicted in figure 4.25 shows two distinct resonances and this indicates that this particular stacked microstrip geometry tends toward dual-frequency behaviour even stronger than the corresponding case of two equally sized patches with an offset $x_{o1} = 1$ mm. (Fig. 4.16b) for which the two resonances are still very close and can hardly be distinguished. This observation leads to the conclusion that the two resonances and the frequencies at which they appear are in the first place determined by the dimensions of the patches, and for patches having different dimensions they

are already clearly separated. Introducing an additional offset will then obviously separate these resonances even further.

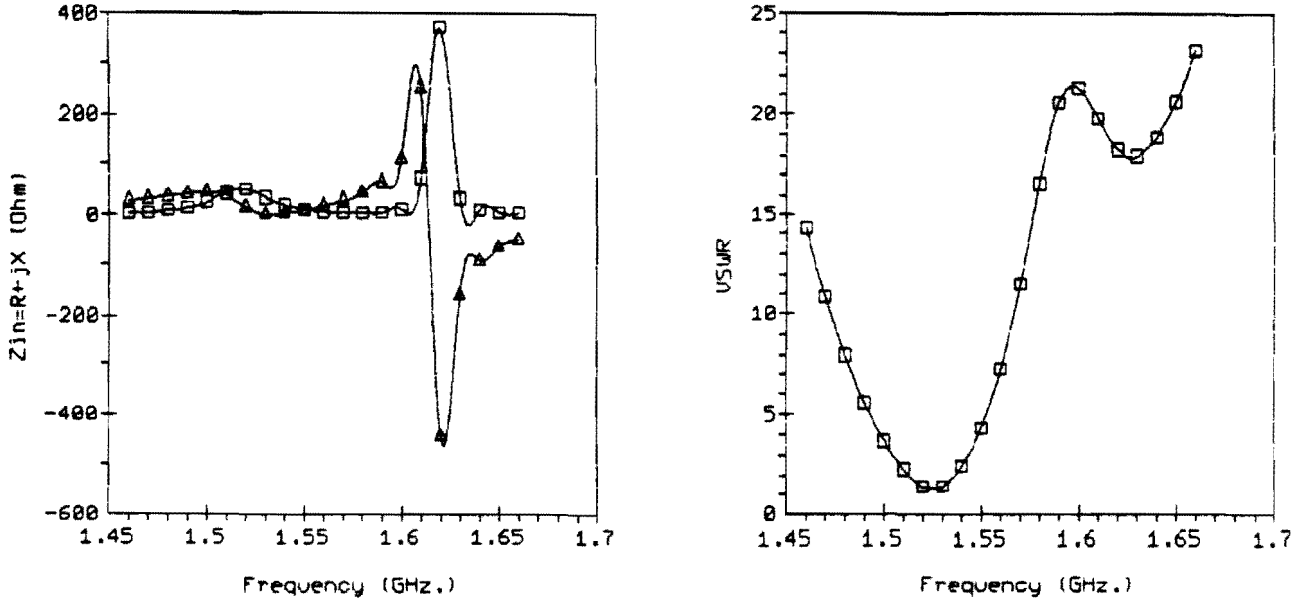

(a) (b)

Fig. 4.26 Input-impedance (a) and VSWR (b), (x_c, y_c) = (5 mm., 30 mm.)

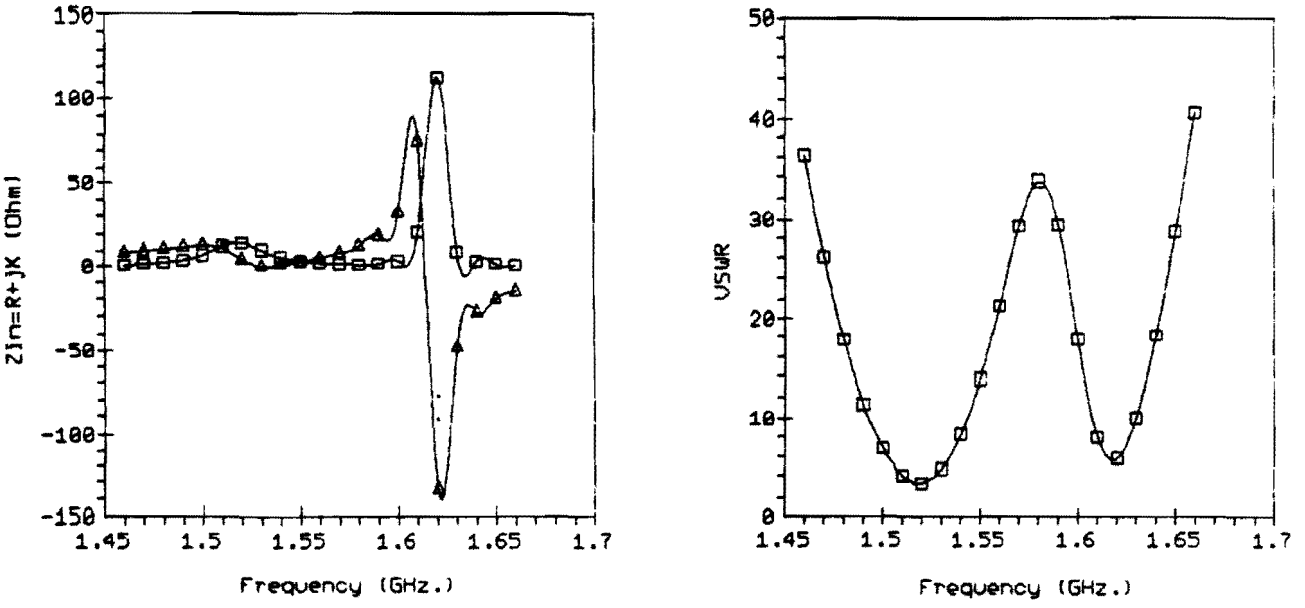

(a) (b)

Fig. 4.27 Input-impedance (a) and VSWR (b), (x_c, y_c) = (20 mm., 30 mm.)

Figures 4.26 and 4.27 show the input-impedance and corresponding Voltage Standing Wave Ratio for the microstrip antenna connected to a 50 Ω coaxial feed line, and for two different feed points (center-fed): (x_c, y_c) = (5 mm., 30 mm.), (20 mm., 30 mm.).

The impedance loci for these cases (Fig. 4.28) again show the typical loop which in this case is relatively large due to the increased separation of the two resonances. Characteristic to this microstrip configuration is also the large difference between the impedance values at the two resonances which renders it even unsuitable for dual-frequency operation, since proper matching can only be achieved for one of the two resonances through a proper choice of the feed point, which can be observed from figure 4.27b.

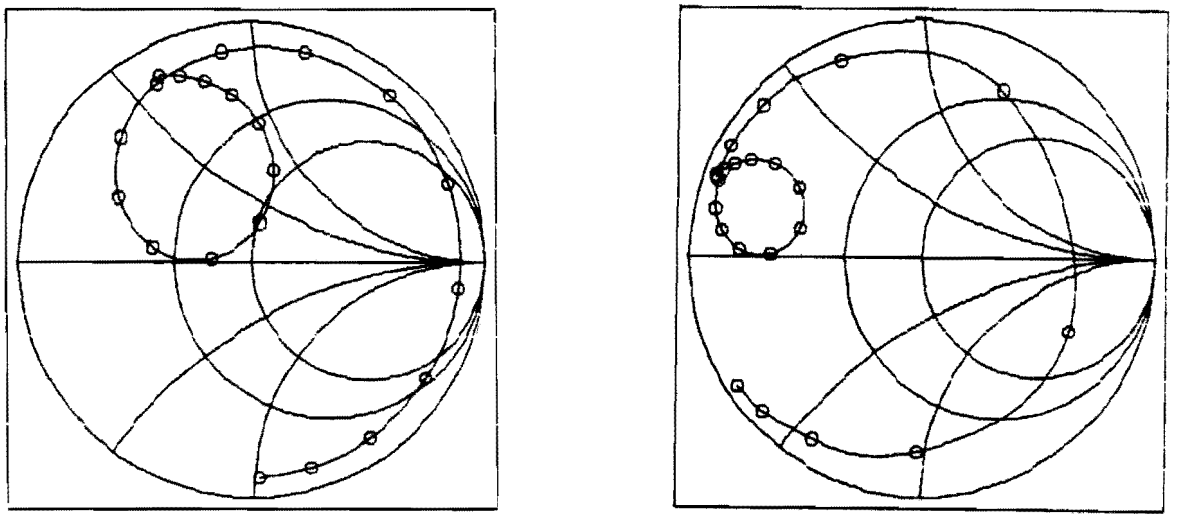

(a) (b)

Fig. 4.28 Impedance loci (1.46-0.01-1.66 GHz.): (a) (x_c, y_c) = (5 mm., 30 mm.) and (b) (x_c, y_c) = (20 mm., 30 mm.)

It might be possible to improve the dual-frequency characteristics by a further increase in the size of the upper patch with respect to the lower patch. This has not been examined yet, but as an illustration of this approach, a stacked (asymmetric) microstrip antenna with differently sized patches, presented in [3], shows an improved dual frequency behaviour,

especially with regard to the impedance values at the two distinct resonances, and it might also be possible to obtain similar characteristics for symmetric microstrip elements. In this example both the upper and lower patch are rectangular with dimensions $a_1 \times b_1$ = 31.2×18 mm. and $a_2 \times b_2$ = 28×18 mm., respectively, there is no offset between the patches, $x_{o1} = y_{o1} = 0$, and the coaxial feed is centered in the y-direction, (x_c, y_c) = (10 mm., 9 mm.). Further microstrip parameters are: $h_1 = h_2$ = 0.51 mm., $\varepsilon'_{r1} = \varepsilon'_{r2}$ = 2.33 and $\tan\delta_1 = \tan\delta_2$ = 0.0012. Figure 4.29 shows the input-impedance and impedance locus for this dual-frequency stacked microstrip antenna.

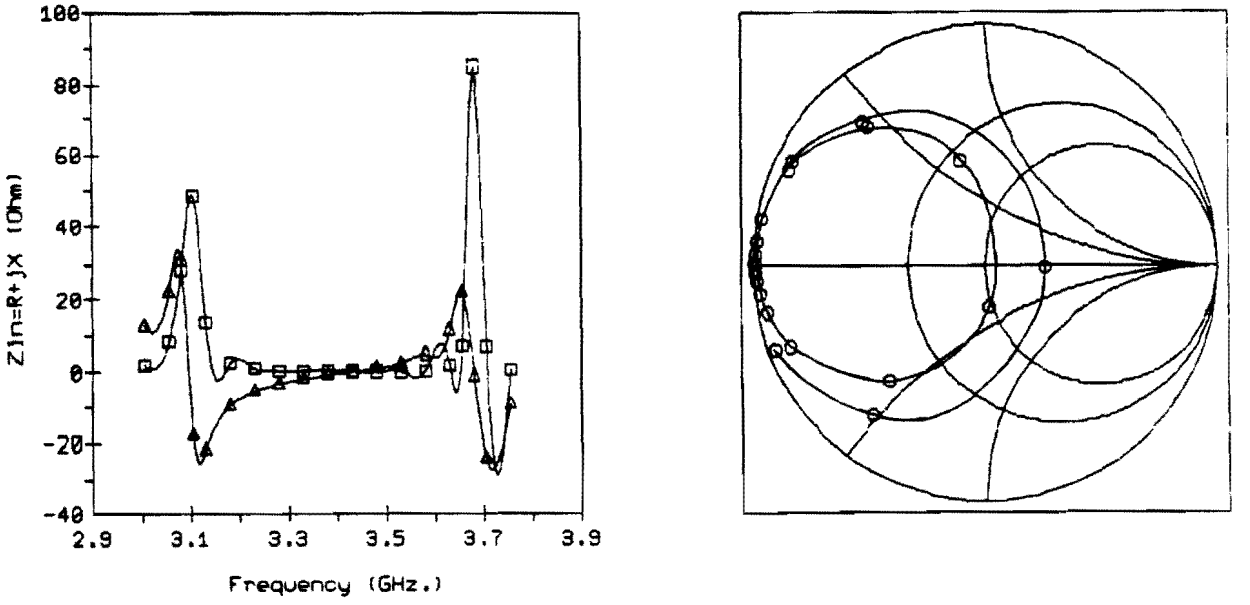

(a) (b)

Fig. 4.29 Input-impedance (a) and (b) impedance locus (3.005-3.775 GHz.) for a dual frequency stacked microstrip antenna

4.4 Different permittivities of the two dielectric layers

In the results presented so far, only stacked microstrip antennas have been analyzed with the substrate layers having equal dielectric properties, i.e., equal dielectric constants and dielectric losses. This is done because almost all cases reported in various articles, [3][7][8], dealt with stacked rectangular microstrip antennas with equal upper and lower substrate layers, and these cases served as a starting point for the examples presented in this report.

However, since the theoretical analysis is given for double-layer microstrip structures with two arbitrary dielectric layers, one can as easily analyze stacked-patch antennas employing substrates with different dielectric properties. Varying the dielectric constants of the substrate layers, possibly in combination with substrate thickness, patch size and offset between the patches, presents a wide variety of stacked microstrip antennas which could be investigated for a possible improvement of the antenna characteristics. Besides a possible improvement in the antenna characteristics studied here, namely the resonance behaviour and input-impedance, the presence of the two dielectric layers with different permittivities also opens up interesting possibilities with regard to some other antenna characteristics such as antenna gain, radiation resistance and radiation efficiency which can be maximized for a proper choice of the microstrip parameters, and also with regard to the possible elimination of the surface waves [22]. Due to time limitations a detailed investigation of these particular microstrip antennas has not yet been carried out.

As an illustration of the fact that the analysis method used also gives correct results for a stacked-patch configuration with two different substrate layers, an example presented in [7] has been analyzed for verification purposes.

This particular configuration consists of two square patches, a 51x51 mm. upper patch and a 41x41 mm. lower patch, and an offset $x_{o1} = y_{o1} = -5$ mm. between both patches. The coaxial feed is again centered in the y-direction between the edges of both patches, $(x_c, y_c) = (0.65 \text{ mm.}, 20.5 \text{ mm.})$, and the antenna can thus be analyzed with one x-directed current mode per patch. The

thickness, dielectric constant and loss-tangent are as follows: h_1 = 8.06 mm., ε'_{r1} = 1.12, $\tan\delta_1$ = 0.005, h_2 = 5.44 mm., ε'_{r2} = 2.54 and $\tan\delta_1$ = 0.0018. The impedance locus in the Smith-chart is shown in figure 4.30 and a good agreement is observed with that in [7].

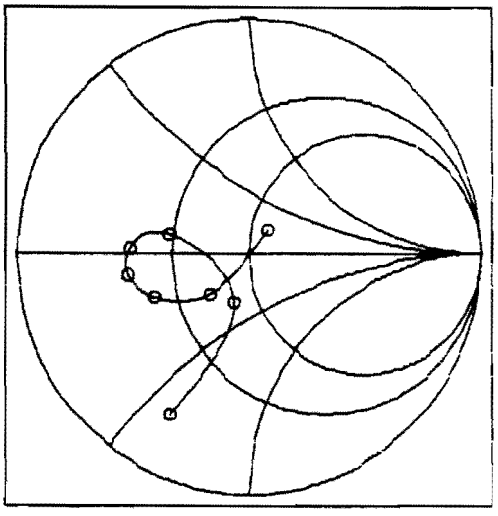

Fig 4.30 Impedance locus for stacked microstrip antenna with different dielectric substrate layers (1.9-0.1-2.6 GHz.)

5 CONCLUSIONS

The model which has been developed for analyzing a dual stacked rectangular microstrip antenna has proved to be well suited for accurately predicting those antenna characteristics which are related to the resonant behaviour and to the impedance-bandwidth of the antenna, such as the appearance of two resonances, the resonant frequencies and the input-impedance and impedance-matching for the microstrip antenna fed by a coaxial feed line. This model considers the microstrip antenna as part of a plane stratified medium and uses potential associated spatial Green's functions and a mixed-potential electric field integral equation which is solved in the space domain for the microstrip patch currents. Especially since efficient numerical techniques are available for dealing with the problems associated with the complex mathematical analysis of the microstrip radiation problem, the model lends itself well for thoroughly investigating stacked microstrip antennas with rectangular patches to gain some insight into their behaviour and designing a microstrip antenna which might possibly meet certain requirements, not realizable with single-patch microstrip antennas.

The stacked microstrip antennas analyzed in this report are not intended for providing a complete understanding of the characteristics of those types of microstrip antennas. They are first of all presented to show the usefulness of the analysis in predicting the characteristics of the stacked microstrip structure instead of pursuing the costly approach of manufacturing and testing different real stacked microstrip antennas.

However, the results presented in this report reveal some interesting properties inherent to stacked-patch microstrip antennas which deserve a closer and more detailed examination. With regard to the impedance-bandwidth it can be concluded that the introduction of the second microstrip patch, resulting in the characteristic impedance-loop in the impedance curve, might possibly provide broadband matching of the stacked microstrip antenna for an optimal choice of the microstrip parameters such as the substrate thickness and permittivity of the substrate layers, the dimensions of the microstrip patches and the offset between the patches. The preliminary results presented here show that variation of the substrate height results in no improvement in impedance-bandwidth for circularly polarized (symmetric) microstrip antenna

elements and that variation of the offset results in only a moderate increase in impedance-bandwidth for linearly polarized (asymmetric) microstrip antenna elements, both having equally sized patches and employing substrate layers with the same dielectric properties. But, in spite of these results, a combination of the variation of all the various microstrip parameters still provides enough options in the design of stacked microstrip antennas, linearly or circularly polarized, for maximizing the bandwidth and improving the matching to the feed line. Another more interesting property is that stacked-patch microstrip antennas are capable of dual-frequency operation, a feature which makes them suitable in applications in which two different frequency bands are used for transmitting and receiving. Again, a more detailed investigation is needed for determining the characteristics of dual-frequency microstrip antennas and their dependence upon the microstrip parameters, and for finding ways of optimizing the dual frequency behaviour.

As a final remark it should be noted that the analysis given only dealt with the so-called near-field quantities, namely the resonant frequency and input-impedance, but that for as proper evaluation of the antenna characteristics the far-field quantities should also be investigated, such as the radiation pattern, antenna gain and radiation efficiency which can also be derived from the microstrip model with only a moderate increase in mathematical complexity.

REFERENCES

[1] Visser H.J.,
'Circularly polarized microstrip phased array antenna for mobile communications (a theoretical research) ',
Graduation report, Group Electromagnetism and Circuit Theory,
Eindhoven University of Technology, Netherlands, Report ET-3-89

[2] den Toom E.C.,
'Microstrip antenne voor de mobiele satelliet communicatie ',
Graduation report, Group Electromagnetism and Circuit Theory,
Eindhoven University of Technology, Netherlands, Report ET-8-89
(in dutch)

[3] Mosig J.R., Barlatey L. and Gardiol F.E.,
'Stacked Microstrip Patches ',
Proc. Phased Array Workshop, Katholieke Universiteit Leuven,
Leuven, Belgium, 26-27 oct. 1988, pp.37-45

[4] Smolders A.B.,
'Analysis of microstrip antennas in the spectral domain using a moment method '
Graduation report, Group Electromagnetism and Circuit Theory,
Eindhoven University of Technology, Netherlands, Report ET-15-89

[5] Long S.A. and Walton M.D.,
'A dual frequency stacked circular disc antenna ',
IEEE Trans. on Antennas and Propagation, vol.AP-27 (1979), pp.270-273

[6] Bailey M.C. and Deshpande M.D.,
'Integral equation formulation of microstrip antennas ',
IEEE Trans. on Antennas and Propagation. vol.AP-30 (1982), pp.651-656

[7] Damiano J.P. and Papiernik A.,
'Antennes microruban rectangulaires multidielectrique ',
Journees Internationales de Nice sur les Antennes (JINA),
Nice, France, nov.1986, pp.203-207

[8] Hassani H.R. and Mirshekar-Syahkal D.,
'Full-wave analysis of stacked rectangular microstrip antennas ',
IEE/URSI 6th International Conference on Antennas and Propagation (ICAP-89), Warwick, UK, 4-7 april 1989, pp.369-373

[9] Mosig J.R. and Gardiol F.E.,
'A dynamical radiation model for microstrip structures ',
In 'Advances in Electronics and Electron Physics', Hawkes P. (Ed.), vol.59, Academic Press, New York, 1982, pp.139-237

[10] Mosig J.R. and Gardiol F.E.,
'Analytical and numerical techniques in the Green's function treatment of microstrip antennas and scatterers ',
IEE Proc., vol.130, Pt.H, no.2, march 1983, pp.175-182

[11] Ramo S., Whinnery J.R. and Van Duzer T.,
FIELDS AND WAVES IN COMMUNICATION ELECTRONICS,
Wiley, New York, 1984

[12] Mosig J.R. and Gardiol F.E.,
'General integral equation formulation for microstrip antennas and scatterers ',
IEE Proc., vol.132, Pt.H, no.7, dec.1985, pp.424-432

[13] Mosig J.R. and Sarkar T.K.,
'Comparison of quasi-static and exact electromagnetic fields from a horizontal electric dipole above a lossy dielectric backed by an imperfect ground plane ',
IEEE Trans. on Microwave Theory and Techniques, vol.MTT-34, no.4, april 1986, pp.379-387

[14] Michalski K.A.,
'The mixed-potential electric field integral equation for objects in layered media ',
AEU, vol.39, 1985, pp.317-322

[15] Mosig J.R.,
'Arbitrarily shaped microstrip structures and their analysis with a mixed potential integral equation ',
IEEE Trans. on Microwave Theory and Techniques, vol.MTT-36, no.2, feb.1988, pp.314-323

[16] Mosig J.R., Barlatey L. and Gardiol F.E.,
'Time harmonic point charges in layered media and their use in microstrip antenna calculations ',
1988 Int. IEEE/AP-S Symposium Digest, Syracuse, New York, USA, june 6-10, pp.1006-1007

[17] Michalski K.A.,
'On the scalar potential of a point charge associated with a time harmonic dipole in a layered medium ',
IEEE Trans. on Antennas and Propagation, vol.AP-35 (1987), pp.1299-1301

[18] Harrington R.F.,
FIELD COMPUTATION BY MOMENT METHODS,
MacMillan, New York, 1968

[19] Carver K.R. and Mink J.W.,
'Microstrip antenna technology ',
IEEE Trans. on Antennas and Propagation, vol.AP-29 (1981), pp.2-24

[20] Wait J.R.,
ELECTROMAGNETIC WAVES IN STRATIFIED MEDIA,
Pergamon, Oxford, 1962

[21] Kong J.A.,
THEORY OF ELECTROMAGNETIC WAVES,
Wiley, New York, 1975

[22] Alexopoulos N.G. and Jackson D.R.,
'Fundamental superstrate (cover) effects on printed circuit antennas ',
IEEE Trans. on Antennas and Propagation, vol.AP-32 (1984), pp.807-816

[23] Mosig J.R.,
'Green's functions for microstrip antennas in multilayered substrates ',
1987 Int. IEEE/AP-S Symposium Digest, Blacksburg, USA, june 15-19,
pp.216-219

[24] Kreyszig E.,
ADVANCED ENGINEERING MATHEMATICS, 6th edition,
Wiley, New York, 1988

[25] Jeuken M.E.J.,
ELECTROMAGNETISCHE GOLVEN EN ANTENNES 1,
Lecture notes, Group Electromagnetism and Circuit Theory, Department of Electrical Engineering, Eindhoven University of Technology, 1983, (in dutch)

[26] Watson G.N.,
A TREATISE ON THE THEORY OF BESSELFUNCTIONS, 2nd edition,
Cambridge University Press, London, 1958

[27] Kong J.A.,
ELECTROMAGNETIC WAVE THEORY,
Wiley, New York, 1986

[28] Abramowitz M. and Stegun I.A.,
HANDBOOK OF MATHEMATICAL FUNCTIONS,
Dover, New York, 1965

[29] Collin R.E. and Zucker F.J.,
ANTENNA THEORY, part 2,
McGraw-Hill, New York, 1969

[30] Jeuken M.E.J.,
Private Communication, 1989

[31] Piessens R., de Doncker-Kapenga E., Überhüber C.W. and Kahaner D.K.,
QUADPACK, A SUBROUTINE PACKAGE FOR AUTOMATIC INTEGRATION
Springer Verlag, Berlin, 1983

[32] Press W.H., Flannery B.P., Teukolsky S.A. and Vetterling W.T.,
NUMERICAL RECIPES, THE ART OF SCIENTIFIC COMPUTING,
Cambridge University Press, 1986

[33] More J.J., Garbow B.S. and Hillstrom K.E.,
USER GUIDE FOR MINPACK-1,
ANL-80-74, Argonne National Laboratory

[34] Deshpande M.D. and Bailey M.C.,
'*Input impedance of microstrip antennas* ',
IEEE Trans. on Antennas and Propagation, vol.AP-30 (1982), pp.645-650

APPENDIX: Complex square root function $w = (z_0^2 - z^2)^{1/2}$

This appendix deals with the double-valued complex square root of the general form

$$w = (z_0^2 - z^2)^{1/2} \tag{A.1}$$

with w and z complex variables, defined on their respective w- and z-plane, and z_0 a complex constant, or, as a special case, a purely real constant.

Because functions of this type are two-valued, the question is if it is possible to define it in such a way that it becomes single-valued. This being of particular importance when a unique specification is needed for w(z), for instance when calculating an integral of some function defined in the z-plane in which these square roots are present [29, p. 238].

Let us first consider the most simple square root, namely the function

$$w = z^{1/2} \tag{A.2}$$

If the complex variable z is represented in polar form

$$z = \rho e^{j\phi} \quad , \quad \rho \geq 0 \tag{A.3}$$

then it is easy to see that if a particular z with argument ϕ is mapped onto point w in the w-plane, that the same z, but with argument $\phi + 2\pi$, is mapped onto point -w. But for argument $\phi + 4\pi$, z is again mapped onto w. Every z thus corresponds to two different points w. If we now define a particular sheet, say the top-sheet, of the z-plane as those values z with arguments

$$4m\pi \leq \phi \leq 2\pi + 4m\pi \quad , \quad m = 0, \pm 1, \pm 2, \cdots \tag{A.4a}$$

and a second sheet, the lower- or bottom-sheet, as all points z with arguments

$$2\pi + 4m\pi \leq \phi \leq 4\pi + 4m\pi \quad , \quad m = 0, \pm 1, \pm 2, \cdots \tag{A.4b}$$

then the square root (A.2) is one-to-one if the two sheets are considered as two separate z-planes. In this case, a cut is introduced in the z-plane, along the positive real axis, to separate the top- from the bottom-sheet. These are called branch-cuts because they provide a cut between the two "branches" of the function (A.2), and the point from which they arise (z = 0) is called the branch-point. Together, the two sheets and the branch cut constitute what is known as a Riemann-surface and is visualized in figure A.1 [24]

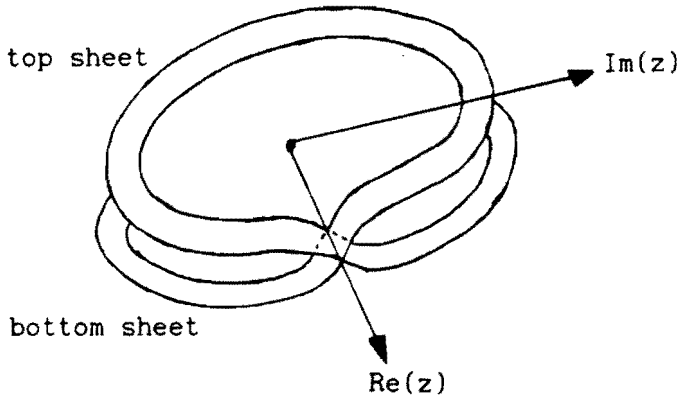

Fig A.3 Riemann-surface for the mapping $z \rightarrow z^{1/2}$

On this surface, the mapping onto the w-plane by (A.2) is defined uniquely, i.e., the entire top-sheet is mapped onto the upper half of the w-plane and the entire bottom-sheet onto the lower half of the w-plane. The choice of the branch cut is somewhat arbitrary; depending on which argument ranges are chosen to define the two sheets, like those in (A.4). But here for the simple square root (A.2) a branch cut along the positive real axis is chosen according to (A.4).

Extending this concept to the double-valued square root (A.1), the main question is now where the branch cuts are situated in the z-plane so as to provide a unique mapping $z \rightarrow (z_0^2 - z^2)^{1/2} = w$. It is also of interest to investigate onto which parts of the w-plane different parts of the z-plane are mapped. A relatively straightforward procedure for determining the branch-cuts and the mapping properties is given below [30].

First, the function (A.1) with z_0 being a positive real constant is considered. If we define $v = z_0^2 - z^2$, in which the intermediate complex variable v is introduced, this variable v maps onto the w-plane according to $v \rightarrow v^{1/2} = w$ and can thus be identified with z appearing in (A.2). The branch-cuts in the complex v-plane can therefore be chosen along the positive real axis. Substituting the polar form for z, Eqn. (A.3), in $z_0^2 - z^2$ yields

$$z_0^2 - z^2 = z_0^2 - \rho^2\cos(2\phi) - j\rho^2\sin(2\phi) \qquad (A.5)$$

and the branch-cut in the v-plane are those points in the z-plane for which Eqn. (A.5) is real and positive. Inspection of (A.5) shows that these points are given by

$$\begin{aligned} &\phi = 0 \quad , \quad 0 \le \rho \le z_0 \\ &\phi = \frac{\pi}{2} \quad , \quad \text{all } \rho \\ &\phi = \pi \quad , \quad 0 \le \rho \le z_0 \\ &\phi = \frac{3\pi}{2} \quad , \quad \text{all } \rho \end{aligned} \qquad (A.6)$$

Figure A.2 shows the z-plane (top- or bottom-sheet) with its branch cuts according to (A.6).

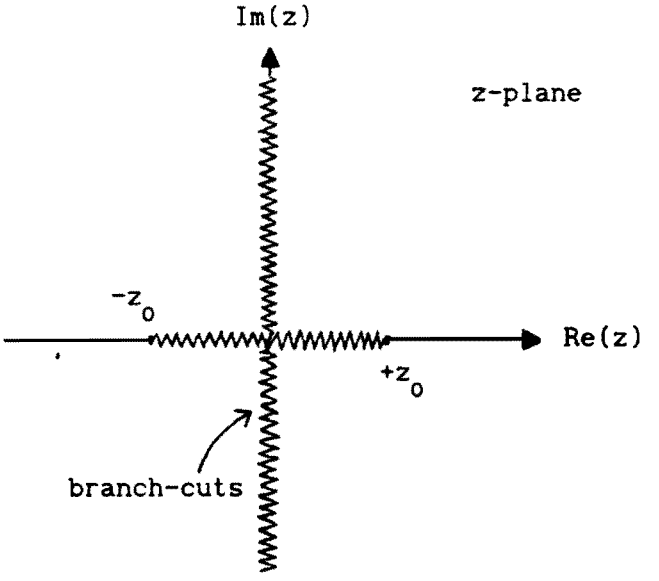

Fig. A.2 Branch-cuts in the z-plane for the mapping $z \rightarrow (z_0^2 - z^2)^{1/2}$ (z_0 real)

To investigate the mapping properties of the different quadrants in both the top- and bottom-sheet of the z-plane onto the w-plane, again the intermediate complex function v is considered, which in polar form is defined as

$$v = z_0^2 - z^2 = \gamma e^{j\theta} = \gamma\cos(\theta) + j\gamma\sin(\theta) \qquad (A.7)$$

and for which, under the mapping

$$v \rightarrow v^{1/2} = w = \gamma^{1/2}\cos(\theta/2) + j\gamma^{1/2}\sin(\theta/2) \qquad (A.8)$$

the arguments θ for v are chosen according to (A.4) to obtain a one-to-one correspondence.

As an example, let us now look at the first quadrant of the z-plane (Fig. A.2). For points in this quadrant, Eqns. (A.5) and (A.7) show that Re(v) can be either positive or negative, whereas $\mathrm{Im}(v) < 0$. The latter means that for points v on the top-sheet of the v-plane, whose arguments lie in the range defined by (A.4a), we must have, for instance, $\pi < \theta < 2\pi$. Substitution of these values into (A.8) then reveal that points in the first quadrant of the z-plane, and in the top-sheet, are mapped onto the region $\mathrm{Re}(w) < 0$, $\mathrm{Im}(w) > o$ in the w-plane. Points v in the bottom-sheet of the v-plane for which $\mathrm{Im}(v) < 0$, for instance values with arguments $3\pi < \theta < 4\pi$, are mapped onto the region $\mathrm{Re}(w) > 0$, $\mathrm{Im}(w) < 0$ in the w-plane. Using a similar procedure, it is easy to show onto which regions in the w-plane the other quadrants, on both the top- and bottom-sheet, are mapped. The result is shown in figure A.3 for the top- and bottom-sheet of the Riemann-surface of the z-plane for the square root function $w = (z_0^2 - z^2)^{1/2}$.

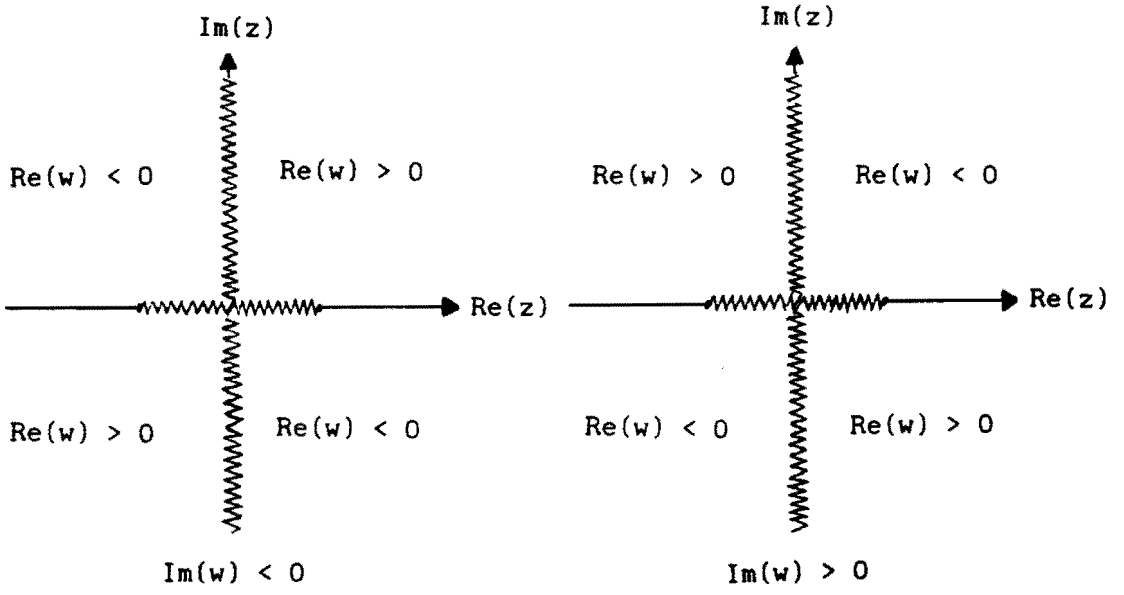

Fig. A.3 Top- (a) and (b) bottom-sheet of the z-plane and its mapping properties under the mapping $z \rightarrow (z^2 - z_0^2)^{1/2} = w$

The constant z_0^2 was assumed to be real in the derivation given above for determining the branch-cuts. It is now instructive to see what happens to these cuts if a small negative imaginary part δ is introduced according to: $z_0^2(1 - j\delta)$, $\delta \geq 0$ with z_0 still real. Writing $z = x + jy$ this yields now for the argument of the square root

$$z_0^2(1 - j\delta) - z^2 = z_0^2 - x^2 + y^2 - j(z_0^2\delta + 2xy) \qquad (A.9)$$

As before, the branch cuts are those points in the z-plane for which (A.9) is real and positive, giving

$$xy = -\frac{z_0^2\delta}{2} \qquad (A.10a)$$

and

$$x^2 - y^2 - z_0^2 \leq 0 \qquad (A.10b)$$

Eqn. (A.10a) represent a hyperbola in the z-plane and the branch-cut is that part of the hyperbola which is situated in the region determined by (A.10b). Plotting (A.10a) together with the hyperbola $x^2 - y^2 = z_0^2$, figure A.4, then

reveals the behaviour of the appropriate branch-cuts for a unique specification of the complex function $w = (z_0^2(1 - j\delta) - z^2)^{1/2}$ with $\delta \geq 0$.

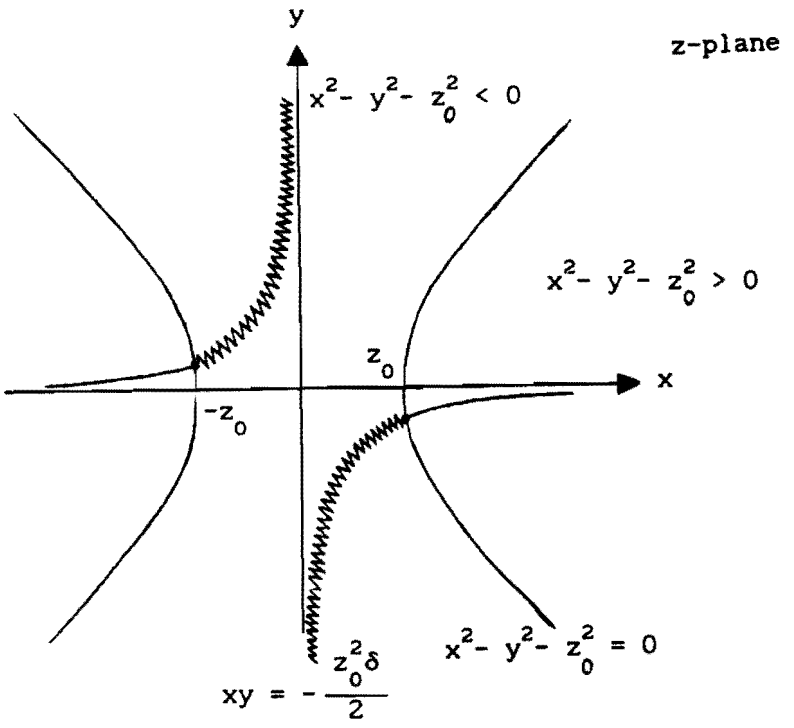

Fig. A.4 Branch-cuts in the z-plane for the mapping
$z \rightarrow (z_0^2(1 - j\delta) - z^2)^{1/2}$, z_0 real

The branch-points in this case are the intersections of the two hyperbolas and follow from the equation $z_0^2(1 - j\delta) - z^2 = 0$. Taking the limit $\delta \rightarrow 0$ obviously reduces the branch-cuts in Fig. A.4 to those in Fig. A.2.